UNIVERSITEIT VAN PRETORIA
UNIVERSITY OF PRETORIA
YUNIBESITHI YA PRETORIA

The effect of palladium deposition on electrically active defects in irradiated silicon

by

Abraham Willem Barnard

Submitted in partial fulfilment of the degree

PhD (Physics)

in the Faculty of Natural & Agricultural Sciences

University of Pretoria

Pretoria

December 2023

Supervisor: Prof W E Meyer

Co-supervisor: Prof F D Auret

© University of Pretoria

Abstract

DLTS was used to study the effect of resistive physical vapour deposition of Pd Schottky contacts on the defects observed in an n-type Si substrate that was irradiated before deposition ("pre-irradiated") and compared to defects in a diode that was irradiated after deposition ("post-irradiated"). In the post-irradiated samples, the familiar radiation-induced defects were observed. However, in the pre-irradiated samples, 13 new defects were observed, with DLTS signatures differing from those of the defects in the post-irradiated diodes.

Out of the 13 newly observed defects, four defects, with activation energy of 0.180, 0.220, 0.360 and 0.607 eV, had DLTS signatures corresponding to defects previously observed in Pt-containing Si, while no match was found for other defects.

The effect (referred to as the Pd Effect) was carefully studied, and it was found that the effect was only observed with Pd, and not when other metals including Au, Ni, Al, Ag were used. Careful experiments ruled out annealing during evaporation of the contact as a possible cause. Different sources of Pd were used in un-used crucibles in an attempt to avoid contamination, but the effect was observed in all cases.

It was found that this phenomenon was inhibited by the presence of a thin intermediate layer, irrespective of the layer being Pd or Au. We therefore conclude that the effect is only observed when Pd is deposited directly on the irradiated Si surface.

We believe that these defects are produced by defect-enhanced diffusion of Pd.

Overall, the study enhances our understanding of defect behaviour in silicon-based devices, particularly under irradiation and metal deposition conditions, and reveals the unique properties and effects of Pd.

© University of Pretoria

Declaration

I, Abraham Willem Barnard declare that the thesis, which I hereby submit for the degree PhD(Physics) at the University of Pretoria, is my own work and has not previously been submitted by me for a degree at this or any other tertiary institution.

SIGNATURE:

DATE: 2023/12/08

© University of Pretoria

Acknowledgements

To My Parents:

Thank you for your support and guidance throughout my academic journey. It's been a long road with many challenges, and having your backing has made a real difference. I appreciate the opportunities you've given me and the support you've provided when things got tough. Proud of what I've accomplished, I'm grateful for your role in it.

To My Supervisor:

Our professional relationship has been a real learning experience, filled with its own set of challenges. I acknowledge the role you've played in guiding my academic path. It's been tough at times, but it's taught me a lot of experience. Thanks for your guidance on my research and the academic counsel you've provided. Your involvement, despite its complexities, has been a significant part of my learning process. I appreciate having had the opportunity to work under your supervision.

To My Colleagues and Fellow Researchers:

To those who shared in the genuine moments of collaboration and camaraderie, your support and shared insights were appreciated. The academic environment, with all its complexities, has been enriched by these interactions.

"When the world shoves you around, you just gotta stand up and shove back. It's not like somebody's gonna save you if you start babbling excuses."

"Talent is something you make bloom, instinct is something you polish."

“A lesson without pain is meaningless. For you cannot gain something without sacrificing something else in return.”

© University of Pretoria

Table of Contents

1 Introduction 10
1.1 Motivation 10
1.2 Approach 11
1.3 Dissertation layout 11
2 Semiconductors and the Schottky diode 12
2.1 Semiconductors 12
2.1.1 Crystal growth 12
2.1.2 Crystal structure of Si 12
2.1.3 Band structure of Si 13
2.2 The Schottky diode 14
2.2.1 The ideal Schottky diode 14
2.2.2 Zero, reverse and forward bias 15
2.3 Semiconductor defects 16
2.3.1 Defects 16
2.3.2 Radiation induced defects 18
2.3.3 Deep- and shallow-levels 19
2.4 Deep-level transient spectroscopy 20
2.4.1 Capacitance signal 20
2.4.2 Thermal DLTS signal processing 23
2.4.3 Laplace DLTS 25
2.5 DLTS defect profiling techniques 26
2.5.1 Electron emission activation energy 26
2.5.2 True capture cross-section 26
2.5.3 Depth profiling 27
2.5.4 Annealing kinetics 28
2.6 References 30
3 Radiation-induced defects within silicon 32
3.1 Reactions of carbon-interstitials (C_i) 32
3.1.1 Carbon-interstitial (C_i) 33
3.1.2 Carbon-interstitial oxygen-interstitial (C_iO_i) complex 34
3.1.3 Carbon-interstitial carbon-substitutional (C_iC_s) 36
3.2 Oxygen-Vacancy (O_iV) 38
3.3 Di-vacancy (V_2) 39

© University of Pretoria

3.4 Phosphorus-substitutional vacancy (P_sV) 40
3.5 References 41
4 Palladium-related defects in Si 46
4.1 Palladium and hydrogen 46
4.1.1 Pure palladium 46
4.1.2 Hydrogen adsorption at metal surfaces 47
4.1.3 Removal of hydrogen from palladium-hydrogen 50
4.2 Noble metal diffusion in Si 50
4.2.1 Palladium silicide 50
4.2.2 Palladium in silicon 51
4.2.3 Diffusion of metals 51
4.3 Pd and H related defects in Si 51
4.3.1 Silicon hydride 52
4.3.2 Pd related energy levels 52
4.4 References 54
5 Experimental Techniques 57
5.1 Sample preparation and measurements 57
5.1.1 Cleaning process 58
5.1.2 Schottky and ohmic contact fabrication 58
5.1.3 Electron irradiation 59
5.1.4 Annealing 60
5.1.5 DLTS characterization 60
5.2 References 61
6 Results and discussion 62
6.1 Samples and baseline measurements 62
6.1.1 Baseline results: Wafer 1 (Medium carbon and oxygen concentration) 63
6.1.2 Baseline results: Wafer 2 (Low carbon and oxygen concentration) 63
6.1.3 Baseline results: Wafer 3 (Low carbon and high oxygen concentrations) 64
6.1.4 Baseline results: Wafer 4 (High carbon and medium oxygen concentrations) 64
6.2 The effect of metal deposition 67
6.2.1 Experimental setup 67
6.2.2 Results 68
6.3 Effect of an intermediate Au or Pd layer and irradiation through a thick Pd layer 69
6.3.1 Experimental setup 69
6.3.2 Results and discussion 71

© University of Pretoria

6.4 H, Pd and contamination 72
6.4.1 Experimental setup....73
6.4.2 Results 73
6.5 Isochronal annealing....75
6.5.1 Experimental setup....75
6.5.2 Results: Post-irradiated samples....75
6.5.3 Results: pre-irradiated samples....78
6.6 Identification of Pd effect complexes 87
6.6.1 Experimental....87
6.6.2 Results 87
6.7 Arrhenius plots and defect identification 90
6.7.1 Experiment....90
6.7.2 Results and discussion 90
6.8 Depth profiling....93
6.8.1 Experiment....93
6.8.2 Results 93
6.9 References....94
7 Discussion and Conclusion 96
7.1 Summary overview....96
7.2 Discussion of possible complex structure 98
7.3 Conclusion 100
7.4 Future work....101
7.5 References....102

© University of Pretoria

List of Figures

Figure 2.1: Energy diagram showing the formation of the ideal Schottky barrier. Metal and semiconductor are completely isolated (a) separated by a vacuum. Metal and semiconductor are in perfect contact (b) (Montanari, 2005). 15
Figure 2.2: Diagram showing the effect of placing an unbiased Schottky diode (Left) under forward (Middle) and reverse (Right) bias. 16
Figure 2.3: Simplified diagram representing point defects within crystals 17
Figure 2.4: Simplified diagram representing dislocations within crystals 17
Figure 2.5: Simplified diagram representing intrinsic and extrinsic stacking faults 18
Figure 2.6: Diagram representing the development of clusters due to an energetic particle entering the crystal from the bottom of the figure. Insert image shows the displacement of atoms when exposing the substrate to electromagnetic (left) and heavy particle (right) radiation. 19
Figure 2.7: Simplified energy diagram showing the position of deep and shallow levels within the band gap. E_C and E_V are the conduction band and valence band respectively. Deep levels here are shown to be more localized while shallow levels have an extended nature. 20
Figure 2.8: Diagram depicting the position of the depletion region for the p-n diode, Schottky diode and the MOS diode connected in a circuit to generate a signal used in DLTS. 21
Figure 2.9: Basic process of a DLTS cycle and the capacitance transient obtained from the cycle (Lang, 1974). .. 23
Figure 2.10: Simplified simulated graphs showing double-boxcar analysis of temperature-scanned DLTS measurements of a single deep level. Capacitance transients (left) were generated for different temperatures. The difference in capacitance at two times, t_1 and t_2, were calculated and plotted as a function of temperature on the right (Zurich Instrument, 2017). 25
Figure 2.11: (a) Conventional DLTS signals (1-5) obtained over a temperature region for different rate windows, leading to the Arrhenius plot (b) obtained from the temperature and emission rate of each defect. (After Lang, 1974). 26
Figure 2.12: Changing the filling pulse width and the effect on the peak obtained for capture cross-section measurements. (After Lang, 1974) 27
Figure 2.13: Changing the filling pulse height and the effect on the peak obtained for depth profiling. 28
Figure 3.1 Configurational-coordinate energy diagram (in eV) for the acceptor (top) and donor (bottom) state of the C_iC_s complex. (After Song 1988.) 37
Figure 4.1 Potential energy of hydrogen approaching a metal surface based off the Lennard-Jones potential (Kirchheim and Pundt, 2014) 48
Figure 4.2 Interstitial octahedral and tetrahedral sites within FCC crystal lattice. 49
Figure 5.1 The two main sequences used for Schottky diode fabrication: post-irradiation (blue arrows) and pre-irradiation (red arrows) samples. (1) Cleaning of sample, (2) deposition of metal for fabrication of Schottky contacts, (3) exposure to electron irradiation and (4) sample ready for analysis. 57
Figure 5.2 Simple side view schematic of the resistive evaporation deposition system. 58
Figure 5.3 Energy distribution of electrons emitted by a ^{90}Sr radionuclide. The Sr + Y energy distribution has been displaced by an amount indicated by the arrow for clarification (Auret, Goodman, Myburg and Meyer, 1993). 59
Figure 5.4 Annealing apparatus. 60
Figure 5.5: *Conventional and Laplace DLTS experimental block diagram setup*. 61
Figure 6.1 Typical IV characteristics of the un-irradiated, pre-irradiated and post-irradiated diodes. The straight lines represent the fit used for the determination of their parameters. 63
Figure 6.2 DLTS spectra of Samples 1 – 4 directly after irradiation and after being left at room temperature for 10 days. Measured at 1 K/min at 200 Hz under a reverse bias of −2 V and forward bias of 0 V of 1 ms pulse length. 66

© University of Pretoria

Figure 6.3 Arrhenius-plots comparing the defects observed in the 4 samples. For clarity, the defects measured in Sample 1 are shown in black and the additional defects observed are shown in red (Sample 2) and green (Sample 4). ... 66
Figure 6.4 Schematic diagram of the procedure showing the selected metal Schottky diode deposited on the first half of the sample's surface (1). The full sample was then exposed to electron irradiation from the ^{90}Sr Source (2). A second Schottky diode was deposited on other half of the sample's surface (3). The resultant sample (4). ... 68
Figure 6.5 C-DLTS spectrums for Schottky diodes of different metals irradiated after deposition (post-irradiated) and before deposition (pre-irradiated). Samples were taken from Wafer 1 and exposed to irradiation for 18 hours at room temperature. ... 69
Figure 6.6 The sample was placed on top of the mask with a moveable shield below the mask to selectively prevent metal from being deposited through some of the holes. During the deposition the shield would be slid to the right revealing more holes in the mask to allow more Schottky diodes to form on the surface of the sample. This allowed multiple Schottky diodes with varying thicknesses to be deposited in a single deposition. ... 70
Figure 6.7 Schematic section through the 5 Schottky diodes fabricated on each sample. The first deposition resulted in Schottky diodes with thickness of 0, 20, 40, 60 and 80 Å of Au/Pd deposited. The samples were then exposed to irradiation before a thick layer of approximately 500 Å of Pd was deposited over the previously deposited diodes. ... 70
Figure 6.8 C-DLTS spectrums of contacts where different thicknesses of Au were deposited before exposing the Schottky diodes to irradiation followed by depositing 500 Å of Pd. ... 72
Figure 6.9 Isochronal annealing profiles of Sample A1 with 5 K incremental annealing steps at 10 minutes intervals measured 1 µm beneath the surface junction. Reversed calculation of $C_iO_i^*$ concentration introduced into the sample based on C_i and C_iC_s observed concentration change. ... 76
Figure 6.10 Normalized isochronal annealing profiles for Sample A2 with 5 K incremental annealing steps at 10 minutes intervals measured 1 µm beneath the surface of the Si. ... 79
Figure 6.11 L-DLTS signals observed at critical temperatures for Sample A2 throughout the isochronal annealing process. These measurements were done under -2V reverse bias, 0 V filling pulse and a 1 ms filling pulse width. ... 80
Figure 6.12 Sample A2 isochronal annealing profiles showing the relationship between the E1, E2 and E4 ... 82
Figure 6.13 Sample A2 isochronal annealing profiles showing the E7 annealing out completely before being re-introduced to the system just to be annealed out at a higher temperature. ... 84
Figure 6.14 Sample A2 isochronal annealing profiles isochronal annealing profiles showing the relationship between the E9 and E10. ... 86
Figure 6.15 C-DLTS spectrums of the 8 samples (Wafer 1) prepared under different conditions. Samples 1a, 1b, 1c and 1d, Pd Schottky diodes were fabricated before irradiation and Samples 1e, 1f, 1g and 1h were fabricated after irradiation. All DLTS spectrums were recorded with a -2 V reverse bias, zero filling pulse, 1 ms pulse length and at 200 Hz. ... 89
Figure 6.16 C-DLTS spectrums of the 4 samples from Wafer 2 and Wafer 3 prepared under different conditions. Samples (2a), (2b), (3a) and (3b), Pd Schottky diodes were fabricated before irradiation and Samples (2e), (2f), (3e) and (3f) were fabricated after irradiation. All DLTS spectrums were recorded with a -2 V reverse bias, zero filling pulse, 1 ms pulse length and at 200 Hz. ... 89
Figure 6.17 Arrhenius measurements of emission activation energy for the pre-irradiated samples directly after deposition (red) and introduced during annealing (green). ... 91
Figure 6.18 The depth profiles of E1, E2, E3, E4, E7 and E14 recorded in Cz Si after a Pd Schottky diode was resistively evaporated onto a pre-irradiated Sample 1 (See Figure 6.2). The depth profile of E5 was recorded after the sample was annealed at 400 K. ... 94

© University of Pretoria

List of Tables

TABLE 3.1 SUMMARY OF PREVIOUS INVESTIGATIONS OF THE C_I DEFECT'S PROPERTIES. 34
TABLE 3.2: EXPERIMENTAL PROPERTIES OF THE C_IO_I COMPLEX OBTAINED FROM LITERATURE. 35
TABLE 3.3: EXPERIMENTAL PROPERTIES OF THE C_IC_S COMPLEX OBTAINED FROM LITERATURE. 37
TABLE 3.4: EXPERIMENTAL PROPERTIES OF THE O_IV COMPLEX OBTAINED FROM LITERATURE. 38
TABLE 3.5 EXPERIMENTAL PROPERTIES OF THE V_2 REPORTED IN LITERATURE. 40
TABLE 3.6: EXPERIMENTAL PROPERTIES OF THE P_SV COMPLEX OBTAINED FROM LITERATURE. 41
TABLE 6.1 SUMMARY OF THE PROPERTIES OF THE WAFERS USED IN THIS STUDY (DATA SUPPLIED BY THE FRAUNHOFER IPMS). 62
TABLE 6.2 TABLE SUMMARIZING THE DEFECTS OBSERVED IN ALL 4 SAMPLES DIRECTLY AFTER IRRADIATION BY ^{90}SR AND AGAIN AFTER THE SAMPLE WAS LEFT AT ROOM TEMPERATURE FOR 10 DAYS. 65
TABLE 6.3: SEM RESULTS FOR PD SCHOTTKY DIODES ON SAMPLE 1. 75
TABLE 6.4: OVERVIEW OF SAMPLE A1 ISOCHRONAL ANNEALING PROFILES: S-CURVE ANALYSIS WITH MIDPOINT TEMPERATURE, ANNEALING RATE, AND DEFECT CONCENTRATION CHANGES 76
TABLE 6.5: SAMPLE B1 ISOCHRONAL ANNEALING PROFILES: MODEL FITTINGS AND SEQUENCE OF CONCENTRATION CHANGES (1-4) INDICATING MULTIPLE ANNEALING PROFILES FOR SOME DEFECTS 78
TABLE 6.6: ELECTRICAL PROPERTIES OF DEFECTS OBSERVED IN WAFER 1. 92

© University of Pretoria

1 Introduction

Silicon (Si), atomic number 14 forming part of the group IV elements on the periodic table, is seen as the most important material in the semiconductor industry. Germanium (Ge), was known as the grandfather material paving the road to integrated circuit development and semiconductor transistors. The first contact transistor was made by wedging a gold foil into a slab of Ge using plastic wedges. Since then the fabrication of transistors has drastically improved with Si taking over the semiconductor industry. This takeover was mainly caused by the ease of availability and the materials ability to form stable oxide layers. Imperfections in the regular geometrical arrangement of atoms within the crystal (defects), change the electrical behaviour of semiconductors. This includes the carrier lifetime, the conductivity, the mechanical strength and finally, the quality of the electrical device (Schottky diode, diode, laser diode, photocell, etc.) produced.

1.1 Motivation

Si is the most used semiconductor material, with an annual semiconductor gross sale of over 481 billion USD as of 2018. Being the second most abundant element in the earth's crust, the low cost of using the material and all the well-established processing techniques makes the material one of the strongest competitors within the market. Si has a large band gap of around 1.12 eV which allows it to absorb wavelengths within the visible spectrum. Due to the hardness of this material, large wafers can safely be handled without any damage. The material allows for easy formation of high quality oxide layers (SiO_2) and is thermally stable up to 1100 °C. However, the material is far from perfect and does come with its own disadvantages. The material is brittle, some of the processing stages are very wasteful, the life cycle can be considered short and pure Si crystals are expensive to produce.

Since the development of the first Si semiconductor in 1906, industry has shown very little digression from using this material to develop new technology. Looking towards the future, the limitations of this material will not be reached for many more years to come and the general industry will not likely use alternative materials. GaAs, GaN and most other semiconductor substrates are currently only used for unique applications. However, recently, the second space race has started and companies are looking towards terra-forming other planets and building equipment in space. Up until now, technology has been developed within safe and controlled environments before being sent into space. Within the next couple of years, companies will look into building integrated circuits on other planets (e.g. Mars) and even in the dead of space for space stations. These environments are much more hazardous and contains high energy radiation which can alter the properties of the material during fabrication.

It has always been a safe assumption within the semiconductor community that exposing substrates to radiation before deposition of metals will not alter the results. In fact, the final device should have the same properties as a device that was fabricated and exposed to exactly the same irradiation conditions. In this thesis, this theory will be tested against palladium (Pd), with a high level study of how the electrical properties of Si based Schottky diodes can be changed by depositing Pd after the substrate has been exposed to irradiation.

© University of Pretoria

1.2 Approach

The aim of this thesis is to show the effect of depositing Pd before and after Si has been exposed to irradiation. In this, multiple issues and limitations were explored and discussed. The main experimental techniques used were conventional deep-level transient spectroscopy (DLTS) and Laplace transform DLTS.

Multiple sources of Si were used to control the concentration of traps introduced by irradiation from an ^{90}Sr radio nuclide. Similarly, these were used to control the introduction of the new traps caused by the deposition of Pd on Si samples already exposed to irradiation. By varying the temperature during irradiation, control over the concentration of traps was further enhanced. Multiple metals were investigated to see if the effect was limited to only Pd, with Pd taken from multiple sources to rule out contamination.

Depth profiling was used to determine if the new traps were limited to the surface or penetrated deeply into the samples. Deposition profiles were done to determine if the effect is limited to only Pd making contact with the surface of the Si or if the affect can persist through metal already deposited on the surface. Finally, deep energy level profiles were done to aid in the identification of the complexes observed.

1.3 Dissertation layout

- Chapter 2 covers the general background theory for ideal Schottky diodes, relevant theory for characterization of electrical properties of traps near the Schottky diode junctions and experimental practices.
- Chapter 3 discusses the common radiation-induced defects observed in phosphorous-doped (P-doped) Si exposed to irradiation. This includes previously measured electrical properties and proposed defect structures.
- Chapter 4 discusses the properties of Pd, hydrogen adsorption and Pd-related defects previously investigated in Si.
- Chapter 5 summarizes the experimental techniques used to prepare samples and measure their electrical properties.
- Chapter 6 presents and gives a discussion of the results obtained in this study.
- Chapter 7 presents the summary of results, general conclusions and suggests future work.

© University of Pretoria

2 Semiconductors and the Schottky diode

2.1 Semiconductors

Semiconductors have electrical conductivity values which fall between that of a conductor and an insulator. Unlike metals, the resistivity of a semiconductor falls with rising temperature. The conduction properties are altered significantly by doping the crystal structure with relatively small amounts of impurities. Semiconductor junctions are created by doping two regions in the same crystal differently. The basis of modern day technology – diodes and transistors – are controlled by the behaviour of the electrons, ions and holes at these junctions (Streetman, 2016).

The semiconductors Si, Ge and GaAs are some of the most commonly used materials for the fabrication of modern day electronics. Semiconductors are typically formed from pure Group IV elements or binary compounds made from the combination of Group III and V elements or Group II and VI elements (Sze, Ng and Li, 2006).

The most common material Si forms part if the Group IV elements of the periodic table. With the atomic weight of 28.086, the material has a melting point around 1410 °C. While many other materials (Ge, GaAs, GaN, etc.) are considered for the fabrication of electronic devices, Si is still widely used in the multi-billion-dollar industry (Streetman, 2016).

In this chapter, the discussion given will be based on n-type material. A similar approach is valid for p-type material.

2.1.1 Crystal growth

Bulk semiconductor-grade material is commonly produced by cooling molten Si material. However, by simply cooling down the material, undesirable poly-crystalline material will be produced. The two methods, Czochralski and Bridgeman are instead used to produce high purity single bulk crystals.

Czochralski crystals are produced by melting high purity Si in a crucible. Impurities such as P, Sb or As are added during the molten phase as dopants. A seed crystal in a specific orientation is attached to the end of a rod and dipped into the molten material. The rod is then slowly rotated while being pulled up from the molten liquid. The size of the final crystal is controlled by the speed the rod is rotated and pulled from the molten material and the temperature gradient of the crystal (Kuech and Nishinaga, 2015).

Bridgeman-Stockbarger crystals are produced by placing the seed crystal at one end of a container and filling the container with high purity molten Si. The material is then cooled from the seed crystal's location to the other side of the container. During this process the container is rotated to stir the molten liquid (Capper, Rudolph and Scheel, n.d.).

2.1.2 Crystal structure of Si

Si crystallizes according to the diamond structure. It is composed of two interpenetrating face-centred cubic (FCC) lattices displaced diagonally by a $\frac{a_0}{4}(1,1,1)$ translation to form the tetrahedral lattice. The lattice parameter a_0 for Si is 0.543 nm with the nearest atomic neighbours a distance

© University of Pretoria

0.235 nm apart. In industry the crystal is most commonly cut into wafers along the (100) plane (Patterson and Bailey, 2019).

2.1.3 Band structure of Si

Bringing isolated atoms together to form a solid results in various interactions between neighbouring atoms. At the proper interatomic spacing for crystal formation, the forces of repulsion and attraction between atoms will balance out. Important changes in the electron energy level configurations occur, leading to the formation of energy bands that determine many of the material's properties (Streetman and Banerjee, 2016).

Quantitative calculations are done to obtain the band structure properties, which uses the assumption that a single electron travels through a perfect periodic lattice (i.e. crystal) in a single direction (i.e. the x-direction) (Streetman and Banerjee, 2016). By solving and approximating the one-electron Schrödinger equation, the energy – momentum relationship can be obtained for a crystalline structure. According to Bloch's theorem, if the potential energy $V(\vec{r})$ is periodic with the periodicity of the lattice, the solutions $\phi_k(\vec{r})$ of

$$E_k\phi_k(\vec{r}) = [-\frac{\hbar^2}{2m}\nabla^2 + V(\vec{r})]\,\phi_k(\vec{r}) \tag{1}$$

is given in the form of

$$\phi_k(\vec{r}) = e^{j\vec{k}\bullet\vec{r}}U_n\left(\vec{k}\bullet\vec{r}\right), \tag{2}$$

with $U_n\left(\vec{k}\bullet\vec{r}\right)$ the function modulating the wave function with accordance to the periodicity of the crystal lattice and $\vec{k}$ the propagation constant (Sze, Ng and Li, 2006). From Bloch's theorem, the energy $E_{\vec{k}}$ is shown to be periodic in the reciprocal lattice, which makes using only $\vec{k}$'s in the primitive cell of a reciprocal lattice sufficient to obtain the unique energy for a given band index (Kittel and Fong, 2010).

When calculating the band structure one can plot the allowed energy values vs. the propagation constant ($\vec{k}$). For most lattices, the periodicity is different in various directions, which requires one to plot the (E, $\vec{k}$) diagram in different directions to obtain the full relationship (Smith, 1987).

The Fermi-level of an undoped semiconductor lies in an energy region in which no allowed states exist, which is known as the energy gap. The conduction band is the band above the energy gap and the valance band is the band below the gap (Kittel, 2005). For Si, the lowest conduction-band minimum is along the <100> axis (of which there are six equivalents) and the valance band maximum is at the centre of the Brillouin zone (Sze, Ng and Li, 2006).

Under normal atmospheric pressure and at room temperature, the band gap for Si was found to be 1.12 eV for high purity materials. For highly doped materials, the band gaps become smaller. The band gap was shown experimentally to decrease with increasing temperature for Si with the relationship approximated by:

$$E_g(T) = E_g(0) - \frac{\alpha T^2}{(T+\beta)}, \tag{3}$$

© University of Pretoria

where $E_g(0) = 1.1519$ eV is the energy gap at $T = 0$ K, $\alpha = 4.730 \times 10^{-4}$ eV K^{-1} and $\beta = 636$ K material constants for Si (Sze, Ng and Li, 2006).

At room temperature it was found that the band gap of Si decreases with increasing pressure at a rate of -2.4×10^{-6} eV kg^{-1} cm^{-2} (Paul and Warschauer, 1963).

The electron and hole mobility, two important semiconductor properties, depend on the band structure. For bulk grown Si, the hole mobility, μ_h , is 450 cm^2 V s^{-1} and the electron mobility, μ_e , is 1500 cm^2 V s^{-1} (Sze, Ng and Li, 2006).

2.2 The Schottky diode

The Schottky barrier diode, named after Walter H. Schottky (Schottky, 1942), is a fast switching device with a low forward voltage drop. The diode is formed by the junction of a metal and semiconductor. This junction gives rise to two possible metal-semiconductor contacts, Schottky and ohmic contacts. Schottky diodes are used for many types of electronics. Defect levels on and beneath the interface of the metal–semiconductor contact influence the properties of the Schottky diodes significantly and therefore Schottky diodes are also used for studying bulk defects in research.

2.2.1 The ideal Schottky diode

The ideal Schottky diode model describes the potential barrier formation at the metal-semiconductor interface in the absence of surface states. For the case of a uniformly doped n-type material, the Fermi level of the semiconductor is positioned higher than the Fermi level of the metal. The minimum energy required to remove an electron from the respective material is defined as the work function of the material and is calculated as the difference between the vacuum level and the Fermi level. In isolation, the work function of the semiconductor (ϕ_s) is less than the work function of the metal (ϕ_m). The difference between these work functions is called the built-in voltage (V_{bi}). The electron affinity (χ_s) is defined as the difference between the bottom of the conduction band and the vacuum level. The doping concentration of the semiconductor does not influence the electron affinity (Streetman, 2016).

When the two materials are in perfect contact, the difference in the work functions causes electrons to flow from the semiconductor to the metal. (See Figure 2.1.) The transfer of electrons builds up a negative charge on the metal surface equal to the positive charge on the semiconductor surface. Since the positive charge in the semiconductor is provided by ionized donors, which are present in a relatively low concentration, the positive charge in the semiconductor extends to a significant distance beneath the interface. This creates an electric field repelling electrons in the conduction band of the semiconductor forming the depletion region of width ω, where there are no electrons in the conduction band. Due to this electric field, the Fermi level of the semiconductor will be lowered relative to the Fermi level of the metal until they coincide preventing further flow of electrons. The Fermi level is lowered by an amount equal to the built in voltage (Streetman, 2016). The electrostatic potential due to the field is usually included in the energy diagram and leads to the parabolic bending of the bands in the depletion region.

© University of Pretoria

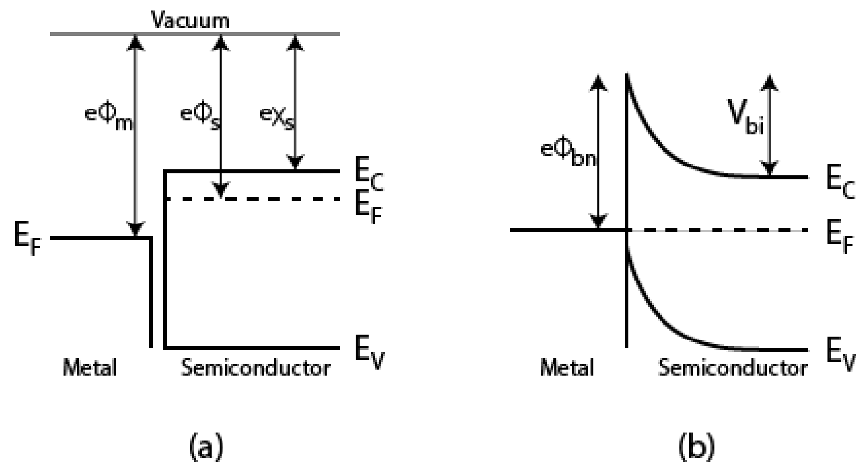

Figure 2.1: Energy diagram showing the formation of the ideal Schottky barrier. Metal and semiconductor are completely isolated (a) separated by a vacuum. Metal and semiconductor are in perfect contact (b) (Montanari, 2005).

Electrons deep in the semiconductor will experience a potential barrier (V_{bi}) when moving towards the metal caused by the bending of the bands. Electrons at the Fermi level of the metal will experience a potential barrier (ϕ_{bn}) when moving towards the semiconductor, equal to the difference between the semiconductor electron affinity and the metal work function (Streetman, 2016).

2.2.2 Zero, reverse and forward bias

When no bias is applied to the Schottky diode (see Figure 2.2), free electrons will transfer from the n-type semiconductor to the metal until a dynamic equilibrium is established. The number of electrons transferring from the metal to the semiconductor every second is equivalent to the number of electrons transferring from the semiconductor to the metal (Sze, Ng and Li, 2006).

Placing the system under forward bias (connection terminals shown in Figure 2.2) shifts the Fermi level of the semiconductor to a higher position relative to the metal. The barrier experienced by electrons traveling from the metal to the semiconductor remains unaltered. However, the barrier experienced by electrons from the semiconductor to the metal decreases with increasing forward bias. This allows for a greater net flow of electrons into the metal, increasing with forward bias. (Streetman, 2016).

Placing the system under reverse bias (connection terminals shown in Figure 2.2) lowers the Fermi level of the semiconductor relative to the metal. This causes a further bending in the conduction band, increasing the barrier height experienced by the electrons flowing from the semiconductor to the metal. As previously, the barrier experienced by the electrons flowing from the metal to the semiconductor remains unaltered with applied bias. This means the flow of electrons to the metal steadily decreases with increasing reverse bias, causing a net flow of electrons from the metal to the semiconductor, which increases asymptotically to a maximum, which is much less than the typical forward-bias current. The dielectric breakdown voltage limits the magnitude of the applied reverse bias. Breakdown occurs when surpassing the breakdown field within the semiconductor. The voltage at which this occurs, is defined as the breakdown voltage, the maximum voltage that can be applied in reverse bias before the system experiences an exponential increase in current flow. In practice one avoids this voltage as it can lead to rapid degrading in the rectifying properties of the barrier and cause irreversible damage to the Schottky diode (Streetman, 2016).

© University of Pretoria

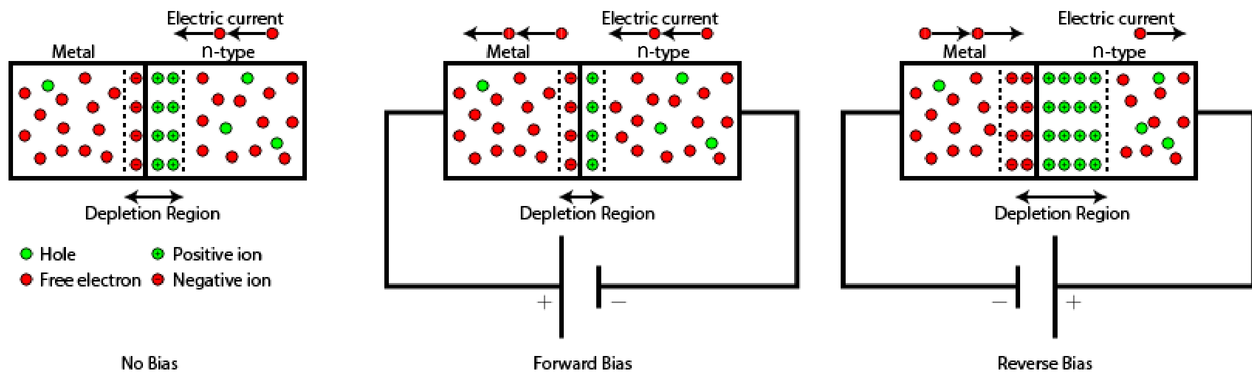

Figure 2.2: Diagram showing the effect of placing an unbiased Schottky diode (Left) under forward (Middle) and reverse (Right) bias.

2.3 Semiconductor defects

Real crystals (Si wafers) are finite; the surface atoms are incompletely bonded, containing multiple defects which influence the mechanical, optical and electrical properties of the semiconductor. In an ideal crystal lattice, defects are described as imperfections such as missing, foreign, misplaced or additional atoms causing discontinuity in the lattice repetition. These imperfections are introduced either during fabrication of electrical devices or during the growth of the semiconductor substrate, although some may also be introduced by radiation (Lannoo, 2012). They can be categorized into four categories: volume, area, line and point defects.

Crystal defects play the dominant role during processing and are the basis of any technological application. They may introduce energy states within the semiconductor band gaps as either shallow or deeps levels.

2.3.1 Defects

Point defects are localized, only involving a few nearest neighbour atoms and do not expand within any dimension of space. The simplest defects are shown in Figure 2.3 and are described as follows:

- Foreign interstitial: A foreign atom occupying a site between regular lattice sites.
- Self-interstitial: A crystal lattice atom occupying a site between regular lattice sites.
- Vacancy: A lattice site missing an atom.
- Substitutional: A foreign atom occupying a lattice site.
- Frenkel pair: Self-interstitial responsible for the vacancy near it.

(Föll, Gösele and Kolbesen, 1981).

© University of Pretoria

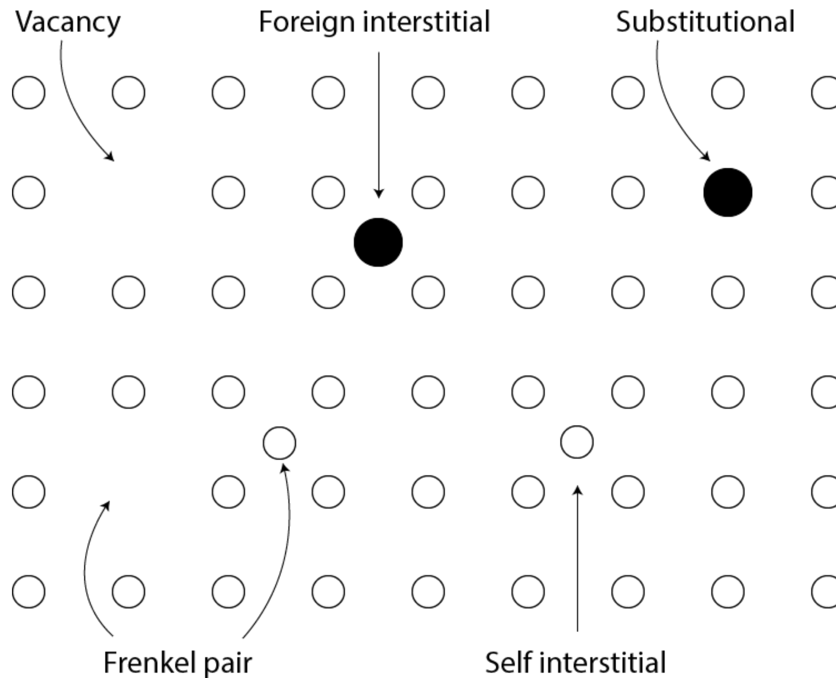

Figure 2.3: Simplified diagram representing point defects within crystals

Line defects are known as dislocations or one-dimensional defects. These are generally introduced by applying stress on the crystal. They can be summarized into two main categories: edge and screw dislocations.

- Edge dislocation: An extra half plane of atoms are inserted into a uniform crystal lattice.
- Screw dislocation: A portion of the crystal undergoes sheering and shifted relative to the other portion of the crystal.

(Vogel, Pfann, Corey and Thomas, 1953).

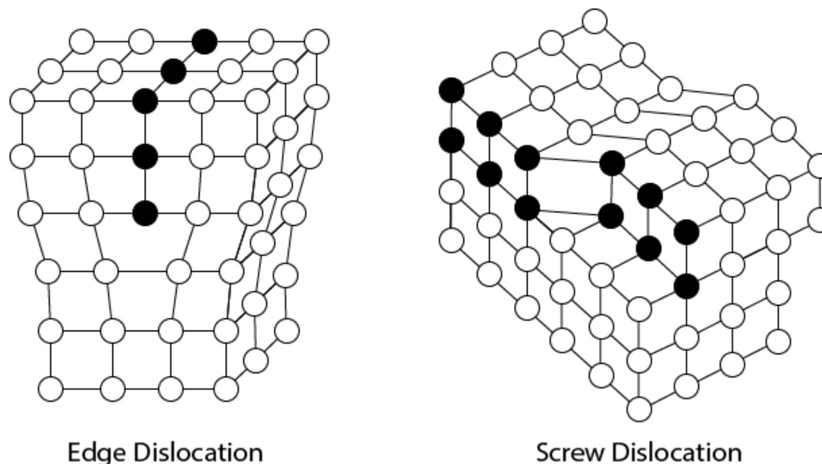

Figure 2.4: Simplified diagram representing dislocations within crystals

Area defects, also known as planar (2D) defects are large lattice discontinuities across a plane. These typically appear during crystal growth and come in the form of grain boundaries and stacking faults.

© University of Pretoria

- Grain boundary: The interface between two boundaries from two crystallites. The crystal is rotated about a specific axis categorizing it either as a tilt or twist boundary. Parallel rotation around the boundary plane is categorized as a tilt boundary and a perpendicular rotation around the boundary plane is categorized as a twist boundary.
- Stacking fault: The interruption of the stacking sequence of atomic layers (Figure 2.5). Intrinsic stacking fault occurs when a part of a layer is missing. Extrinsic stacking faults occurs when an extra plane is inserted between two layers.

These area defects are not usable for manufacturing of integrated circuits, thus, crystals containing these defects are discarded.

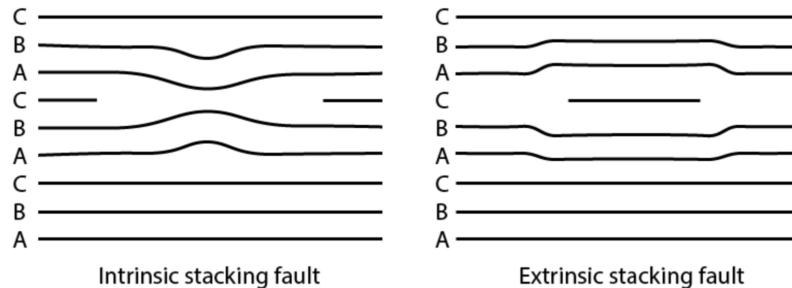

Figure 2.5: Simplified diagram representing intrinsic and extrinsic stacking faults

Volume defects arise due to the inherent solubility of dopants or impurities in the lattice. The lattice can accept a specific concentration of impurities in solid solution (McCluskey and Haller, 2018).

2.3.2 Radiation induced defects

High energy particles (radiation) introduce a variety of defects by inducing damage in the semiconductor material. The incident particle interacts with the nuclei of the lattice atoms to cause bulk damage which in most cases is irreversible.

The minimum required energy to remove a silicon atom from a lattice site (E_d) is approximately 25 eV. Electrons require at least 255 keV to provide recoil energy of that magnitude during collision. Protons and neutrons require less energy, approximately 185 eV, due to their higher mass. Single vacancy self-interstitial pairs are created when the recoil atom receives small amounts of energy, e.g. from low-energy x-ray photons or electrons from electromagnetic radiation (Van Lint *et al.*, 1980).

The recoil atom can cause further damage if it receives enough energy during the collision with the incident particle. A Si atom needs to receive at least 5 keV of energy during the collision to displace another Si atom from its lattice site. One can deduct from this value that the threshold energy of more than 35 keV is required for protons or neutrons, and a threshold energy of more than 8 MeV is required for electrons. This results in the formation of dense agglomeration of defects since these displacements are very closely positioned. These are usually referred to as defect clusters as they have high defect density. These clusters have a greater effect on the properties of semiconductor devices compared to point defects (Van Lint *et al.*, 1980).

The following are important defects formed during irradiation and will be discussed in full detail in Chapter 3:

© University of Pretoria

- Di-vacancy: Two neighbouring atoms removed from lattice sites. This can be created as either a primary defect when the collision cascades are dense enough, or as a secondary defect when two single vacancies pair up through diffusion.
- E-centre: Substitutional donor atom with a neighbouring vacancy. This can be created either as a primary defect if the neighbouring atom is removed by collision or as a secondary defect by capturing a mobile vacancy.
- A-centre: Oxygen atom with a neighbouring vacancy. Similar to the E-centre, this can be created as a primary or secondary defect.

These complexes and other more complicated defects will be discussed in full detail later in this study.

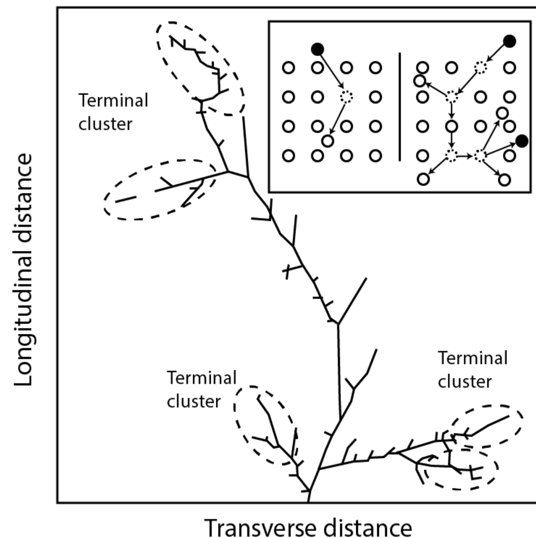

Figure 2.6: Diagram representing the development of clusters due to an energetic particle entering the crystal from the bottom of the figure. Insert image shows the displacement of atoms when exposing the substrate to electromagnetic (left) and heavy particle (right) radiation.

2.3.3 Deep- and shallow-levels

Impurity atoms are introduced to semiconductors to change the conductivity (p-type or n-type) of semiconductors. Relative to the conduction and valance band, these levels will be classified either as shallow or deep levels.

Defects with energy levels close to the edges are classified as shallow level defects (see Figure 2.7). The hydrogenic model usually describes these defects well and the associated wave functions are not localized. Shallow levels will release carriers into the semiconductor due to their easily ionized nature. If the material is doped with donor atoms, these atoms introduce electrons into the conduction band forming a positively charged ionized donor. Group V atoms are commonly used as donor atoms for Group IV semiconductors. In contrast, for p-type material, the material will be doped with acceptor atoms introducing holes within the valance band, which are typically from Group III.

Defects categorized as deep levels have much more localised wave functions and typically give rise to levels that are deeper in the band gap. These deep levels will bind with electrons or holes, interfering with electrical transport and other electrical properties of the material. Furthermore, they

© University of Pretoria

decrease the minority carrier lifetime by acting as recombination centres, allowing electrons and holes to recombine. In turn this increases the noise in photodiodes and transistors and decreases the efficiency of solar cells (Poole, 2014).

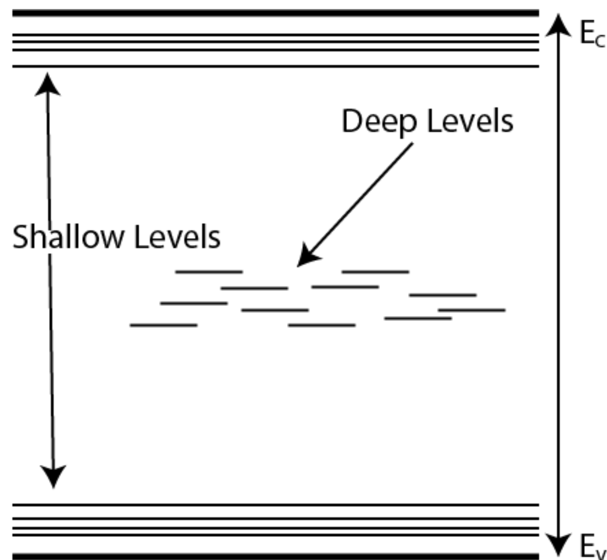

Figure 2.7: Simplified energy diagram showing the position of deep and shallow levels within the band gap. E_C and E_V are the conduction band and valence band respectively. Deep levels here are shown to be more localized while shallow levels have an extended nature.

2.4 Deep-level transient spectroscopy

Deep-level transient spectroscopy (DLTS) is a method introduced by D.V. Lang in 1974 for characterizing and observing deep level impurities in semiconductors. DLTS measures the capacitance of the diode at a high frequency (MHz) and observes the capacitance transient due to emission of carriers in a p-n junction, Schottky diode or metal oxide semiconductor (MOS) as a function of temperature.

DLTS is rapid, easy to analyse and sensitive enough to fulfil all the requirements for complete and quick characterization of deep levels. It is able to distinguish between minority and majority carrier traps and is spectroscopic, as it resolves signals produced by different kinds of traps (Sah and Walker, 1973). There are many variants to the technique, all with the basis of filling the deep levels with free carriers either optically or electrically and observing the carriers being emitted. The technique is used to establish the capture rates, various energies, concentration and other fundamental properties of defects. The properties are used in part to identify the structure of defects and may be used to find various techniques for manipulating properties of electrical devices.

2.4.1 Capacitance signal

The DLTS technique can be applied to any device with a depletion region. This includes but is not limited to the p-n junction diode, Schottky diode and MOS devices. Figure 2.8 shows a simplistic circuit diagram for measuring these devices and where in the device the depletion region would be found.

© University of Pretoria

When voltage across the metal-semiconductor junction is modified, there is a corresponding change with the depletion region width. As the depletion width changes, the number of free charge carriers changes on both sides of the junction, cause a change in the capacitance. The junction capacitance and the diffusion capacitance both contribute to the change in capacitance. While the system is under reverse bias, the junction capacitance would dominate, which is due to the change in the depletion width. While the system is under forward bias, the diffusion capacitance would dominate, which is caused by the change in concentration of minority carriers.

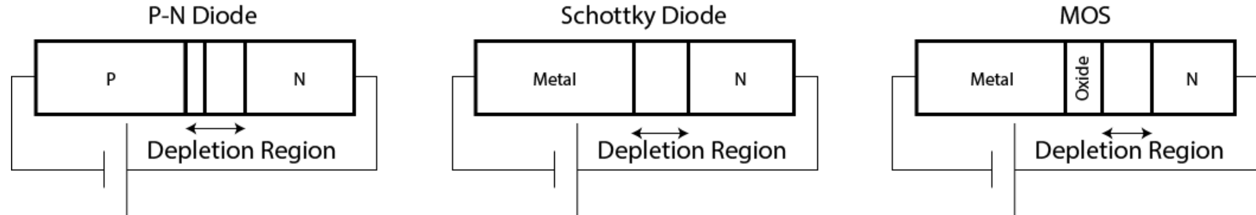

Figure 2.8: Diagram depicting the position of the depletion region for the p-n diode, Schottky diode and the MOS diode connected in a circuit to generate a signal used in DLTS.

Suppose, in a metal – n-type semiconductor junction, there are deep levels in the semiconductor and they have an energy of E_T relative to the conduction band. In the undisturbed state, there will be no net flow of electrons across the junction. The hole and electron densities in the depletion region are negligible. Shockley and Reed (1952) determined the relationship between the total density of deep states (N_T) and the density of filled traps (n_T) with a hole emission rate of e_p and an electron emission rate of e_n to be

$$n_T = \left(\frac{e_p}{e_n + e_p}\right) N_T. \tag{4}$$

Disturbing this system will cause a change in the nett charge of the depletion region, and with that a corresponding change to the capacitance. To a first approximation, the charge due to the defects may be added to that due to the ionised donors.

The full process of the DLTS cycle (Lang, 1974) for obtaining the capacitance transient is shown in Figure 2.9. The system is kept under reverse bias (V_R) in a quiescent state (Figure 2.9 (a)). During this step there are no free charge carriers available for the traps to capture, so the traps in the depletion region are empty. During the second step (Figure 2.9 (b)) the applied bias is reduced to zero by using a filling pulse. The depletion width decreases, giving rise to a sharp rise in capacitance. At the same time, the decreased depletion width allows electrons to be captured by the empty deep levels. If the system is at sufficiently low temperature, the re-emission of electrons can be neglected. The rate of density of traps being filled with a capture time constant c_n for electrons can be represented by:

$$\frac{dn_T}{dt} = c_n(N_T - n_T) \tag{5}$$

From this it can be seen that if a long enough filling pulse ($t \gg c_n^{-1}$) is applied to the system, all the traps will be filled (i.e. $n_T = N_T$).

During the third step (Figure 9 (c)), the filling pulse is removed, restoring the system to the former applied bias. The capacitance immediately drops to a value slightly lower than its earlier reverse-

© University of Pretoria

bias value due to electrons trapped in the depletion region. The system is kept in an undisturbed state with a reverse bias in the fourth step (Figure 9 (d)). Here the trapped electrons are emitted thermally, thereby reducing the concentration of filled traps, which in turn causes the capacitance to decay to its quiescent reverse-bias value. The rate at which electrons are emitted from the density of traps can be expressed as follows:

$$\frac{dn_T}{dt} = e_p N_T - \left(e_n + e_p\right) n_T. \tag{6}$$

This can be solved to give the following solution:

$$\begin{aligned} n_T &= \frac{N_T}{e_n + e_p}\left(e_p + e_n e^{-(e_n+e_p)t}\right) \qquad && t \geq 0 \\ n_T &= N_T && t < 0 \end{aligned}, \tag{7}$$

where $t < 0$ is the period before the filling pulse is removed and all the traps are assumed to still be full. The solution thus shows that the density of filled traps will decay exponentially with the time constant given by:

$$\tau = \frac{1}{e_n + e_p}. \tag{8}$$

For the case of an electron-emitting centre, the assumption $e_n \gg e_p$ holds valid, reducing the solution obtained in Equation (7) to:

$$\begin{aligned} n_T &= N_T e^{-e_n t} \qquad && t \geq 0 \\ n_T &= N_T && t < 0 \end{aligned}. \tag{9}$$

The amplitude of the transient will thus give a measure of the trap concentration while the time constant will give the rate of electron emission:

$$\tau = \frac{1}{e_n}. \tag{10}$$

The capacitance of a Shottky diode can be considered to be the same as that of a parallel plate capacitor. For an n-type Shottky diode the capacitance can be written as follows:

$$C = \frac{\epsilon A}{\omega} = \frac{\epsilon A}{\sqrt{\frac{2\epsilon(V_b - V)}{q(N_D - n_T)}}}, \tag{11}$$

where A is the junction area with ω the depletion width. N_D is the donor concentration, V_{bi} is the built-in voltage, V is the applied voltage, and ε is the permeability of the semiconductor.

Following a first order series expansion of Equation (8) about n_T at a reverse bias of V_R, assuming that $n_T \ll N_T$, substitution of Equation (6) and taking into consideration of the time dependence in Equation (7), one obtains:

© University of Pretoria

$$C(t) = C_0 \left(1 - \frac{N_T}{2N_D} e^{-\frac{t}{\tau}}\right), \tag{12}$$

where C_0 is the quiescent capacitance at a reverse bias of V_R. This equation shows that from the change in capacitance observed due to the pulsing bias, one can determine the emission rates and the concentration of deep levels in a Schottky junction (Kosyachenko, 2015).

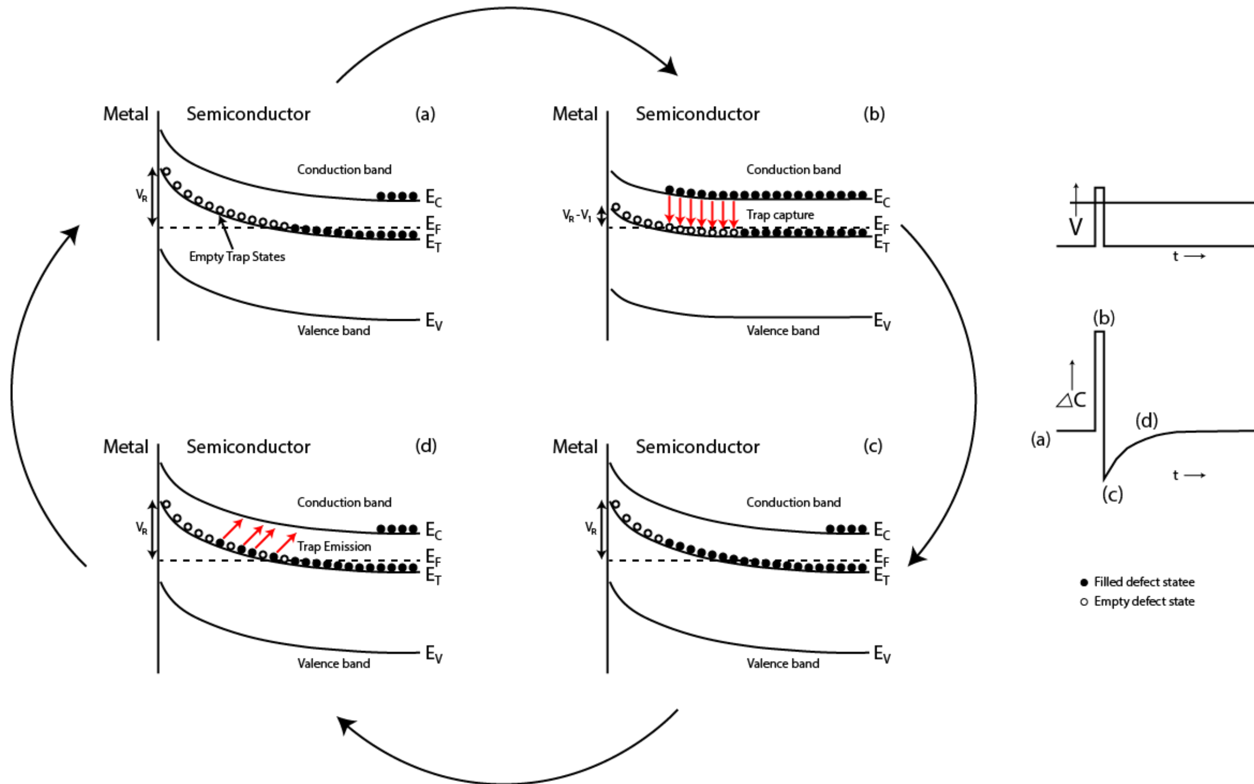

Figure 2.9: Basic process of a DLTS cycle and the capacitance transient obtained from the cycle (Lang, 1974).

2.4.2 Thermal DLTS signal processing

The isothermal capacitance transient described in Equation (11) can be obtained by applying a single DLTS cycle described in Section 2.4.1 at a constant temperature. Analysing the resultant transient will give the emission rate of the carriers for that temperature. Conventional DLTS, also known as a rate window scan, measures the emission rate of carriers with changing temperature for a set rate window. However, this is a time consuming technique to obtain a wide range of emission rates and analysis becomes complicated if many deep levels are present (Lang, 1974). It is none the less insightful to describe the process.

Setting up the rate window is one of the essential features for this technique to work. The rate window needs to ensure that the measuring apparatus only gives an output when the transient has an emission rate corresponding with the rate window. The amplitude of the transient is proportional to the output, thus, by varying the temperature over a large interval, the signal will peak when the emission rate is equal to the rate window and information relating to the thermal activation energies and concentration of the deep levels can be obtained.

© University of Pretoria

Traditionally, the dual-gate boxcar integrator is one of the most widely used methods for obtaining this time filter. The boxcar measures the capacitance at two gates set up at times t_1 and t_2. The DLTS signal $S(T)$ is obtained from the calculated difference between these measured capacitances ($C(t_1)$-$C(t_2)$). Substituting capacitance transient described in Equation (11) into this definition gives:

$$S(T) = \Delta C(T) = \Delta C_0 \frac{N_T}{2N_D} \left(e^{-\frac{t_1}{\tau}} - e^{-\frac{t_2}{\tau}} \right), \tag{13}$$

where ΔC_0 is the capacitance difference measured at $t = 0$.

The difference in measured capacitance as a function of temperature can be seen in Figure 2.10, which shows the formation of a bell curve. From this we can see that for some time constant τ_{max}, Equation (13) has a maximum $S(T)_{max}$. To determine this maximum signal we first need to consider that there is a high and low temperature for which there will be no measurable change in the capacitance ($S(T) = 0$). When the temperature is high enough the transient will complete before passing through the two gates, while at a low enough temperatures the change between the gates become negligibly small. However, between these two extremes, there is a transient for some time constant τ_{max}, for which the signal is a maximum. By differentiation Equation (13) with respect to t, we obtain τ_{max}.

$$\tau_{max} = \frac{t_2 - t_1}{\ln\left(\frac{t_2}{t_1}\right)}. \tag{14}$$

Further substituting this into Equation (13) we obtain $S(T)_{max}$:

$$S(T) = \Delta C(T) = \Delta C_0 \frac{N_T}{2N_D} \left(e^{-\frac{\ln\left(\frac{t_2}{t_1}\right)}{\frac{t_2}{t_1} - 1}} - e^{-\frac{\ln\left(\frac{t_2}{t_1}\right)}{1 - \frac{t_1}{t_2}}} \right). \tag{15}$$

This shows clearly that the peak height is dependent only on the ratio of the time gate positions and that the defect concentration is proportional to S (Kosyachenko, 2015). The defect concentration N_T can now be directly obtained from the DLTS peak height. Assuming all traps have been filled, it is possible to obtain the concentration by rewriting Equation (12) as follows:

$$\frac{\Delta C}{C_0} = \frac{N_T}{2N_D} \tag{16}$$

© University of Pretoria

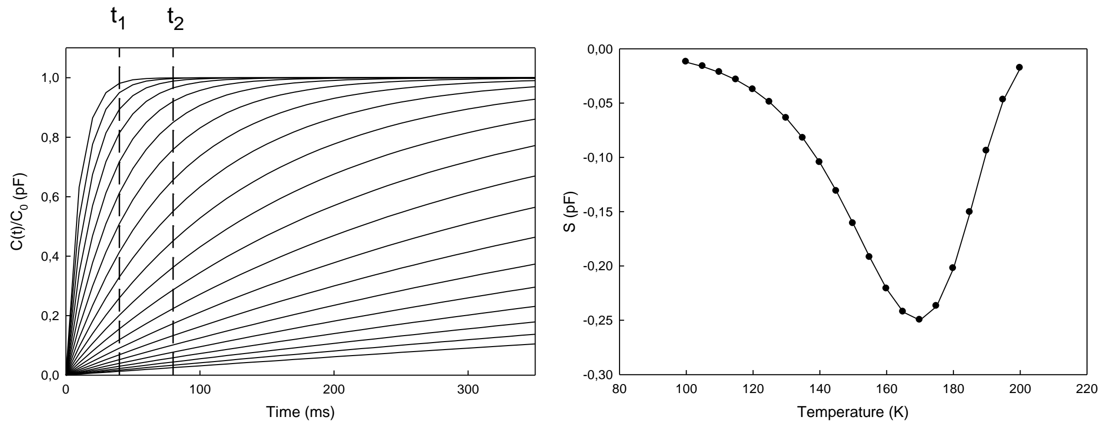

Figure 2.10: Simplified simulated graphs showing double-boxcar analysis of temperature-scanned DLTS measurements of a single deep level. Capacitance transients (left) were generated for different temperatures. The difference in capacitance at two times, t_1 and t_2, were calculated and plotted as a function of temperature on the right (Zurich Instrument, 2017).

2.4.3 Laplace DLTS

Laplace DLTS (L-DLTS) overcomes the resolution problem seen with conventional DLTS. In contrast to temperature scanned DLTS, this technique measures multiple transients at a set temperature. It was proposed by Dobaczewski in 1994 that an observed transient is the result of multiple transients measured at a set temperature. This is represented by:

$$f(t) = \int_0^{\infty} F(s) e^{-st} ds, \tag{17}$$

where $F(s)$ is the spectral density function and $f(t)$ is the observed transient. By averaging multiple transients, the signal-to-noise ratio greatly improves allowing for advanced mathematical techniques to be used on it. Performing an inverse Laplace transform on the function in Equation (17), the spectrum of emission rates can be obtained. Great care has to be taken during the numerical inversion of a Laplace transformation on a real life problem, as it is an “ill posed” problem (Dobaczewski *et al*., 1994). The accuracy of the calculated emission rates is highly dependent on the signal-to-noise ratio of the averaged transient. During experimentation, the equipment used, the quality of the sample, the number of transients averaged and other external factors influence the results of the calculation. In contrast to conventional DLTS, the defect concentration is directly related to the area under each emission rate peak (Dobaczewski *et al*., 2004).

L-DLTS identifies and accurately calculates multiple emission rates observed under what appears to be a single peak when observed with conventional DLTS. However, the technique does not come without limitations, as accurate distinction between emission rates less than a factor 6 apart becomes increasingly complicated (Dobaczewski *et al.*, 2004).

© University of Pretoria

2.5 DLTS defect profiling techniques

The DLTS technique can be used to study different electrical properties of deep levels present in semiconductors. This includes but is not limited to electron emission activation energy, capture cross-section, depth profiling, electric field effect and annealing activation energy. Some of these electrical properties and how to obtain them experimentally will be summarized in this section.

2.5.1 Electron emission activation energy

Activation energies are based off the Arrhenius law principle proposed by Svante Arrhenius (1889). The result is the combination of Boltzmann distribution and the concept of activation energy. The rate constant (k) and the activation energy (E_α) relationship can be expressed as:

$$k = A\,e^{-\frac{E_\alpha}{k_B T}}, \tag{18}$$

with A the frequency factor, T the absolute temperature and k_B the Boltzmann constant.

The electron emission activation energy can be determined using both conventional and L-DLTS techniques. It was calculated in Section 2.4.2 that for a set rate window, there is a maximum peak height over a temperature region. By changing the t_1 and t_2 settings, different rate windows are applied to obtain different temperatures at which the maximum is observed. Similarly, L-DLTS measures and calculates the emission rate for a set temperature. Using the emission rates and their corresponding temperatures, a linear plot should be obtained when plotting on a graph of $\log\left(\frac{e}{T^2}\right)$ vs $\frac{1}{T}$, as seen in Figure 2.11. The activation energy is calculated from the gradient with the apparent capture cross-section calculated from the y-intercept. (Lang, 1974)

.

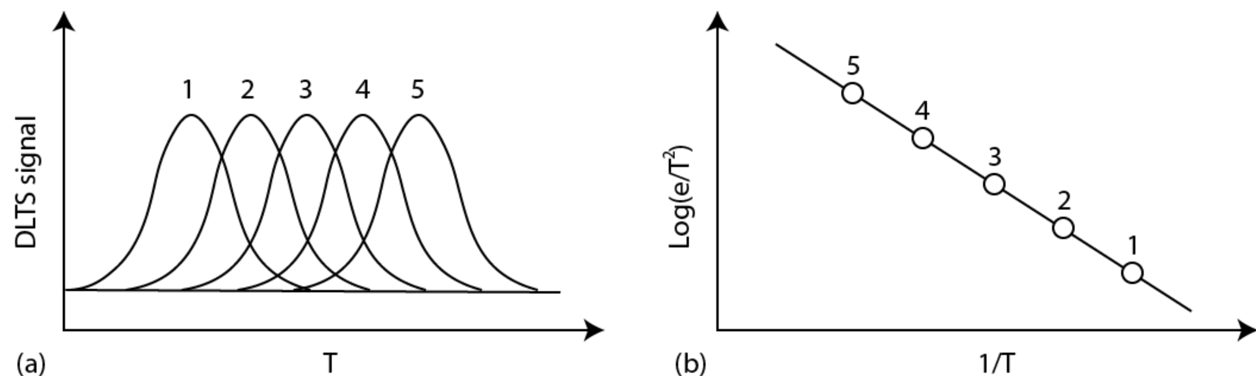

Figure 2.11: (a) Conventional DLTS signals (1-5) obtained over a temperature region for different rate windows, leading to the Arrhenius plot (b) obtained from the temperature and emission rate of each defect. (After Lang, 1974)

2.5.2 True capture cross-section

In Section 2.5.1, the capture cross-section can be obtained by extrapolating the Arrhenius plot to $1/T = 0$. This is referred to be the apparent capture cross-section as it may not correspond to the true capture cross-section. Often, the extrapolation is over a larger distance than the measurements, so small extrapolation errors would lead to significant errors. In the case of a capture barrier being present, the capture cross-section will be temperature dependent invalidating this approach. Thus,

© University of Pretoria

the capture cross-section needs to be directly measured over a wide range of temperatures. (Lang, 1974.)

By measuring the concentration of filled defects as a function of filling pulse width, the true capture cross-section can be obtained. Increasing the filling pulse width increases the fraction of filled defects until a maximum is observed due to all traps being filled by the single, long pulse. Figure 2.12 shows the peak height (S) increasing with filling pulse (t_{pulse}), with their relationship expressed as:

$$\frac{S}{S_\infty} = 1 - e^{-\frac{t_{pulse}}{\tau}} . \tag{19}$$

Here S_∞ is the maximum peak height obtained after applying a filling pulse long enough to fill all available traps. Substituting in Equation (15), this equation can be rewritten in terms capacitance measurements for experimentation. The theoretical shape for the measured capacitance (ΔC) versus $\log(t_{\text{pulse}})$ is that of a logistic curve with the slope giving $1/\tau$.

Now the capture cross-section (σ_T) for a set temperature (T) is described by the following equation:

$$\sigma_T = \frac{1}{\tau n \langle v_{th} \rangle} , \langle v_{th} \rangle = \sqrt{\frac{8Tk_B q}{\pi m_e}} . \tag{20}$$

In this case the carrier concentration n is approximately equal to N_D which can be calculated from capacitance-voltage measurements, $\langle v_{th} \rangle$ is the thermal velocity of electrons, q is the electron charge and m_e is the effective mass of an electron in the semiconductor.

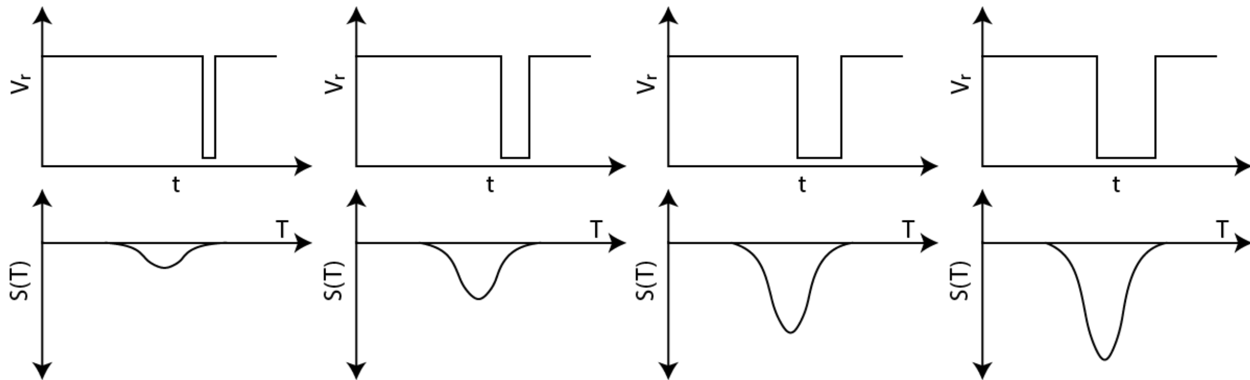

Figure 2.12: Changing the filling pulse width and the effect on the peak obtained for capture cross-section measurements. (After Lang, 1974)

2.5.3 Depth profiling

The defect concentration is directly proportional to the DLTS peak height. It can be calculated from the measured change in capacitance using Equation (16). Only if $\Delta C \ll C$ and if the pulse is large and long enough to completely fill the defects does it hold. This was shown to only be an approximation, resulting in serious errors when used inappropriately for determining the concentrations of defects deep in the band gap at low reverse bias voltages. (Zohta and Watanabe, 1982.)

© University of Pretoria

A more accurate representation of the defect concentration can be obtained by considering the so-called λ effect. This effect considers the region a distance λ shallower than the depletion region where the defect level is still beneath the Fermi level. Here traps are occupied and do not contribute to change in capacitance. The width is given by

$$\lambda = \left[\frac{2\varepsilon(E_F - E_T)}{q^2 N_D}\right]^{\frac{1}{2}}, \tag{21}$$

where E_F is the Fermi level, E_T is the energy of the deep-level trap, q is the electron charge, N_D is the ionized shallow impurity concentration and ε is the dielectric constant of the semiconductor.

The depth profiling technique used in this study requires a variable filling pulse and a fixed reverse bias. In this method the filling pulse (V_p) is changed by small increments while monitoring the incremental change in capacitance $\delta(\Delta C)$ as shown by Zohta and Watanabe (1982). This incremental change due to the increment in the pulse can be expressed by

$$\frac{\Delta C}{C} = \left(\frac{E}{q\omega^2 N_D}\right)\frac{N_T(x)}{N_D(x)}\,\delta V_p\,, \tag{22}$$

where ω is the depletion width and x is the depth below the junction. Capacitance-voltage measurements will give the shallow impurity profile $N_D(x)$. Zohta and Watanabe (1982) calculated the total signal due to the majority carrier pulse by applying a double integration of the Poisson equation. The correct deep-level concentration was found to be expressed as

$$N_T = \frac{2\Delta C N_D(x)}{C}\left[\left(\frac{x-\lambda}{x}\right)^2 - \left(\frac{x_p-\lambda_p}{x}\right)^2\right]^{-1}, \tag{23}$$

where $x - \lambda$ is the depletion width before applying a filling pulse, $x_p - \lambda_p$ is after applying the filling pulse, with λ_p the value of λ_p during the pulse.

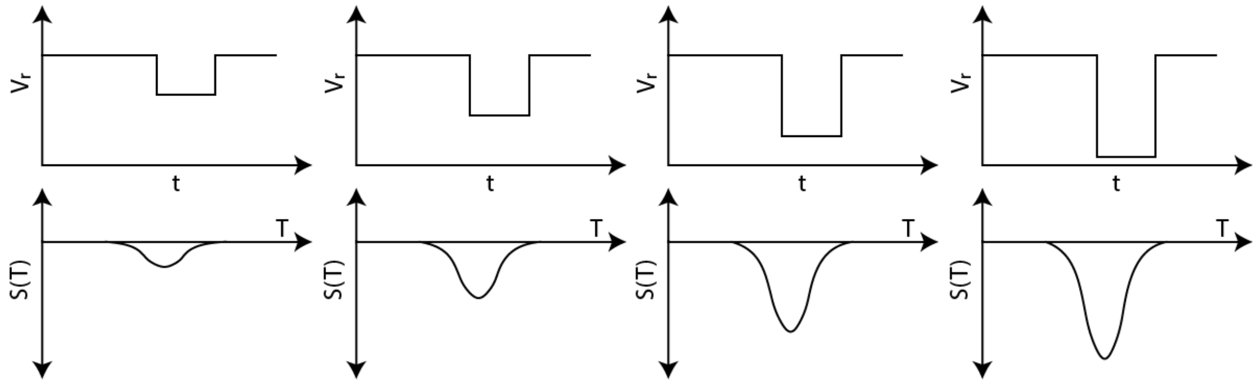

Figure 2.13: Changing the filling pulse height and the effect on the peak obtained for depth profiling.

2.5.4 Annealing kinetics

The annealing profile is the time dependent characteristic temperature at which a defect is reduced. The two main processes according to which defects anneal are diffusion and dissociation. Diffusion is the migration of defects within the semiconductor to either the surface or to the grain boundaries. They may also be trapped by other defects or impurities through hydrogen passivation, complex

© University of Pretoria

formation or direct recombination of the interstitial and vacancy. The charge state and the thermal energy of the semiconductor crystal determines the migration ability of the defect. Dissociation is the breaking up of defect complexes, which may also be charge-state dependent.

Isothermal and isochronal annealing are two main techniques used for profiling deep levels, with the latter used as a guideline for the former. It was proposed by Svante Arrhenius in 1889 that the temperature dependent reaction rate formula can be obtained by combining the concept of activation energy and the Boltzmann distribution. This equation is known as Arrhenius' Law which states that the rate constant (k) can be written as follows:

$$k = Ae^{-\frac{E_\alpha}{k_B T}}, \tag{24}$$

with E_α the activation energy, T the absolute temperature, A the frequency factor and k_B the Boltzmann constant.

Each annealing process is characterized by an activation energy (E_α) with the reaction rate increasing with temperature. With isothermal annealing, the decrease in defect concentration can be monitored for a fixed temperature, T. Assume the concentration of defects to be N_T, for any unit of time, the concentration of defects annealed will be proportional to the concentration of defects $f(N_T)$ present at time t. This relationship is described as follows:

$$\frac{dN_T}{dt} = -kf(N_T) \tag{25}$$

with k the annealing rate constant. The first and second order annealing kinetics would be described by $f(N_T) = N_T$ and $f(N_T) = N_T^2$ respectively. The solution to Equation (25) for first order annealing kinetics is written relative to the initial defect concentration $N_T(0)$ as:

$$N_T(t) = N_T(0)e^{-kt}, \tag{26}$$

with t the total annealing time. k is the temperature dependent annealing rate constant and can be obtained from the Arrhenius equation

$$k(T) = k(0)e^{-\frac{E_a}{k_B T}} \tag{27}$$

with $k(0)$ the pre-exponential constant which, in the case of a defect in a crystal, is related to the vibrational frequency.

Experimentally, isothermal annealing profiles are measured and plotted as $\ln(N_T)$ vs. t. The gradient obtained from this linear plot is the annealing rate constant at the temperature at which the profile was measured. After obtaining k values at different temperatures, these can be plotted as a function $\ln[k(T)]$ vs. T^{-1}. The activation energy can be calculated from the gradient of this linear plot, with the y-intercept representing the frequency factor. The activation energy is related to the minimum energy required to remove the defect from the crystal while the frequency factor can give additional information on the mechanism according to which the defect is removed (i.e. dissociation, recombination, diffusion, etc.).

© University of Pretoria

2.6 References

Arrhenius, S., 1889. Über die Dissociationswärme und den Einfluss der Temperatur auf den Dissociationsgrad der Elektrolyte. *Zeitschrift für Physikalische Chemie*, 4U(1).

Capper, P., Rudolph, P. and Scheel, H., 2010 *Crystal Growth Technology: Semiconductors and Dielectrics*. New York: Wiley.

Dobaczewski, L., Kaczor, P., Hawkins, I. and Peaker, A., 1994. Laplace transform deep-level transient spectroscopic studies of defects in semiconductors. *Journal of Applied Physics*, 76(1), pp.194-198.

Dobaczewski, L., Peaker, A. and Bonde Nielsen, K., 2004. Laplace-transform deep-level spectroscopy: The technique and its applications to the study of point defects in semiconductors. *Journal of Applied Physics*, 96(9), pp.4689-4728.

Föll, H., Gösele, U. and Kolbesen, B., 1981. Microdefects in silicon and their relation to point defects. *Journal of Crystal Growth*, 52, pp.907-916.

Kittel, C., 2005. *Introduction To Solid State Physics*. New York: Wiley.

Kittel, C. and Fong, C., 2010. *Quantum Theory Of Solids*. New York, N.Y.: Wiley.

Kosyachenko, L., 2015. *Solar Cells - New Approaches And Reviews*. InTech, pp.199-220.

Kuech, T. and Nishinaga, T., 2015. *Handbook Of Crystal Growth*. Amsterdam: Elsevier.

Lang, D., 1974. Deep-level transient spectroscopy: A new method to characterize traps in semiconductors. *Journal of Applied Physics*, 45(7), pp.3023-3032.

Lannoo, M., 2012. *Point Defects In Semiconductors I*. New York: Springer-Verlag Berlin An.

McCluskey, M. and Haller, E., 2018. *Dopants And Defects In Semiconductors*. 2nd ed. New York: CRC Press.

Montanari, S., 2005. *Fabrication And Characterization Of Planar Gunn Diodes For Monolithic Microwave Integrated Circuits*. Jülich: Forschungszentrum, Zentralbibliothek.

Patterson, J. and Bailey, B., 2019. *Solid-State Physics*. Cham: Springer International Publishing AG.

Paul, W. and Warschauer, D., 1963. *Solid State Physics Under Pressure*. New York: McGraw-Hill.

Poole, J., 2014. *Encyclopedic Dictionary Of Condensed Matter Physics*. Amsterdam: Elsevier Science.

Sah, C. and Walker, J., 1973. Thermally stimulated capacitance for shallow majority-carrier traps in the edge region of semiconductor junctions. *Applied Physics Letters*, 22(8), pp.384-385.

Seeger, K., 1997. *Semiconductor Physics*. Berlin: Springer.

Shockley, W. and Read, W., 1952. Statistics of the Recombinations of Holes and Electrons. *Physical Review*, 87(5), pp.835-842.

Schottky, W., 1942. Vereinfachte und erweiterte Theorie der Randschicht-gleichrichter. *Zeitschrift für Physik*, 118(9-10), pp.539-592.

© University of Pretoria

Smith, R., 1987. *Semiconductors*. Cambridge: Cambridge Univ. Press.

Streetman, B. and Banerjee, S., 2016. *Solid State Electronic Devices*. Harlow, Essex: Pearson Education Limited.

Sze, S., Ng, K. and Li, Y., 2006. *Physics of semiconductor devices*. New York: Wiley

Van Lint, V., Flanagan, T., Leadon, R., Naber, J. and Rogers, V., 1980. *Mechanisms Of Radiation Effects In Electronic Materials*. New York: Wiley & Sons.

Vogel, F., Pfann, W., Corey, H. and Thomas, E., 1953. Observations of Dislocations in Lineage Boundaries in Germanium. *Physical Review*, 90(3), pp.489-490.

Zohta, Y. and Watanabe, M., 1982. On the determination of the spatial distribution of deep centers in semiconducting thin films from capacitance transient spectroscopy. *Journal of Applied Physics*, 53(3), pp.1809-1811.

Zurich Instrument (2017). *Laplace Deep Level Transient Spectroscopy using the MFIA*

© University of Pretoria

3 Radiation-induced defects within silicon

3.1 Reactions of carbon-interstitials (C_i)

Carbon is naturally introduced during the growth phase of the Si substrate as C_s atoms. The carbon is produced by the graphite components in the equipment, the poly-crystalline starting material or from the gaseous contamination during growth (Kolbesen and Mühlbauer, 1982).

Carbon-related reactions play a vital role in radiation damage in Si. The reaction of interstitial carbon atoms (C_i) are based on three assumptions which are valid for low irradiation fluence. The first is that in high resistivity silicon crystals, the substitution carbon (C_s) atoms are the main traps for interstitial silicon (Si_i) atoms. Secondly, the only source of mobile carbon species that are responsible for the formation of carbon-related complexes which are stable at room temperature are isolated carbon atoms in interstitial positions created by the Watkins replacement mechanism. (Watkins, 1965). Finally, the kinetics of the formation of carbon-related complexes are controlled by the C_i diffusion coefficient and the capture radii of substitutional carbon, oxygen and doping materials (Makarenko *et al*., 2007). The Watkins replacement mechanism for the formation of C_i in Si is described by the following reaction:

$$C_s + Si_i \rightarrow C_i + Si_s. \quad (28)$$

Si_i atoms are introduced by exposing the material to an external source of high energy particles. The Si_i are mobile in the crystal and migrate to the position of a C_s, where the Si_i replaces the C_s to form the substitutional Si (Si_s) and to release C_i into the crystal. The mobile C_i will then react with other impurities, with the most common reactions described as follow:

$$C_i + O_i \rightarrow C_iO_i \quad (29)$$

$$C_i + C_s \rightarrow C_iC_s \quad (30)$$

$$C_i + P_s \rightarrow C_iP_s \quad (31)$$

(Khirunenko *et al*., 2005).

In p-type material the mobility of Si_i atoms is very low at room temperature which results in a slow reaction rate for the formation of C_i and other C_i-related complexes described above. However, this can be stimulated by the injection of electrons allowing greater diffusion rates of self-interstitials even at liquid nitrogen temperatures (Makarenko *et al*., 2009).

.

© University of Pretoria

3.1.1 Carbon-interstitial (C_i)

The sources of C_i atoms in Si were listed in Section 3.1. In an ideal substrate, absent of all dopants except carbon, C_i may only react with other carbon atoms or intrinsic defects (Chappell and Newman, 1987). The first C_i point defect was detected by infrared spectroscopy (IR) giving rise to the 922 and 932 cm^{-1} local-mode absorption bands (at 77K) (Stein and Vook, 1969). The configuration of the point-group symmetry for the positive state (Si-G12) was later observed in EPR spectroscopy by Watkins and Brower (1976). The symmetry was described as D_{2v}, an interstitial carbon atom which lies anywhere along the line between the substitution site and the interstitial tetrahedral site (Song and Watkins, 1990). DLTS studies of the donor (E_v + 0.28 eV) and acceptor levels (E_c – 0.12 eV) were identified using similarities in the formation and annealing behaviours seen in EPR studies (Lee *et al*., 1977).

EPR studies by Song and Watkins (1990), identified the negative charged state of the C_i-Si_s pair to correspond to the Si-L6 centre. The structural information obtained was in agreement with the symmetry used to describe the positive charged state of the interstitial carbon. Zheng *et al*. (1994) later obtained the structural information of the interstitial carbon in its neutral state from stress effects on infrared (IR) bands which again was in agreement with the symmetry used to describe the positive state.

Photoluminescence (PL) studies by Woolley *et al*. (1986) assigned the 0.856 eV line to the C_i-Si_s complex. This conclusion was further re-enforced by Thonke *et al*. (1987) obtaining the hole binding energy of 0.25 eV in perfect agreement with DLTS measurements.

The annealing of the C_i has shown itself to be of a complicated nature depending on multiple material characteristics, fabrication techniques and the charge state of the atom. While mobile at room temperature, the C_i tends to form complexes with dominant traps present in the substrate. The rate of complex formation has previously been reported to be dependent on the concentration of other traps present. Shinoda and Ohta (1992) measured the annealing rate constant of C_i to increase as a function of oxygen concentration. This can be described as C_i atoms having less distance to travel before encountering a trapping site.

Further studies have shown the migration energy to be dependent on the charge state of the atom. In n-type material it was found that the C_i was in a positive state while under a reverse bias in the depletion region and the majority placed under a neutral state while the system was unbiased. While under a neutral state, the migration energy was found to decrease, however, the annealing rate was independent of the value of the reverse bias applied to the system (Lastovskii *et al*., 2017).

© University of Pretoria

Table 3.1 Summary of previous investigations of the C_i defect's properties.

Property	Value	Reference
Emission activation energy level / Trap level	C_i^- : $E_c - 0.12$ eV C_i^+ : $E_v + 0.28$ eV	(Shinoda and Ohta, 1992) (Makarenko *et al.*, 2009) (Lastovskii *et al.*, 2017)
DLTS peak identification	C_i^- : E0 C_i^+ : H1	(Makarenko *et al.*, 2009)
Apparent capture cross-section	C_i^- : 5.9×10^{-15} cm^2 C_i^+ : 5.6×10^{-15} cm^2	(Moll, 1999) (Khirunenko *et al.*, 2005)
Annealing temperature range (Unbiased n- type)	260 – 300 K 280 – 330 K	(Khirunenko *et al.*, 2005) (Lastovskii *et al.*, 2017)
Annealing temperature range (Reverse bias n- type)	280 – 330 K	(Lastovskii *et al.*, 2017)
Annealing activation energy	0.72 → 0.78 eV	(Makarenko *et al.*, 2007) (Makarenko *et al.*, 2009)
Migration energy	0.88 ± 0.02 eV (Charged) 0.73 − 0.74 eV (Neutral) 0.72 eV (Neutral)	(Lastovskii *et al.*, 2017) (Makarenko *et al.*, 2007)
EPR signal	C_i^+ : G12 C_i^- : L6	(Watkins and Brower, 1976) (Song and Watkins, 1990)
Point-group symmetry	C_i^- : D_{2v}	(Watkins and Brower, 1976) (Song and Watkins, 1990)
PL spectroscopy	0.856 eV	(Woolley *et al.*, 1986)
IR spectroscopy	C_i^+ : (77 K) 922 cm^{-1} C_i^+ : (77 K) 932 cm^{-1}	(Chappell and Newman, 1987)

3.1.2 Carbon-interstitial oxygen-interstitial (C_iO_i) complex

Interstitial oxygen (O_i) is another common unintended impurity introduced during the growth phase of Si substrates. C_i species (see Section 3.1.1) which are highly mobile at room temperature in n-type Si are introduced into the lattice after exposing the substrate to high energy particles. These mobile species migrate to eventually bond with the O_i impurities to form the interstitial-carbon interstitial-oxygen (C_iO_i) complexes.

The introduction of the C_iO_i has been observed to be more complex in p-type material than in n-type material. Due to the slow migration rates of the self-interstitial at room temperature, the C_iO_i complexes are initially seen to form at a lower rate in p-type material compared to that observed in n-type material. However, the self-interstitial migration rate can be stimulated by means of injection. Furthermore, in n-type material, the C_iO_i was found to have only one configuration, while in p-type material, it is observed to have two configurations namely $C_iO_i^*$ and C_iO_i. These two configurations are formed in equal proportions, but the metastable $C_iO_i^*$ complex transforms into the C_iO_i complex during annealing just above room temperatures. The reaction can be summarized as follows:

$$C_i + O_i \rightarrow C_iO_i \tag{32}$$

$$C_i + O_i \rightarrow C_iO_i^* \xrightarrow{RT} C_iO_i \tag{33}$$

© University of Pretoria

It is believed that the configuration of the C_iO_i that forms depends on the direction from which the C_i diffuses towards the O_i. Either directly towards the global minimum of the potential to form the stable complex or towards a local minimum to form a metastable complex (Makarenko *et al*., 2009).

IR spectroscopy investigations by Newman and Bean (1971) observed the concentration of carbon interstitials reducing at room temperature at the same time absorption bands 865 and 1116 cm^{-1} appeared. These were labelled C(3) and attributed to carbon and oxygen. Zero-phonon investigations (C-line 0.7894 eV) in photoluminescence (PL) spectra showed the associated defect has a C_{1h} symmetry while containing both carbon and oxygen (Thonke *et al*., 1985). Investigations later by Davies *et al*. (1986) showed close correlation between the IR C(3) centre and the PL C-line, while also demonstrating no vacancies to be involved, assigning them to the C_iO_i complex. Further investigations by Trombetta and Watkins (1987) showed the EPR centre Si-G15 and the PL C-line to arise from the same defect. The EPR signal was identified to arise from a positive state due to a C_i-Si_s pair near an interstitial oxygen atom (Lee, Corbett and Brower, 1977). Mukashev *et al*. (2000) further suggested that the formation of the metastable C_iO_i* was similar but with the oxygen next to the C_i-Si_s pair.

DLTS and electrical measurements have shown strong complimentary information. Based on correlation with the EPR Si-G15 centre, the energy of the donor level was reported to be $E_v + 0.38$ eV (Mooney *et al*., 1977). Asom *et al*. (1987) later attributed the value $E_v + 0.36$ eV because of correlation to the PL C-line to the C_iO_i pair. These two closely spaced energy levels were both attributed to carbon–oxygen complexes but with different atomic arrangements of the C_iO_i complex (Londos, 1990). Shinoda and Ohta (1992) found an acceptor level in electron-irradiation studies with an energy level of E_c–0.06 eV. The combination of annealing (Svensson *et al*., 1986) and formation kinetics gave strong evidence for this acceptor to be a metastable precursor of the Si-G15 EPR centre.

Table 3.2: Experimental properties of the C_iO_i complex obtained from literature.

Electrical Property	Value	Reference
Emission activation energy level / Trap level	$C_iO_i^-$: $E_c - 0.06$ eV $C_iO_i^+$: $E_v + 0.36$ eV $C_iO_i^{+*}$: $E_v + 0.34$ eV	(Shinoda and Ohta, 1992) (Makarenko *et al*., 2009) (Khirunenko *et al*., 2005)
DLTS peak identification	$C_iO_i^+$: H2	(Makarenko *et al*., 2009)
Apparent capture cross-section	$C_iO_i^{+*}$: 4.2×10^{-15} cm^2 $C_iO_i^+$: 3.5×10^{-15} cm^2	(Khirunenko *et al*., 2005)
Annealing temperature 1/e	15 min: ~325 K	(Khirunenko *et al*., 2005)
Annealing activation energy	1.99 eV	(Svensson *et al*., 1986)
Formation activation energy	$C_iO_i^+$: 1.0→1.05 eV	(Abdullin *et al*., 1992) (Makarenko *et al*., 2009)
Formation frequency factor	$C_iO_i^+$: 6→9.5 $\times 10^{12}$ s^{-1}	(Abdullin *et al*., 1992) (Makarenko *et al*., 2009)
Annealing frequency factor	RT : 3×10^{-5} s^{-1}	(Shinoda and Ohta, 1992)
EPR signal	$C_iO_i^+$: G15 center	(Shinoda and Ohta, 1992)
Point-group symmetry	C_{1h}	(Thonke *et al*., 1985)
PL spectroscopy	$C_iO_i^{+*}$: C-line 0.7894 eV	(Thonke *et al*., 1985)
IR spectroscopy	$C_iO_i^+$: (10K) C(3) 865.2 and 115.5 cm^{-1}	(Newman and Bean,1971)

© University of Pretoria

3.1.3 Carbon-interstitial carbon-substitutional (C_iC_s)

In sufficiently high concentrations, C_s atoms are natural reaction partners for C_i atoms. Brower (1974) reported the first successful identification of the carbon pair. The EPR signal Si–G11 centre was attributed to the positive charge state of the C_iC_s pair. Optical detection of magnetic resonance (ODMR) studies done by Lee *et al*. in 1982 led to the most widely studied zero-phonon 0.969 eV G-line. It was identified to arise from two C_s atoms with a Si_i in between. Davis *et al*. (1983) re-examined the vibronic sidebands, which indeed also gave indications of two carbon atoms. Unlike the ODMT studies by Lee *et al.* (1982), it was suggested the carbon atoms occupy inequivalent crystal sites.

Originally complementary DLTS investigations attributed the bi-stable electrical properties of the C_iC_s to the O_iV pair, which was later rectified (Jellison, 1982). Song *et al*. (1986) combined the results from a multitude of different measurements (IR, ODMR, EPR, DLTS) to give a full analysis of the electrical properties of the defect. It was found to exist in two possible configurations due to its bi-stability. The EPR centres Si–G11 and Si–G17 correspond to the positive charge state of the C_iC_s pair. Similarly, the corresponding DLTS donor and accepter levels were identified as $E_v + 0.09$ and E_c–0.17 eV respectively. They all show a common stable configuration consisting of a C_s atom directly adjacent to a C_iSi_s pair. The neutral state gives rise to the EPR signal Si–L7 centre, with the configuration consisting of two C_s atoms with a Si_i in-between. The corresponding DLTS measurements found an acceptor level at E_c–0.11 eV with no signs of a donor level.

It was first reported by Jellison (1982) that the transient associated with the energy level E_c–0.17 eV can be converted to a faster transient corresponding with an energy level at E_c–0.11 eV under special pulsing conditions. However, not all of the traps associated with this energy level could be converted, which led to the conclusion that this was due to the contribution of two traps. This was later supported with annealing profiles with the stable component attributed to the O_iV pair which anneals out at higher temperatures. The transition from the positive state to the neutral state could be achieved with a special pulsing condition. For the conversion associated with the conversion from the neutral to the positive state, the pulse width had to be less than τ_p. For the conversion associated with the conversion from the positive state to the neutral state, the reverse bias time between pulses had to be greater than τ_r. These time constants are thermally active and are given by

$$\tau_p = 7.3 \times 10^{-13} e^{\frac{0.174\,eV}{kT}}\ , \tag{7}$$

$$\tau_r = 7.5 \times 10^{-13} e^{\frac{0.145\,eV}{kT}}\ . \tag{8}$$

Other methods were later developed to generate the neutral state, which include but are not limited to minority carrier injection at less than 50 K (regardless of cooling conditions) and photo excitation with Nd:YAG (1.16 eV) light. The full configurational-coordinate energy diagram measured by Song (1988) and Jellison (1982) for the bi-stable C_iC_s pair can be seen in Figure 3.1.

© University of Pretoria

Table 3.3: Experimental properties of the C_iC_s complex obtained from literature.

Electrical Property	Value	Reference
Emission activation energy level / Trap level	A: $C_iC_s^-$: $E_c - 0.17$ eV B: $C_iC_s^0 + e$: $E_c - 0.10$ eV A: $C_iC_s^+$: $E_v + 0.09$ eV B: $C_iC_s^0 + h$: $E_v - 0.05$ eV	(Jellison, 1982) (Song *et al.*, 1988)
Annealing activation energy	1.7→1.9 eV	(Davies *et al.*, 1991)
EPR signal	$C_iC_s^-$: G11 $C_iC_s^0$: L7 $C_iC_s^+$: G17	(Song, Zhan *et al.*, 1990)
PL spectroscopy	G-line 0.969 eV	(O'Donnell *et al.*, 1983)
IR spectroscopy	A: C_iC_s : (10 K) 594.6, 596.66, 722.4, 953 cm^{-1} B: C_iC_s : (10 K) 540.4, 543.3, 579.8, 640.6, 730.4, 842.4 cm^{-1}	(Lavrov *et al.*, 1999)

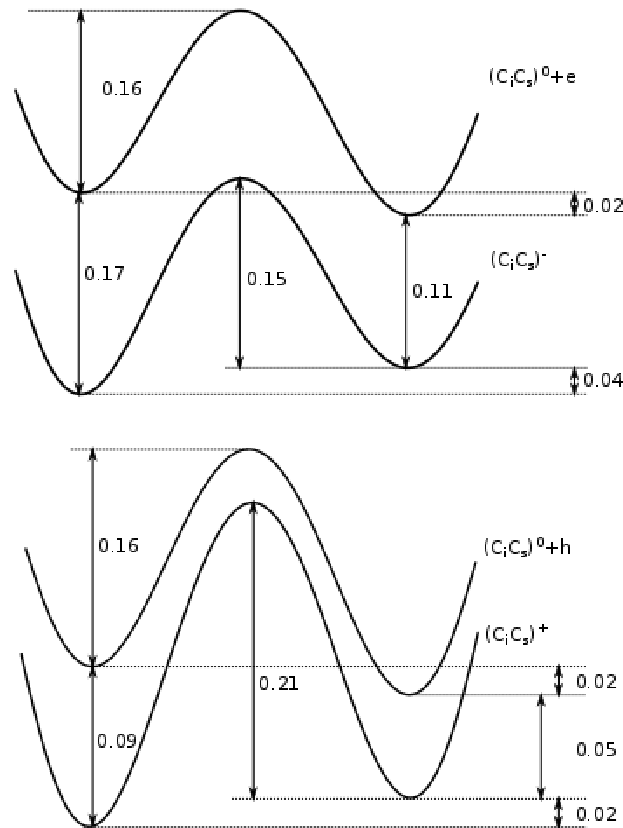

Figure 3.1 Configurational-coordinate energy diagram (in eV) for the acceptor (top) and donor (bottom) state of the C_iC_s complex. (After Song 1988.)

© University of Pretoria

3.2 Oxygen-Vacancy (O_iV)

During the growth of CZ substrates, oxygen diffuses from the silica crucible during its molten phase (Zulehner, 1983) with concentrations ranging between 10^{17} and 10^{18} cm^{-3}. Investigation of the oxygen by Bond and Kaiser (1960) showed direct evidence by means of X-ray investigations of the interstitial nature. This was further justified by IR measurements (Kaiser *et al.*, 1956) suggesting that oxygen forms a non-linear pseudo-molecule (Si-O-Si) consisting of an O_i bonded with two Si atoms (Wang *et al.*, 2014).

After electron irradiation, the primary defect observed with EPR (Si-A) was first observed by Bemski *et al.* (1959) and later labelled as Si-B1 by Watkins *et al.* (1959). The EPR centre Si-B1 was well researched (ENDOR, IR, EPR, DLTS) and showed to arise from the negative charged state. The configuration of this charged state was shown to have C_{2v} symmetry. Often referred to as a substitutional oxygen, the complex is that of O_i in the off centre position in a vacancy between two Si_s (i.e. lattice) atoms. In the neutral state it would give rise to the EPR centre Si-S1 (Brower, 1971).

DLTS studies of the acceptor level found the complex to average an energy level of $E_c - 0.16$ eV to 0.18 eV (Brotherton *et al.*, 1982). Further extensive EPR studies by Frens *et al.*(1993) assigned the VO complex the donor level $E_c - 0.76$ eV and showed it to be of amphoteric nature. Makarenko (1991) re-evaluated the experiments based on gamma-ray irradiation experimentation and concluded that the Si-A centre has an acceptor and donor level at $E_c - 0.16$ and $E_c - 0.2$ eV respectively. At 77 K the localization modes 835 and 884 cm^{-1} which shift to 830 and 877 cm^{-1} at room temperature, were assigned to the neutral and negative charge states. Further studies showed these vibrational lines correlating to the lines 1370 and 1430 cm^{-1} at 10 K (Lindström *et al.*, 1999; Murin *et al.*, 1999).

The Shockley-Read-Hall carrier lifetime was found to be determined at high levels of injection by OV complexes introduced by either low mass MeV ion implantation or particle irradiation. This lends it to the application to control the lifetime in power semiconductors (Mogro, Love, Chang and Dyer, 1986)**,** (Sawko and Bartko, 1983).

Table 3.4: Experimental properties of the O_iV complex obtained from literature.

Electrical Property	Value	Reference
Emission activation energy level / Trap level	VO^- : $E_c - 0.16$ eV VO^0 : $E_c - 0.2$ eV	(Makarenko 1991)
Annealing activation energy	1.8 eV	(Londos *et al.,* 1998)
Point-group symmetry	C_{2v}	(Brower, 1971)
IR spectroscopy	VO^- : (10 K) 1430 cm^{-1} VO^0 : (10 K) 1370 cm^{-1}	(Lindström *et al.*, 1999), (Murin *et al.*, 1999)
EPR signal	VO^- : Si-B1 VO^0 : Si-S1	(Watkins *et al.*, 1959) (Brower, 1971)

© University of Pretoria

3.3 Di-vacancy (V_2)

Corbett and Watkins (1961) were the first to identify the EPR spectra Si-G6 (single positive) and Si-G7 (single negative) centres (originally labelled Si-J and Si-C respectively) to be associated with the di-vacancy in silicon. Observations were done after 20 K *in situ* irradiation, which suggests formation does not involve annealing and that the di-vacancy is a primary defect. IR studies in correlation to EPR, associates the absorption bands at 1.8, 3.3 and 3.9 µm to the neutral, double negative and positive charge states, respectively (Cheng *et al*., 1966). High-energy particle irradiation results in the formation of vacancies. In the case of β-particle irradiation, the high energy electron collides with the nuclei of the Si_s (i.e. lattice atoms) transferring sufficient energy during collision, displacing it from its lattice position as Si_i. This Si_i then collides with the nearest neighbour atom, displacing it from its lattice position. The initial Si_i atom must retain enough energy to remain an interstitial atom, resulting in two adjacent vacancies being created.

In its undistorted state the configuration of the V_2 can be described by the D_{3d} point-group symmetry, having high-symmetry axes along the four equivalent $\langle 111 \rangle$ directions. However, degenerate and partially occupied orbitals appear in its charged states (V_2^+, V_2^0, V_2^-) allowing Jahn-Teller distortion to take place lowering the symmetry to C_{2h}. This symmetry was confirmed experimentally by EPR measurements at temperatures lower than 20 K (Wit *et al*., 1976; Watkins and Corbett, 1965).

The energy and the direction of scattering the initial Si_s received from the high energy electron can be determined by the Mott-Rutherford scattering formula (Rose, 1948). The production rate of V_2 has been observed to be substantially anisotropic, which increases with decreasing bombardment energy.

DLTS studies observed the acceptor energy levels $E_c - 0.23$ eV and $E_c - 0.42$ eV both having one to one proportional introduction rates during electron and gamma irradiation (Evwaraye and Sun, 1976). This relationship did not persist with other irradiation studies concerning protons, alpha particles (Hallén *et al*., 1990), neutrons (Tokuda, Shimizu and Usami, 1979) or even ions within the MeV range (Svensson *et al*., 1991). The donor level has been reported to be around $E_v + 0.18$ to +0.23 eV. It was found by Kuchinskii and Lomako (1987) to have introduction rates for gamma and electron irradiation which agree with those observed for the acceptor levels.

Isochronal annealing studies showed the $1/e$ point to occur at 340 °C with no annealing being observed below 280 °C. Isothermal annealing studies revealed a thermal activation energy of 1.47 eV and a frequency factor of 1.08×10^9 s^{-1} which corresponds to dissociation of the VV (Evwaraye and Sun, 1976). This was observed to be the same for both levels of the trap: V_2^- and $V_2^=$.

The true electron capture cross-sections (determined by varying the pulse length in DLTS studies) was determined for V_2^- and $V_2^=$ by Evwaraye and Sun in 1976 to be 6×10^{-15} and 1.62×10^{-16} cm^2 respectively. However, the capture rate for V_2^- is controversial as it is 4 to 5 orders of magnitude higher than expected for a highly localized and repulsive single negative charged state ($10^{-19} \rightarrow 10^{-21}$ cm^2) (Svensson *et al*., 1991).

© University of Pretoria

Table 3.5 Experimental properties of the V_2 reported in literature.

Electrical Property	Value	Reference
Emission activation energy level / Trap level	V_2^+ : E_v + 0.25 eV V_2^- : E_c – 0.23 eV $V_2^{=}$: E_c – 0.42 eV	(Svensson *et al.*, 1991)
Apparent capture cross-section	V_2^+, : 7.9 × 10^{-16} cm^2	(Khirunenko *et al.*, 2005)
True capture cross-section at T→∞	V_2^- : 6.00 × 10^{-15} cm^2 $V_2^{=}$: 1.62 × 10^{-16} cm^2	(Evwaraye and Sun, 1976)
Annealing temperature 1/e	340 °C	(Evwaraye and Sun, 1976)
Annealing activation energy	1.47 ± 0.15 eV	(Evwaraye and Sun, 1976)
Annealing pre-factor	1.08 × 10^9 s^{-1}	(Evwaraye and Sun, 1976)
EPR signal	V_2^+ : G6 V_2^- : G7	(Corbett and Watkins, 1961)
Point-group symmetry	D_{3d} Jahn-Teller distortion C_{2h}	(Wit, Sieverts and Ammerlaan, 1976)

3.4 Phosphorus-substitutional vacancy (P_sV)

Phosphorous, an intentional impurity introduced into the substrate by means of doping is by far the fastest diffusing donor impurity in Si. This decreases its importance for microelectronics, however, it still has great importance for power semiconductors. In high concentrations, phosphorous has the ability to getter detrimental impurities. In substitutional sites in Si, the atoms easily emit an electron to the conduction band. Hall-effect measurements have shown this donor level to average around E_c – 0.045 eV (Samara *et al.*, 1987; Pajot *et al.*, 1979), agreeing with the theoretical expected values 0.0443 eV (Pantelides *et al.*, 1974).

Exposing the substrate to external radiation sources which introduce vacancies results in the formation of the phosphorous-vacancy (PV) donor vacancy complex. The first EPR spectrum was reported by Watkins *et al.* (1959) labelling it Si-E. This EPR signal was later relabelled to Si-G8, however, Si-E was still used and extended for other pairs of substitutional group-V vacancy complexes. Electron-nuclear double resonance was later used to identify the complex as a vacancy adjacent to a substitutional phosphorous atom in a neutral charge state (PV^0) (Watkins *et al.*, 1964).

EPR investigations by Watkins *et al.* (1959) show the acceptor level to be E_c – 0.44 eV. DLTS measurements by Kimerling *et al.* (1975) and Chantre *et al.* (1983) estimate the acceptor level to be E_c – 0.45 eV and E_c – 0.44 eV respectively. L-DLTS showed the emission rate observed with DLTS are indeed 2 centres with similar emission rates (Evans-Freeman *et al.*, 2000).

Annealing studies have shown two annealing stages associated with the diffusion of the PV complex with the first stage occurring from 120 to 180 °C (Hirata *et al.*, 1966) and the second stage at temperatures higher than 200 °C (Hirata *et al.*, 1967). Kimerling *et al.* (1975) obtained the activation energy 0.95 eV for the neutral charged state and 1.25 eV for the negative charged state. The difference in activation energies was explained quantitatively by the double Coulomb attraction between the double negative charged vacancy and the positively charged phosphorous atom which increases the diffusion barrier.

© University of Pretoria

Table 3.6: Experimental properties of the P_sV complex obtained from literature.

Electrical Property	Value	Reference
Emission activation energy level / Trap level	E_c − 0.458±0.005 eV	(Auret *et al*., 2006)
Annealing temperature range	PV^0 : 120 → 180 °C PV^- : >200 °C	(Hirata *et al*., 1966) (Hirata *et al*., 1967)
Annealing activation energy	PV^0 : 0.95 eV PV^- : 1.25 eV	(Kimerling *et al*.,1975)
EPR signal	PV^0 : Si-E / Si-G8	Watkins *et al*. (1959)

3.5 References

Abdullin, K., Mukashev, B., Tamendarov, M. and Tashenov, T. (1992). Electronic Levels and Properties of the Selfinterstitials in Irradiated Silicon. *MRS Proceedings*, 262.

Asom, M., Benton, J., Sauer, R. and Kimerling, L. (1987). Interstitial defect reactions in silicon. *Applied Physics Letters*, 51(4), pp.256-258.

Auret, F., Peaker, A., Markevich, V., Dobaczewski, L. and Gwilliam, R. (2006). High-resolution DLTS of vacancy–donor pairs in P-, As- and Sb-doped silicon. *Physica B: Condensed Matter*, 376-377, pp.73-76.

Bemski, G. (1959). Paramagnetic Resonance in Electron Irradiated Silicon. *Journal of Applied Physics*, 30(8), pp.1195-1198.

Bond, W. and Kaiser, W. (1960). Interstitial versus substitutional oxygen in silicon. *Journal of Physics and Chemistry of Solids*, 16(1-2), pp.44-45.

Brotherton, S. and Bradley, P., 1982. Defect production and lifetime control in electron and γ-irradiated silicon. *Journal of Applied Physics*, 53(8), pp.5720-5732.

Brower, K., 1971. Structure of multiple-vacancy (oxygen) centers in irradiated silicon. *Radiation Effects*, 8(3-4), pp.213-219.

Brower, K. (1974). EPR of a Jahn-Teller distorted (111) carbon interstitialcy in irradiated silicon. *Physical Review B*, 9(6), pp.2607-2617.

Chantre, A. and Bois, D. (1985). Metastable-defect behavior in silicon: Charge-state-controlled reorientation of iron-aluminum pairs. *Physical Review B*, 31(12), pp.7979-7988.

Chantre, A., Kechouane, M. and Bois, D., 1983. Vacancy-diffusion model for quenched-in E-centers in CW laser annealed virgin silicon. *Physica B+C*, 116(1-3), pp.547-552.

© University of Pretoria

Chappell, S. and Newman, R. (1987). The selective trapping of self-interstitials by interstitial carbon impurities in electron irradiated silicon. *Semiconductor Science and Technology*, 2(10), pp.691-694.

Cheng, L.J. *et al.* (1966) '1.8-, 3.3-, and 3.9-μ bands in irradiated silicon: Correlations with the divacancy', *Physical Review*, 152(2), pp. 761–774.

Corbett, J. and Watkins, G. (1961). Silicon Divacancy and its Direct Production by Electron Irradiation. *Physical Review Letters*, 7(8), pp.314-316.

Davies, G., Kwok Tat Kun and Reade, T. (1991). Annealing kinetics of the dicarbon radiation-damage center in crystalline silicon. *Physical Review B*, 44(22), pp.12146-12157.

Davies, G., Lightowlers, E. and Carmo, M. (1983). Carbon-related vibronic bands in electron-irradiated silicon. *Journal of Physics C: Solid State Physics*, 16(28), pp.5503-5515.

Davies, G., Oates, A., Newman, R., Woolley, R., Lightowlers, E., Binns, M. and Wilkes, J. (1986). Carbon-related radiation damage centres in Czochralski silicon. *Journal of Physics C: Solid State Physics*, 19(6), pp.841-855.

Evans-Freeman, J., Peaker, A., Hawkins, I., Kan, P., Terry, J., Rubaldo, L., Ahmed, M., Watts, S. and Dobaczewski, L. (2000). High-resolution DLTS studies of vacancy-related defects in irradiated and in ion-implanted n-type silicon. *Materials Science in Semiconductor Processing*, 3(4), pp.237-241.

Evwaraye, A. and Sun, E. (1976). Electron-irradiation-induced divacancy in lightly doped silicon. *Journal of Applied Physics*, 47(9), pp.3776-3780.

Frens, A.M. *et al.* (1993) 'Observation of rapid direct charge transfer between deep defects in Silicon', *Materials Science Forum*, 143–147, pp. 1371–1374.

Hallén, A., Sundqvist, B., Paska, Z., Svensson, B., Rosling, M. and Tirén, J. (1990). Deep level transient spectroscopy analysis of fast ion tracks in silicon. *Journal of Applied Physics*, 67(3), pp.1266-1271.

Hirata, M., Hirata, M. and Saito, H. (1966). Annealing of E Center in Irradiated Silicon. *Japanese Journal of Applied Physics*, 5(3), pp.252-252.

Hirata, M., Hirata, M., Saito, H. and Crawford J.H. (1967). Annealing of lrradiated Silicon Containing Phosphorus Atoms. *J. Phys. Soc. Japan*, 22(3), p.1301.

Jellison, G. (1982). Transient capacitance studies of an electron trap at $E_c - E_T = 0.105$ eV in phosphorus-doped silicon. *Journal of Applied Physics*, 53(8), pp.5715-5719.

Kaiser, W., Keck, P. and Lange, C. (1956). Infrared Absorption and Oxygen Content in Silicon and Germanium. *Physical Review*, 101(4), pp.1264-1268.

Khirunenko, L., Pomozov, Y., Tripachko, N., Sosnin, M., Duvanskii, A., Murin, L., Lindström, J., Lastovskii, S., Makarenko, L., Markevich, V. and Peaker, A. (2005). Interstitial Carbon Related Defects in Low-Temperature Irradiated Si: FTIR and DLTS Studies. *Solid State Phenomena*, 108-109, pp.261-266.

© University of Pretoria

Kimerling, L., DeAngelis, H. and Diebold, J. (1975). On the role of defect charge state in the stability of point defects in silicon. *Solid State Communications*, 16(1), pp.171-174.

Kolbesen, B. and Mühlbauer, A. (1982). Carbon in silicon: Properties and impact on devices. *Solid-State Electronics*, 25(8), pp.759-775.

Kuchinskii, P. and Lomako, V. (1987). On the Mechanism of Primary Radiation Defect Annihilation in Si. *Physica Status Solidi (a)*, 102(2), pp.653-658.

Lastovskii, S., Gusakov, V., Markevich, V., Peaker, A., Yakushevich, H., Korshunov, F. and Murin, L. (2017). Radiation-induced interstitial carbon atom in silicon: Effect of charge state on annealing characteristics. *physica status solidi (a)*, 214(7), p.1700262.

Lavrov, E., Hoffmann, L. and Bech Nielsen, B. (1999). Local vibrational modes of the metastable dicarbon center(Cs–Ci)in silicon. *Physical Review B*, 60(11), pp.8081-8086.

Lee, K., O'Donnell, K., Weber, J., Cavenett, B. and Watkins, G. (1982). Optical Detection of Magnetic Resonance for a Deep-Level Defect in Silicon. *Physical Review Letters*, 48(1), pp.37-40.

Lee, Y., Corbett, J. and Brower, K. (1977). EPR of a carbon-oxygen-divacancy complex in irradiated silicon. *Physica Status Solidi (a)*, 41(2), pp.637-647.

Lindström, J., Murin, L., Markevich, V., Hallberg, T. and Svensson, B. (1999). Vibrational absorption from vacancy-oxygen-related complexes (VO, V2O, VO2) in irradiated silicon. *Physica B: Condensed Matter*, 273-274, pp.291-295.

Londos, C. (1990). Carbon-related radiation damage centres and processes in p-type Si. *Semiconductor Science and Technology*, 5(7), pp.645-648.

Londos, C., Sarlis, N. and Fytros, L. (1998). Infrared studies of defects formed during postirradiation anneals of Czochralski silicon. *Journal of Applied Physics*, 84(7), pp.3569-3573.

Makarenko, L., Korshunov, F., Lastovskii, S., Murin, L. and Moll, M. (2009). DLTS Studies of Carbon Related Complexes in Irradiated N- and P-Silicon. *Solid State Phenomena*, 156-158, pp.155-160.

Makarenko, L., Moll, M., Korshunov, F. and Lastovski, S. (2007). Reactions of interstitial carbon with impurities in silicon particle detectors. *Journal of Applied Physics*, 101(11), p.113537.

Markevich, V.P., Makarenko, L.F. and Murin, L.I. (1991) 'Thermal donor formation and mechanism of enhanced oxygen diffusion in Silicon', *Materials Science Forum*, 38–41, pp. 589–594.

Mogro-Compero, A., Love, R., Chang, M. and Dyer, R. (1986). Localized lifetime control in insulated-gate transistors by proton implantation. *IEEE Transactions on Electron Devices*, 33(11), pp.1667-1671.

Moll, M. (1999). *Radiation damage in silicon particle detectors*. Hamburg: DESY.

Mooney, P., Cheng, L., Süli, M., Gerson, J. and Corbett, J. (1977). Defect energy levels in boron-doped silicon irradiated with 1-MeV electrons. *Physical Review B*, 15(8), pp.3836-3843.

© University of Pretoria

Mukashev, B., Abdullin, K. and Gorelkinskii, Y. (2000). Metastable and bistable defects in silicon. *Uspekhi Fizicheskih Nauk*, 170(2), p.143.

Murin, L., Markevich, V., Hallberg, T. and Lindström, J. (1999). New Infrared Vibrational Bands Related to Interstitial and Substitutional Oxygen in Silicon. *Solid State Phenomena*, 69-70, pp.309-314.

Newman, R. and Bean, A. (1971). Irradiation damage in carbon-doped silicon irradiated at low temperatures by 2 MeV electrons. *Radiation Effects*, 8(3-4), pp.189-193.

O'Donnell, K., Lee, K. and Watkins, G. (1983). Origin of the 0.97 eV luminescence in irradiated silicon. *Physica B+C*, 116(1-3), pp.258-263.

Pajot, B., Kauppinen, J. and Anttila, R. (1979). High resolution study of the group V impurities absorption in silicon. *Solid State Communications*, 31(10), pp.759-763.

Pantelides, S. and Sah, C. (1974). Theory of localized states in semiconductors. II. The pseudo impurity theory application to shallow and deep donors in silicon. *Physical Review B*, 10(2), pp.638-658.

Rose, M. (1948). The Charge Distribution in Nuclei and the Scattering of High Energy Electrons. *Physical Review*, 73(4), pp.279-284.

Samara, G. and Barnes, C. (1987). Pressure dependence of impurity levels in semiconductors: The deep gold acceptor level and shallow donor and acceptor levels in silicon. *Physical Review B*, 35(14), pp.7575-7584.

Sawko, D. and Bartko, J. (1983). Production of Fast Switching Power Thyristors by Proton Irradiation. *IEEE Transactions on Nuclear Science*, 30(2), pp.1756-1758.

Shinoda, K. and Ohta, E. (1992). Interstitial carbon-oxygen complex in near threshold electron irradiated silicon. *Applied Physics Letters*, 61(22), pp.2691-2693.

Song, L.W., Benson, B.W. and Watkins, G.D. (1986) 'New vacancy-related defects in*n*-type silicon', *Physical Review B*, 33(2), pp. 1452–1455.

Song, L. and Watkins, G. (1990). EPR identification of the single-acceptor state of interstitial carbon in silicon. *Physical Review B*, 42(9), pp.5759-5764.

Song, L., Zhan, X., Benson, B. and Watkins, G. (1988). Bistable defect in silicon: The interstitial-carbon–substitutional-carbon pair. *Physical Review Letters*, 60(5), pp.460-463.

Song, L., Zhan, X., Benson, B. and Watkins, G. (1990). Bistable interstitial-carbon–substitutional-carbon pair in silicon. *Physical Review B*, 42(9), pp.5765-5783. Stein, H. and Vook, F. (1969).

Stein, H.J. and Vook, F.L. (1969) 'Infrared studies of oxygen and carbon associated defects in electron-irradiated silicon', *Radiation Effects*, 1(1), pp. 41–46.

Svensson, B. and Lindstköm, J. (1986). Annealing studies of the 862 cm−1 infrared band in silicon. *physica status solidi (a)*, 95(2), pp.537-542.

Svensson, B., Mohadjeri, B., Hallén, A., Svensson, J. and Corbett, J. (1991). Divacancy acceptor levels in ion-irradiated silicon. *Physical Review B*, 43(3), pp.2292-2298.

© University of Pretoria

Thonke, K., Hangleiter, A., Wagner, J. and Sauer, R. (1985). 0.79 eV (C line) defect in irradiated oxygen-rich silicon: excited state structure, internal strain and luminescence decay time. *Journal of Physics C: Solid State Physics*, 18(26), pp.L795-L801.

Thonke, K., Teschner, A. and Sauer, R. (1987). New photoluminescence defect spectra in silicon irradiated at 100 K: Observation of interstitial carbon?. *Solid State Communications*, 61(4), pp.241-244.

Tokuda, Y., Shimizu, N. and Usami, A. (1979). Studies of Neutron-Produced Defects in Silicon by Deep-Level Transient Spectroscopy. *Japanese Journal of Applied Physics*, 18(2), pp.309-315.

Trombetta, J. and Watkins, G. (1987). Identification of An Interstitial Carbon – Interstitial oxygen Complex in Silicon. *MRS Proceedings*, 104.

Vook, F.L. and Stein, H.J. (1969) ‘Relation of neutron to ion damage annealing in Si and Ge’, *Radiation Effects*, 2(1), pp. 23–30.

Wang, H., Chroneos, A., Londos, C., Sgourou, E. and Schwingenschlögl, U. (2014). Carbon related defects in irradiated silicon revisited. *Scientific Reports*, 4(1).

Watking, G.D. (1965), in: Radiation Damage in Semiconductors (Dunod, Paris) p. 97.

Watkins, G. and Brower, K. (1976). EPR Observation of the Isolated Interstitial Carbon Atom in Silicon. *Physical Review Letters*, 36(22), pp.1329-1332.

Watkins, G. and Corbett, J. (1964). Defects in Irradiated Silicon: Electron Paramagnetic Resonance and Electron-Nuclear Double Resonance of the Si-ECenter. *Physical Review*, 134(5A), pp.A1359-A1377.

Watkins, G. and Corbett, J. (1965). Defects in Irradiated Silicon: Electron Paramagnetic Resonance of the Divacancy. *Physical Review*, 138(2A), pp.A543-A555.

Watkins, G., Corbett, J. and Walker, R. (1959). Spin Resonance in Electron Irradiated Silicon. *Journal of Applied Physics*, 30(8), pp.1198-1203.

Wit, J., Sieverts, E. and Ammerlaan, C. (1976). Divacancy in silicon: Hyperfine interactions from electron-nuclear double resonance measurements. *Physical Review B*, 14(8), pp.3494-3503.

Woolley, R., Lightowlers, E., Tipping, A., Claybourn, M. and Newman, R. (1986). Electronic and Vibrational Absorption of Interstitial Carbon in Silicon. *Materials Science Forum*, 10-12, pp.929-934.

Zheng, J. F., Stavola, M. and Watkins G.D. (1944), "Structure of the Neutral Charge State of Interstitial Carbon in Silicon ," in: *The Physics of Semiconductors,* edited by D. J. Lockwood, Singapore : World Scientific, 2363-2366.

Zulehner, W. (1983). Czochralski growth of silicon. *Journal of Crystal Growth*, 65(1-3), pp.189-213.

© University of Pretoria

4 Palladium-related defects in Si

4.1 Palladium and hydrogen

Pd, the rare silver-white ductile metal, was discovered by an English chemist, William Hyde Wollaston, in 1803 (McDonald and Hunt, 1982). Compared to other metals, when in the form of a sponge or powder, it has the greatest affinity for hydrogen. At room temperature and atmospheric pressure, it is able to adsorb up to 900 times its own volume forming palladium hydride. This absorption process is reversible, which led to the investigation of its use in hydrogen storage.

The metal gets attacked more readily by oxidizing agents compared to other similar metals (e.g. Pt). This allows it to dissolve in nitric acid or to be attacked by fluorine at red hot temperatures. At dull red hot temperatures, Pd acquires a violet oxide film while exposed to air while Pt does not. Furthermore, while heated, hydrogen and deuterium are able to diffuse through Pd.

Due to the material's strong capability to combine with H, it is extensively used as a catalyst for hydrogenation and dehydrogenation. Other uses include jewellery, catalytic convertors for harmful automobile gases and the use as electrical contacts in connectors. More than half of the world's supply of Pd and its congener Pt is used for catalytic converters converting approximately 90% of harmful automobile gases.

4.1.1 Pure palladium

Pd can be found in placer deposits as a free metal alloyed with gold and other platinum-group metals (Samson, Linnen and Martin, 2005). Pure Pd does not naturally occur on earth, however, it is prepared via a series of reactions based on the mine and nature of the ore.

The common method uses converter matte (crude, non-ferrous sulphide), which is crushed into small three-inch sized pieces, which is sent off to the smelting operations. The first step of this stage is blast furnace treatment, separating practically all the nickel matte containing only platinum group metals and the nickel matte containing small traces of copper. The nickel matte containing copper is separated, refined and finally cast into copper anode moulds for the electro-refinery. The nickel mattes containing the precious metals go through a grinding, oxidization and smelting process, before being cast into anodes for the electro-refining operations (Gouldsmith, Wilson, 1963).

The copper anodes are dissolved electrolytically with the use of copper sulphuric acid as an electrolyte. This produces pure copper cathodes and an anode slime which may contain small quantities of platinum group metals or gold. Similarly, the nickel anodes are dissolved electrolytically in a solution of nickel sulphate containing boric acid as a buffer. This results in a pure nickel cathode and a slime anode. The quantity of slime produced by the nickel anodes is far greater than that produced by the copper anodes (Gouldsmith, Wilson, 1963).

The slime is now subjected to chemical operations where it is completely chemically processed. First an enriched slime is produced by subjecting the slime to roasting and leaching attacks. This removes the last copper, iron, nickel and sulphur. The enriched slime contains approximately 65% of the platinum group metals and gold. The next treatment uses aqua-regia to separate the gold, platinum and palladium from the more insoluble metals ruthenium, rhodium, osmium and iridium. This solution is then reduced by adding ammonium chloroplatinate to remove the gold. Amonium chloride is then added during the filtration which precipitates impure ammonium chloroplatinate

© University of Pretoria

which is then calcined to produce a crude platinum sponge. This crude sponge is then re-disolved and re-precipitated as a pure ammonium chloroplatinate before being calcined again to produce a pure platinum sponge. The remaining filtrate from the ammonium chloroplatinate is then oxidized. An excess of ammonium chloride is added to precipitate the palladium as a crude ammonium salt. This is then re-dissolved in ammonia to form tetrammino palladium chloride which on acidification precipitates palladium diammino dichloride. This salt is then calcined to a pure palladium sponge (Gouldsmith, Wilson, 1963).

Brazlian Mint, uses the following steps: leeching with sulphuric acid, leeching with nitric acid, removal of impurities, yellow salt precipitation, yellow salt reduction and finally smelting of the Pd powder. This method proved purity greater than 99.9 % when produced at an industrial scale. (Sobral and Granato, 1992).

The crystal structure of pure Pd is the face-centred cubic (FCC) lattice. The distance between two corner lattice points within a single cell is 389.07 pm with the face-centre atom and the corner lattice point a distance 275.1 pm apart (Arblaster, 2012).

4.1.2 Hydrogen adsorption at metal surfaces

For many decades, hydrogen in metals has attracted the interest of many scientists. One of the most interesting properties related to the small size of hydrogen is the interstitial diffusion accompanied by quantum tunneling transport. This results in a remarkable high mobility of H in the material with thermodynamic equilibrium being reached in comparable short times at room temperature. (Oates and Flanagan, 1981).

Hydrogen allows for dense packing in metal hosts with the hydrogen density in metal hydrides being larger than liquid hydrogen. This packing is often accompanied by large negative heat of solution for hydrogen (Latroche, 2004). This restores research interest in using metal hydrides as potential energy storage materials (Züttel *et al*., 2004).

When exposing the surface of pure Pd to H_2 molecules, the molecules split and are transferred into the crystal lattice via surface adsorption, namely a combination of chemi- and physisorption (Zangwill, 2001). Physisorption is responsible for the adsorption of hydrogen via van der Waals forces, while chemical bonds between the metal and adsorbate are implied by chemisorption. The latter is responsible for subsequent uptake of hydrogen in metals (Schlapbach, 1992).

Chemisorption and dissociation are responsible for the activation energy barrier the hydrogen molecule has to overcome. Figure 4.1 illustrates the potential energy curve of hydrogen in the vicinity of a metal surface with the curves derived using Lennard-Jones potentials. On the left side of the graph (Gas), the potential energy of the gas phase of hydrogen and the metal (H_2 + M) is set to zero. In the middle (Interface) the interaction between the metal-surface and the hydrogen is visible). To the right (Metal), the potential energies of the hydrogen dissolved into the metal are plotted. When the hydrogen atoms are far from the metals surface, the potentials between the hydrogen molecule and that of two hydrogen atoms are separated by the energy required for dissociation. The van der Waals force leading to the physisorbed state is the first attractive interaction of the hydrogen molecule. When placed closer to the surface, the molecule has to overcome the activation energy barrier for dissociation and the formation of the hydrogen-metal bond. When the hydrogen on the surface of the metal shares an electron with the metal, they are in a chemisorbed state. The chemisorbed hydrogen atom can jump in the surface layer and diffuse into the interstitial sites of the host metal (Züttel *et al.*, 2010).

© University of Pretoria

With regards to the gas phase, dissolution of hydrogen in the metal can lower (exothermic reaction) or increase (endothermic reaction) the potential energy of the system. When the systems potential energy in the metal is lower than the potential energy of the hydrogen gas molecule and the metal, hydrogen absorption will occur, resulting in an exothermal reaction (Züttel *et al.*, 2010).

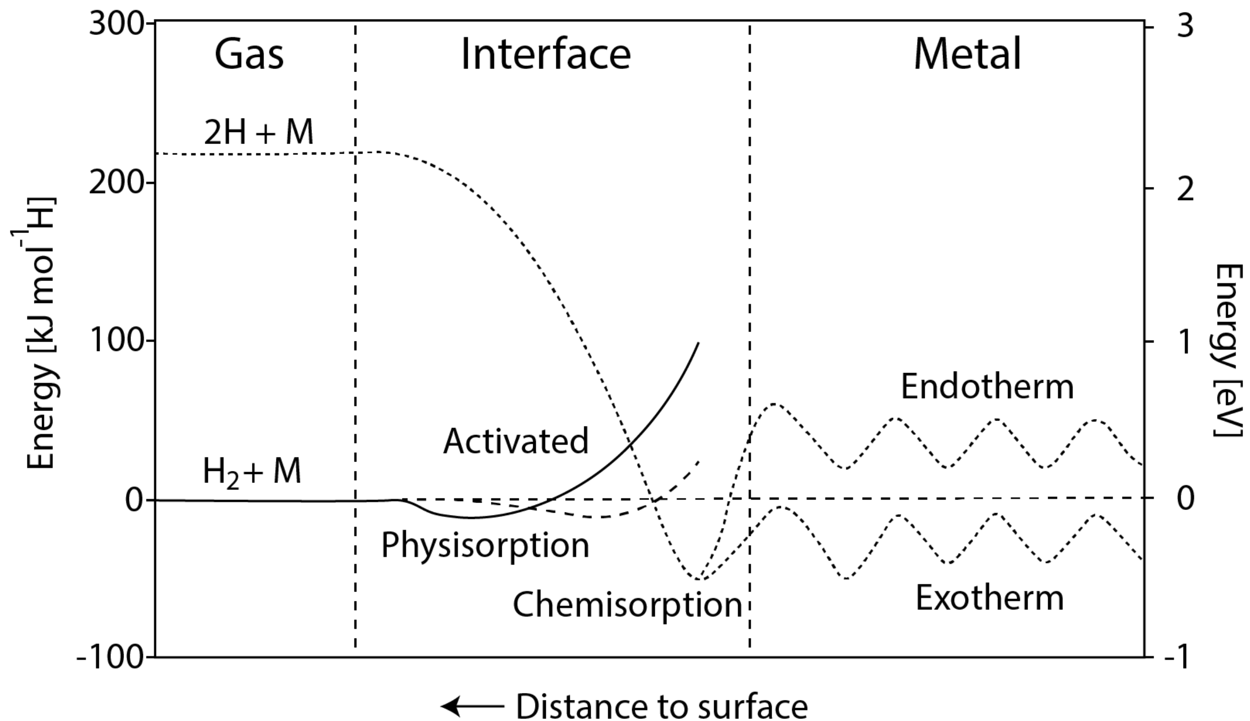

Figure 4.1 Potential energy of hydrogen approaching a metal surface based off the Lennard-Jones potential (Kirchheim and Pundt, 2014) .

When the surface of pure Pd is exposed to H_2 molecules, the two atoms separate and each adsorbs into an interstitial site. During the absorption of hydrogen, expansion of the crystal lattice has been observed. This has shown an increase of as much as 5% in the lattice coefficient (Manchester, San-Martin and Pitre, 1994).

Conrad *et al*. (1974) demonstrated that hydrogen adsorbs into Pd as an atom for Pd (110) and (111) surfaces with Behm *et al*. (1980) demonstrating this for Pd (100) surfaces. The hydrogen atoms bond to different positions in the lattice depending on the surface reconstruction and temperature. Therefore, different surface coverages exists for different surface faces (Christmann, 1988).

The number of hydrogen atoms per Pd lattice atom gives the local adsorbate hydrogen concentration (Θ). The surface phases are plotted in the surface phase diagrams (see, Foiles and Daw, 1985) where the concentration axis of conventional bulk phase diagrams are replaced with surface coverage Θ. The equilibrium position of surface metal atoms can differ from the lattice periodicity given by the bulk (Schlapbach, 1992).

Hydrogen adsorbates can induce reconstruction by changing the relaxation of metal surface atoms. At low temperatures, hydrogen will have an extraordinary high coverage of $\Theta = 1.5$ H/Pd forming a (1×2)H phase on Pd(110) (Rieder, Baumberger and Stocker, 1983). At higher temperatures, approximately 0.5 H/Pd is released transforming the surface into the (2×1)H phase. This phase is

© University of Pretoria

maintained at room temperature being quite stable with about Θ ≈ 1.5 H/Pd for Pd(100) and Pd(111) surfaces (Dong *et al*., 1998; Okuyama *et al*., 1998).

At a constant pressure, the absorbed quantity of H decreases as a function of increased temperature. The electrical conductivity and the magnetic susceptibility was found to decrease with increased H absorption. The shape of the pressure-concentration isothermal diagram suggests the existence of hydrides below 300°C. While below this temperature, the isotherm exhibits a horizontal pressure-invariant portion, suggesting the α and β phase hydrides to coexist (Khanuja *et al*., 2009).

Hydrogen absorption was suggested to form stoichiometric compounds Pd_2H. However, it is now accepted that the composition of the hydride phase varies with temperature with non-stoichiometric ratio of Pd to H atoms in both α and β phases of hydrides (Kawae *et al*., 2020).

Due to the small size of hydrogen atoms, they are absorbed onto interstitial sites of the metal lattice. For the simple lattice structure FCC, they commonly occupy sites with tetrahedral (T-site) and octahedral (O-site) symmetry, as seen in Figure 4.2.

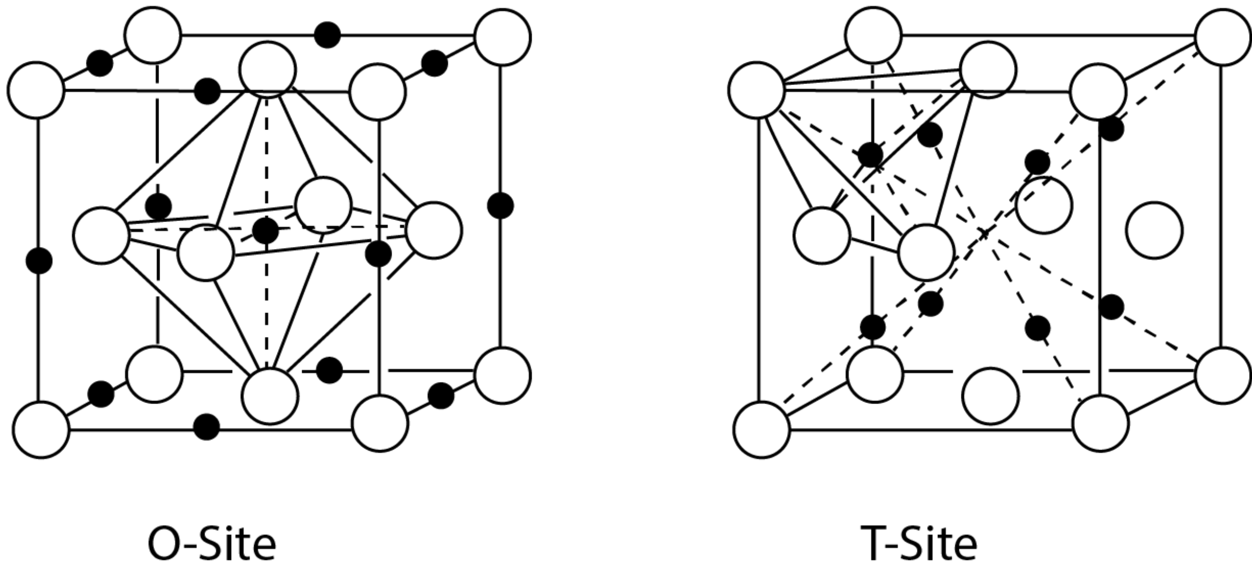

Figure 4.2 Interstitial octahedral and tetrahedral sites within FCC crystal lattice.

The total energy of the system raises by the strain energy contributed by the distortion of the lattice due to the occupation of an interstitial site. Thus the size of the interstitial site plays an important role for hydrogen occupation. To simplify the calculations, one can assume ball-like atoms which gives the relation between the lattice interstitial site and the hydrogen atom as r_i/r_h. The lattice structure relations for FCC is 0.414 (O-site) and 0.255 (T-site). Thus, for FCC lattices, the O-sites are predominantly filled (Fukai, 2005).

Sieverts (1929) studied many gases dissolving into metals and discovered Sievers' law. That is, for an environment containing low concentrations of hydrogen, the concentration of hydrogen (C_H)

within defect-free metals, has a square root relationship with the gas pressure, $C_H \sim \sqrt{P_{H_2}}$.

© University of Pretoria

4.1.3 Removal of hydrogen from palladium-hydrogen

Differential thermal analysis performed on hydrogen-containing palladium in a nitrogen environment revealed two dominant peaks. An endothermic peak with a maximum observed around 175 °C corresponding to the desorption of hydrogen and an exothermic peak observed around 280 °C which was attributed to the relaxation of the extended hydrogen-free lattice to its normal lattice spacing. Ancillary evidence was later presented suggesting hydrogen may be removed from palladium without exhibiting relaxation of the lattice (Gibb, MacMillan and Roy, 1966; Artman and Flanagan, 1972).

Some researchers did not support this idea. The desorption investigations were later revisited and accompanied with desorption of PdAg alloys, both of which showed no evidence of the exothermic peak. Desorption of hydrogen for $PdH_{0.65}$ was done within a helium environment to avoid the hydrogen-oxygen reaction. The desorption commenced at 150 °C with the maximum occurring at approximately 265 °C. Similarly, for $PdH_{0.81}$ and $PdH_{0.92}$ the endothermic maximums were measured around 245 °C and 205 °C (Artman and Flanagan, 1972).

4.2 Noble metal diffusion in Si

In semiconductor technology, the carrier lifetime can be controlled through the diffusion of noble metals (Au, Pd and Pt) which introduces recombination centres in the band gap (So *et al.*, 1977). Proton, helium and electron radiation offer better defect localization, reproducibility, "off-line" application and several degrees of freedom for profiling. However, radiation defects have low annealing temperatures (approximately 350 °C) and high concentrations cause parasitic doping and high device leakage, making them un-ideal recombination centres. In contrast, Pd and Pt in substitutional positions within the Si lattice are ideal recombination centres. However, it is difficult to introduce them with exact spatial profiles. Using a combination of both approaches, it is possible to use radiation damage to guide in-diffusion of noble metals to obtain arbitrary profiles of ideal recombination centres (Vicente *et al.*, 1993).

4.2.1 Palladium silicide

A considerable number of studies were done on the electrical properties of different silicide-Si interfaces for use as contacts in semiconductor devices. These studies are important for understanding the basics of Schottky barrier formation. Silicides are produced by evaporating metals onto a single crystal Si substrate followed by heat treatment. They are widely used for Schottky-barrier diodes and ohmic contacts in semiconductor devices. One of the most important features which distinguishes silicide interfaces from other metal-semiconductor interfaces is the strong chemical reactivity. Silicide formation alters the stoichiometry of the interface as well as the atomic structure and chemical bonding. This gives rise to an interface with electrical properties distinguishably different to non-interacting metal-semiconductor interfaces.

Ultraviolet photoemission and Auger spectroscopy studies showed the formation of Pd_2Si-Si formation on the interface of atomically cleaned Si. This silicide formation occurs at temperatures below 300 °C and is stable up to 700 °C. The resistivity and barrier heights have been measured for both *n*- and *p*-type materials for different doping concentrations. Pd_2Si formation on <111> orientated Si substrates showed epitaxial growth, whereas with <100> orientated Si, the growth was polycrystalline. The crystal structure of Pd_2Si was found to be hexagonal with the c-axis perpendicular to the substrate.

© University of Pretoria

4.2.2 Palladium in silicon

Pd, Au, Pt, and other noble metals have been investigated over the years due to their properties of being recombination centres. Diffusion of these metals within p-n junctions allows for the control of the minority carrier lifetime. This leads to an increase in leakage current caused by the generation of charge within the depletion region. Similar properties were obtained between Pd and Pt, but smaller compared to those obtained with Au (Vicente *et al.*, 1993).

Both Pd and Pt behave similarly in Si being able to occupy either substitutional or interstitial sites with the latter configuration making up a small fraction of the solutes. It was found by Azimov *et al.* (1973) that the concentration of electrically active palladium would strongly decrease as a consequence of heat treatment.

4.2.3 Diffusion of metals

Before delving into the lifetime control and technological properties, a better understanding of the diffusion process of palladium is required. Pd follows two mechanisms for interchanging from the interstitial state to the substitutional state. The Frank-Turnbull (dissociative) mechanism assumes the interstitial impurity (X_i) recombines with the lattice vacancy (V) to form the substitutional impurity (X_s). The kick-out mechanism assumes an interstitial impurity displaces a Si_s atom into a self-interstitial (I) position then occupying the substitutional site (Huntley and Willoughby, 1970).

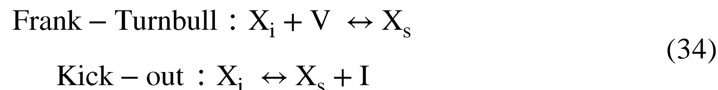

$$\begin{gathered}\text{Frank} - \text{Turnbull}: X_i + V \leftrightarrow X_s \\ \text{Kick} - \text{out}: X_i \leftrightarrow X_s + I\end{gathered} \tag{34}$$

The occurrence of these two reactions is affected by the number of lattice defects present in the crystal, thus, Pd can be guided by irradiation.

There are a few distinct differences between the two mechanics during diffusion. With the kick-out mechanism, the concentration of substitutional impurity in the middle of the wafer increases according to the square root of in-diffusion time. With dissociative mechanism, the concentration increases according to an exponential in-diffusion time.

On supersaturated wafers, during the annealing process, the concentration due to the kick-out mechanism follows a first order approximation, annealing linearly with annealing time. However, the dissociative mechanism follows an exponential approximation (Vicente *et al.*, 1993).

Investigations regarding the diffusion of Pd at high temperatures showed that the Pd defects in Si interact predominantly with self-interstitials. At low temperatures, however, they predominantly interact with vacancies.

4.3 Pd and H related defects in Si

As with radiation-induced defects discussed in Chapter 3, other impurities such as noble metals or gases can be introduced into Si crystal wafers producing electrically active defects. This section will mainly focus on the introduction of hydrogen and Pd related electrically active complexes.

© University of Pretoria

4.3.1 Silicon hydride

During fabrication of solar cell devices, impurities are often deliberately introduced into the crystal. Due to the unique possibility of depositing the antireflection coating with the surface and bulk passivation in a single processing step, silicon nitride layers containing hydrogen have become popular in the industrial solar cell processes. During deposition of the front-facing silicon nitride anti-reflection layer, large quantities of fast-diffusing atomic hydrogen are introduced into the Si (Duerinckx and Szlufcik, 2002). Important benefits include reduced surface recombination, however, the side effects and the underlying mechanism of hydrogen injection is still not well understood.

In Si, the isolated H is a bi-stable species with negative-U ordered donor and acceptor levels. The positive (H^+) and neutral (H^0) charged states both have a donor level of $E_c - 0.17$ eV. H in its positive state is most stable at the site of highest electron density, i.e. at the bond-centre site (H_{BC}^+). In its neutral state (H_{BC}^0) the donor level is most stable in the bond-center site serving as the direct transition between H_{BC}^0 and $H_{BC}^+ + e^-$ states, resulting in a free electron in the conduction band. However, in the negative charge state, H^- has an acceptor level at approximately $E_c - 0.5$ eV and avoids high electron density regions due to Coulomb repulsion. The H ion prefers to be located at a tetrahedral site (H_T^-) while in this state. There is an indirect transition involving considerable lattice relaxation energy for the acceptor which is the difference between the energy levels H_T^- and H_{BC}^0 (Andersen *et al*., 2002)

4.3.2 Pd related energy levels

Diffusion of Pd in Si plays an important role in reducing carrier lifetime without simultaneously increasing the leakage current. Pd has a significant advantage over Au or Pt, in the sense that process control can be achieved with relative ease given the lifetime values (So *et al.*, 1978). At the same time, Pd-related defect centres can also function as lifetime carrier killers making it relevant for use in fast integrated circuitry (Gill *et al.,* 1993).

Studies related to Pd defects in Si can be traced back as far as 1962 by Woodbury and Ludwig (1962) measuring an acceptor level of $E_v + 0.34$ eV using EPR. A few years later, the activation energy levels $E_c - 0.18$ eV, $E_v + 0.34$ eV were measured by Azimov *et al.* (1973) using Hall effect measurements. Similar energy levels ($E_c - 0.22$ eV, $E_v + 0.30$ eV) were obtained by Pals (1974) using the constant capacitance technique. Further investigations led by So and Ghandhi (1977) showed the formation of two independent Pd centres which were labelled Pd_I and Pd_{II}. The Pd_I centre is similar to the previously discussed centres which showed an accepter level $E_c - 0.22$ eV and a donor level $E_v + 0.33$ eV. The Pd_{II} centre was found to be acceptor-like with an energy level located at $E_v + 0.32$ eV. The concentration ratio (Pd_I/Pd_{II}) of these two centres varied from 40 to 5 for the diffusion temperature range of 900 – 1200 °C. Furthermore, for Pd_I the solubility varied from 4×10^{14} to 4×10^{15} cm^{-3} across the same temperature range, being less than that of Pt or Au (Kleinhenz *et al*., 1981).

Recent studies by Gill *et al.* (1993) related to Pd-doped p^+n Si diodes showed the existence of 5 deep levels related to the Pd impurity after exposure to α particle irradiation. It was found that the concentration of Pd-related traps would increase at the expense of the α particle radiation induced trap concentrations. Four acceptor levels, $E_c - 0.18$ eV, $E_c - 0.22$ eV, $E_c - 0.37$ eV and $E_c - 0.59$ eV where observed with one donor level, $E_v + 0.30$ eV. These 5 energy levels were later confirmed by Sudjadi *et al.* (1995) with deep-level transient Fourier spectroscopy (DLTFS).

© University of Pretoria

In the substitutional configuration, both atoms (Pd and Pt) show very similar electronic properties. Within the Si band gap, Pd_s has an acceptor level at $E_c - 0.22$ eV ($Pd_s^{-/0}$) and a donor level at E_v + 0.33 eV ($Pd_s^{0/+}$) (Woodbury and Ludwig, 1962). Similarly, Pt_s has an acceptor level at $E_c - 0.22$ eV ($Pt^{-/0}$) and a donor level at $E_v + 0.33$ eV ($Pt_s^{0/+}$). The distinguishing property between the two metals is the solid solubility of active Pd in Si being 20 – 50 times lower than that of Pt, with the Pd_s concentration increasing more gradually with diffusion temperature (Vicente *et al*., 1993). The energy levels were associated with substitutional sites due to their high thermal stability.

The in-diffusion and annealing was investigated theoretically and experimentally by Vicente *et al.* (1993). This was done by measuring the concentration of the electrically active centres associated with the energy levels of $E_c - 0.22$ and $E_v + 0.33$ eV. Within the temperature range of 880 – 1050 °C they found a constant distribution of Pd_s within the central zone even for relatively low diffusion times, suggesting high interstitial diffusivity of Pd. The concentration was found to depend highly on the square root of diffusion time, suggesting the main in-diffusion mechanism is the kick-out mechanism. In the super saturated samples, the annealing process at 550 °C showed an exponential decay with annealing time, similar to what was shown with the dissociation model. This can be summarized as follows: when the substitutional solubility is low for metal impurities, the generation of vacancies is high enough so that the main diffusion mechanism is normal diffusion. At temperatures of high solubility, the predominant mechanism would be the kick-out mechanism (Vicente *et al*., 1993).

During the investigation of the production and annealing of the of the Pd levels in Pd-doped p^+n Si diodes an interesting interaction between the Si-A centre (VO: $E_c - 0.20$ eV) and the Pd level at E_c – 0.18 eV. At temperatures above 100 °C the $E_c - 0.18$ eV concentration increased sharply at the expense of the Si-A centre. It was suggested that the vacancies dissociate from the Si-A centre and attach to electrically inactive Pd atoms converting them into electrically active traps associated with the Pd-vacancy complex in Si (Gill, Zafar *et al.,* 1994).

© University of Pretoria

4.4 References

Arblaster, J., (2012). *Crystallographic Properties of Palladium, Platinum Metals Review*, 56(3), pp.181-189.

Andersen, O., Peaker, A., Dobaczewski, L., Nielsen, K., Hourahine, B., Jones, R., Briddon, P. and Öberg, S., (2002). Electrical activity of carbon-hydrogen centers in Si. *Physical Review B*, 66(23).

Artman, D. and Flanagan, T., (1972). Desorption of Hydrogen from Palladium and Palladium-Silver Alloys followed by Differential Scanning Calorimetry. *Canadian Journal of Chemistry*, 50(9), pp.1321-1324.

Azimov, S., Yunusov, M., Tursunov, N. and Sultanov, N., (1973). some properties of palladium-doped silicon. *Soviet Physics: Semiconductors*, 6, p.1252.

Behm, R., Christmann, K. and Ertl, G., (1980). Adsorption of hydrogen on Pd(100). *Surface Science*, 99(2), pp.320-340.

Christmann, K., (1988). Interaction of hydrogen with solid surfaces. *Surface Science Reports*, 9(1-3), pp.1-163.

Conrad, H., Ertl, G. and Latta, E., (1974). Adsorption of hydrogen on palladium single crystal surfaces. *Surface Science*, 41(2), pp.435-446.

Dong, W. *et al.* (1998) 'Hydrogen adsorption on palladium: A comparative theoretical study of different surfaces', *Surface Science*, 411(1–2), pp. 123–136.

Duerinckx, F. and Szlufcik, J., (2002). Defect passivation of industrial multicrystalline solar cells based on PECVD silicon nitride. *Solar Energy Materials and Solar Cells*, 72(1-4), pp.231-246.

Foiles, S. and Daw, M., (1985). Summary Abstract: A theoretical study of the order–disorder transitions for hydrogen on Pd(111). *Journal of Vacuum Science & Technology A: Vacuum, Surfaces, and Films*, 3(3), pp.1565-1566.

Fukai, Y., (2005). *The Metal-Hydrogen System*. Berlin, Heidelberg: Springer-Verlag Berlin Heidelberg.

Gibb, T., MacMillan, J. and Roy, R., (1966). The Magnetic Susceptibility of Palladium Hydride. *The Journal of Physical Chemistry*, 70(9), pp.3024-3025.

Gill, A., Iqbal, M. and Zafar, N., (1993). Palladium-related deep levels in silicon. *Semiconductor Science and Technology*, 8(5), pp.675-681.

Gill, A., Zafar, N., Zafar Iqbal, M. and Baber, N., (1994). Interaction of α-radiation induced defects with Pd-related deep levels in silicon. *Journal of Applied Physics*, 75(12), pp.7737-7744.

Gouldsmith, A., Wilson, B., (1963). Extraction and Refining of the Platinum Metals: A Complex Cycle of Smelting, Electrolytic and Chemical Operations. *Johnson Matthey Technology Review*, 7(4), pp.136

© University of Pretoria

Huntley, F. and Willoughby, A., (1970). The diffusion of gold in thin silicon slices. *Solid-State Electronics*, 13(9), pp.1231-1240.

Kawae, T., Inagaki, Y., Wen, S., Hirota, S., Itou, D. and Kimura, T., (2020). Superconductivity in Palladium Hydride Systems. *Journal of the Physical Society of Japan*, 89(5), p.051004.

Khanuja, M., Mehta, B., Agar, P., Kulriya, P. and Avasthi, D., (2009). Hydrogen induced lattice expansion and crystallinity degradation in palladium nanoparticles: Effect of hydrogen concentration, pressure, and temperature. *Journal of Applied Physics*, 106(9), p.093515.

Kirchheim, R. and Pundt, A., (2014). Hydrogen in Metals. *Physical Metallurgy*, pp.2597-2705.

Kleinhenz, R., Lee, Y., Corbett, J., Sieverts, E., Muller, S. and Ammerlaan, C., (1981). EPR Observation of an Au-Fe Complex in Silicon: I. Experimental Data. *physica status solidi (b)*, 108(2), pp.363-371.

Latroche, M., (2004). Structural and thermodynamic properties of metallic hydrides used for energy storage☆. *Journal of Physics and Chemistry of Solids*, 65(2-3), pp.517-522.

Manchester, F., San-Martin, A. and Pitre, J., (1994). The H-Pd (hydrogen-palladium) System. *Journal of Phase Equilibria*, 15(1), pp.62-83.

McDonald, D. and Hunt, L., (1982). *A history of platinum and its allied metals*. London: Johnson Matthey.

Oates, W. and Flanagan, T., (1981). The solubility of hydrogen in transition metals and their alloys. *Progress in Solid State Chemistry*, 13(3), pp.193-272.

Okuyama, H., Siga, W., Takagi, N., Nishijima, M. and Aruga, T., (1998). Path and mechanism of hydrogen absorption at Pd(100). *Surface Science*, 401(3), pp.344-354.

Pals, J., (1974). Properties of Au, Pt, Pd and Rh levels in silicon measured with a constant capacitance technique. *Solid-State Electronics*, 17(11), pp.1139-1145.

Rieder, K.H., Baumberger, M. and Stocker, W. (1983) ‘Selective transition of chemisorbed hydrogen to subsurface sites on pd(110)’, *Physical Review Letters*, 51(19), pp. 1799–1802.

Samson, I., Linnen, R. and Martin, R., (2005). *Rare-element geochemistry and mineral deposits*. Ottawa: Mineralogical Association of Canada.

Schlapbach, L., (1992). *Hydrogen in Intermetallic Compunds II*. Berlin, Heidelberg: Springer Berlin Heidelberg, pp.15-85.

Sieverts, A., (1929). *Die Aufnahme von Gasen durch Meralle*. Z. Metallkd. 21

So, L. and Ghandhi, S., (1977). The energy levels of palladium in silicon. *Solid-State Electronics*, 20(2), pp.113-117.

So, L., Whiteley, J., Ghandhi, S. and Baliga, B., (1978). Lifetime control by palladium diffusion in silicon. *Microelectronics Reliability*, 18(3), pp.232-233.

Sobral, L. and Granato, M., (1992). Palladium : Extraction and refining. *Minerals Engineering*, 5(1), pp.17-25.

© University of Pretoria

Sudjadi, U., Weiss, S., Bock, A. and Kassing, R., (1995). Investigation of a Pd—Au complex in n-type silicon with DLTFS techniques. *Physica Status Solidi (a)*, 149(2), pp.649-658.

Vicente, J., Enríquez, L., Rubio, E., Bailón, L. and Barbolla, J., (1993). In-Diffusion and Annealing Kinetics of Palladium in Silicon. *Journal of The Electrochemical Society*, 140(3), pp.868-870.

Woodbury, H. and Ludwig, G., (1962). Spin Resonance of Pd and Pt in Silicon. *Physical Review*, 126(2), pp.466-470.

Zangwill, A., (2001). *Physics at surfaces*. Cambridge [u.a.]: Cambridge Univ. Press.

Züttel, A., Remhof, A., Borgschulte, A. and Friedrichs, O., (2010). Hydrogen: the future energy carrier. *Philosophical Transactions of the Royal Society A: Mathematical, Physical and Engineering Sciences*, 368(1923), pp.3329-3342.

Züttel, A., Wenger, P., Sudan, P., Mauron, P. and Orimo, S., (2004). Hydrogen density in nanostructured carbon, metals and complex materials. *Materials Science and Engineering: B*, 108(1-2), pp.9-18.

© University of Pretoria

5 Experimental Techniques

5.1 Sample preparation and measurements

In these experiments, the order in which irradiation and deposition of Schottky contacts is performed, is important. The term *post-irradiated* will be used to describe samples irradiated after deposition of the Schottky contacts, and the term *pre-irradiated* will refer to samples exposed to irradiation before deposition of the contact. Figure 5.1 shows the difference in the order of the steps involved in making both types of samples. Each sample was prepared in accordance with these two process types, with minor changes in the environment to suit each relevant experiment.

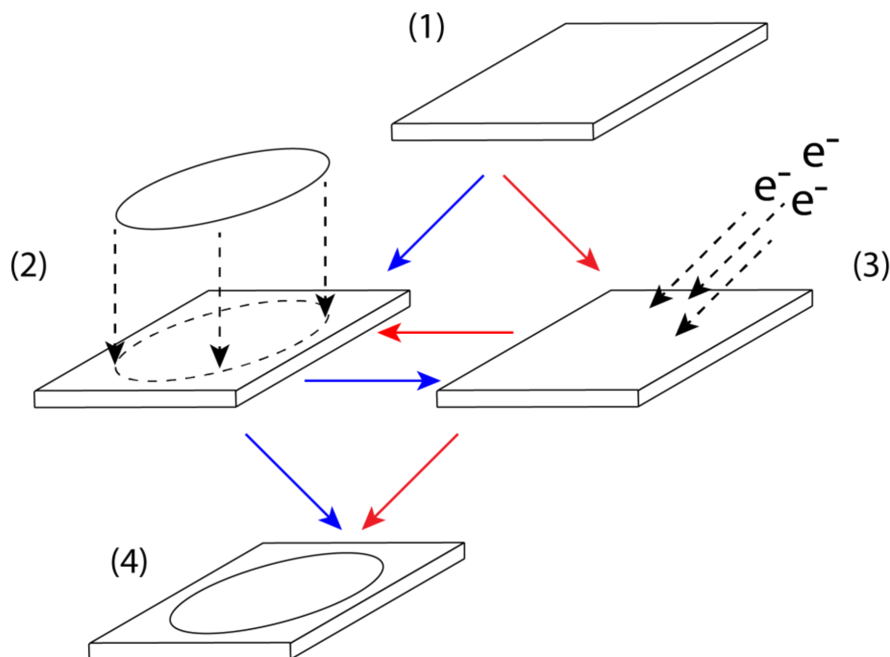

Figure 5.1 The two main sequences used for Schottky diode fabrication: post-irradiation (blue arrows) and pre-irradiation (red arrows) samples. (1) Cleaning of sample, (2) deposition of metal for fabrication of Schottky contacts, (3) exposure to electron irradiation and (4) sample ready for analysis.

© University of Pretoria

5.1.1 Cleaning process

The cleaning steps for Si samples were as follows:

- Degreasing/cleaning: Removal of general surface dust particles, grease and other organic components in trichloroethylene (TCE), isopropanol and methanol for 5 minutes each in an ultrasonic bath.
- Etching: Removal of the oxide layer using 40% HF by dipping the sample for 10 s.
- Blow dry: Samples are dried using a stream of N_2 gas and are now ready for the metallization step.

5.1.2 Schottky and ohmic contact fabrication

Schottky contacts were fabricated immediately after chemical cleaning. These contacts were deposited by evaporating metals (Au, Pd, Ni, Al etc.) onto the polished side of the Si through a metal contact mask consisting of 0.60 mm diameter circular holes. Deposition was done at a rate of 1 Å/s under a vacuum of 10^{-6} mbar. The metal layer thickness depended on the experiment and will be mentioned in each case.

A schematic of the resistive evaporation deposition system is shown in Figure 5.2. The metal to be evaporated was placed in a crucible coated with Al_2O_3. The aluminium barrier inhibits the evaporant from wetting the tungsten wire and short-circuiting the crucible. The system was sealed and placed under a high vacuum to prevent further oxidation of the substrate surface and to reduce the interaction of metal vapour with the atmosphere. The substrate was shielded from the metal evaporant while slowly increasing the current passing through the crucible. The crucible starts melting the metal and releasing metal vapour into the system. The rate of deposition is measured using the vibrating quartz crystal method. Once the desired deposition rate has been obtained, the shield is removed from the substrate and the deposition commences while monitoring the thickness of the deposition. The shield is placed between the substrate and the crucible once the desired thickness was achieved, to prevent further deposition while the crucible is cooling.

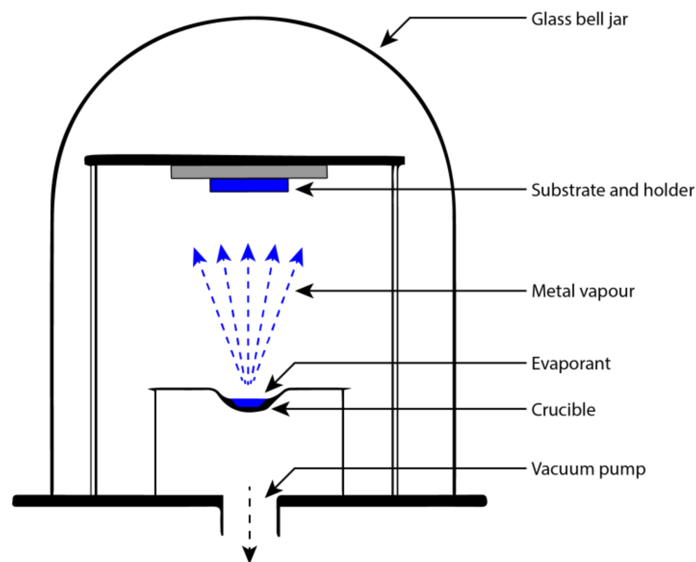

Figure 5.2 Simple side view schematic of the resistive evaporation deposition system.

© University of Pretoria

Ohmic contacts were made using liquid gallium-indium eutectic on the back of the sample. A sheet of carbon paper is placed on top of this liquid to prevent contamination to the cryostat mounting surface.

5.1.3 Electron irradiation

Electron irradiation was carried out using a ^{90}Sr radionuclide source. The half-life for the ^{90}Sr radionuclide is 28.5 years decaying to yttrium (Y-90) releasing 0.5 MeV energy, and electron and an anti-neutrino. The Y-90 has a half-life of 64.1 hours decaying into zirconium (Zr) by the emission of a 2.27 MeV energy and another electron and anti-neutrino. Over 70% of the electrons emitted from the nuclide have energies above the threshold (255 keV) required for producing defects by elastic collision within Si. The continuous energy distribution of electrons emitted by the ^{90}Sr radionuclide can be seen in Figure 5.3.

The sample was placed 1 mm away from the nuclide, below the centre of the circular ^{90}Sr source which measured 8.4 mm in diameter. The flux reaching the sample at this position can be assumed to be that leaving the surface of the source. The ^{90}Sr had an activity of 20 mCi which was used to calculate the total flux of electrons emitted by the source. Due to the much shorter life-time of the Y compared to the ^{90}Sr, each decay of ^{90}Sr leads to the emission of 2 electrons. The total dose is equal to the area under the Sr + Y curve seen in Figure 5.3. The temperature of the sample was kept constant using a Peltier cell running on a PID loop.

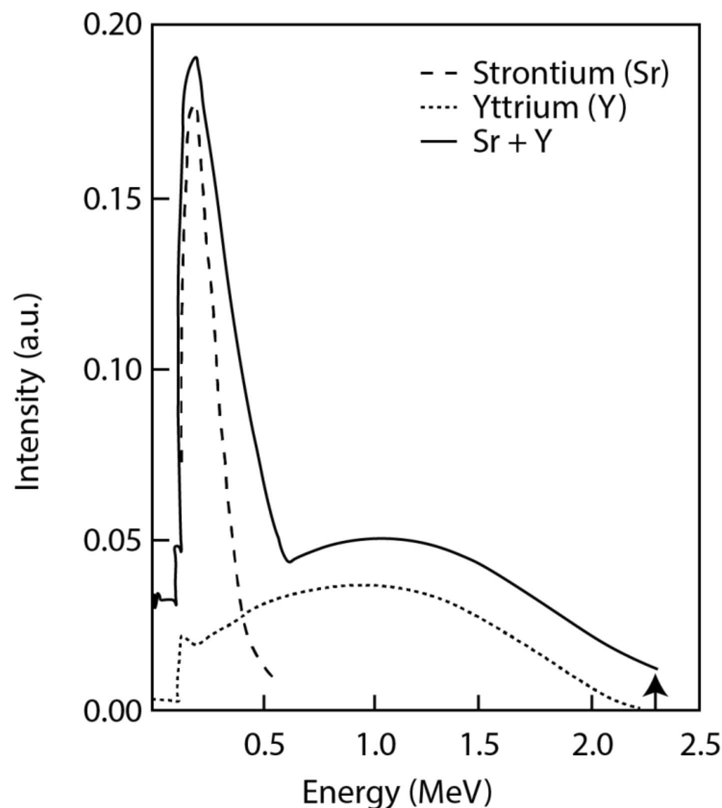

Figure 5.3 Energy distribution of electrons emitted by a ^{90}Sr radionuclide. The Sr + Y energy distribution has been displaced by an amount indicated by the arrow for clarification (Auret, Goodman, Myburg and Meyer, 1993).

© University of Pretoria

5.1.4 Annealing

Annealing of samples was done as shown in Figure 5.4. Samples were directly placed on the silver hot plate within the chamber, which was then closed and either placed under a vacuum or flushed out with argon or nitrogen gas. When gas was used, the one-way valve was opened to allow a constant flow of gas entering and leaving the chamber, but the valve was closed for vacuum annealing. Once the desired environment was achieved, the hot plate was switched on. The temperature of the hot plate was measured using a thermocouple sensor and controlled using a Lakeshore 340 temperature controller. A rate of 5 K/s was used, controlled by a PID loop to ensure it stabilizes at the desired temperature. Stabilization within 0.01 K was achieved within 10 seconds. After the sample has annealed at the stabilized temperature for a set amount of time, the hot plate is switched off and cooled down rapidly to room temperature. Once room temperature was achieved the chamber was opened to remove the sample.

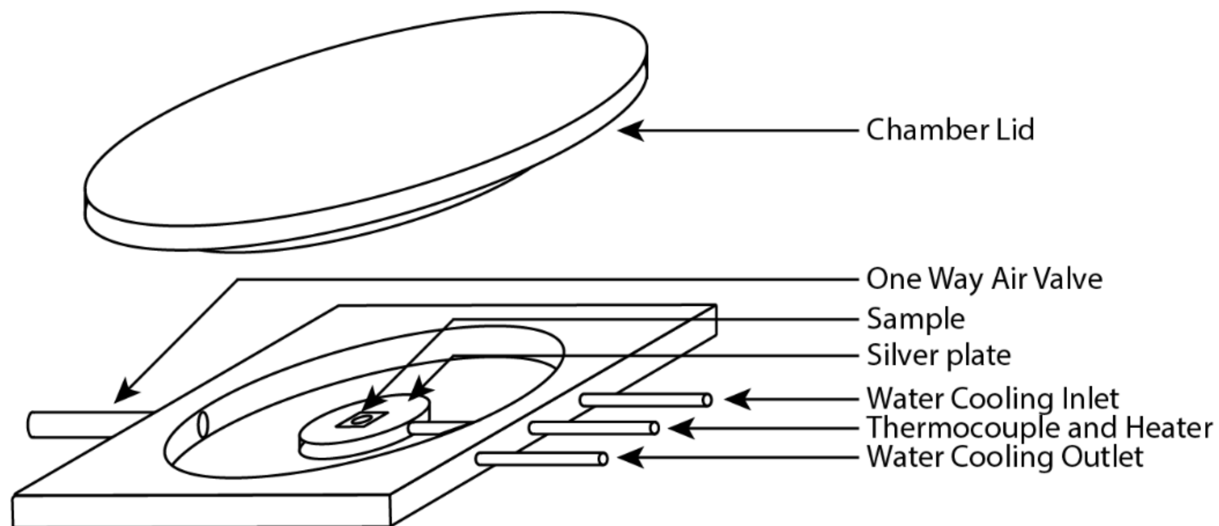

Figure 5.4 Annealing apparatus.

5.1.5 DLTS characterization

The schematic diagram in Figure 5.5 shows the system in which both conventional and Laplace DLTS was done in. The system was comprised of the following:

- Closed cycle helium cryostat used for cooling the system down to as low as 15 K.
- Vacuum Pump to prevent condensation during cooling and provide thermal insulation.
- Insulating sapphire disk to insulate the sample electrically from the cold finger while providing good thermal contact.
- Agilent 33220A Arbitrary Wave Form Generator applying the required filling pulse and quiescent reverse bias.
- Lakeshore 340 temperature controller which is responsible for stabilizing the temperature of the sample using a PID loop.
- Boonton Model 7200 Capacitance Meter which is a high speed instrument measuring capacitance with high precision.

© University of Pretoria

- Offset box connected to the "diff" terminal of the Boonton to reduce the capacitance observed for more sensitive scales.
- Laplace Card which triggers pulses for the wave generator and converts analogue signals from the Boonton into digital data for processing in computers.

The sample is placed on indium foil directly on the surface of the sapphire. Two probes are used, one placed on the Schottky diode and the second placed on the indium foil connected to the ohmic contact of the sample.

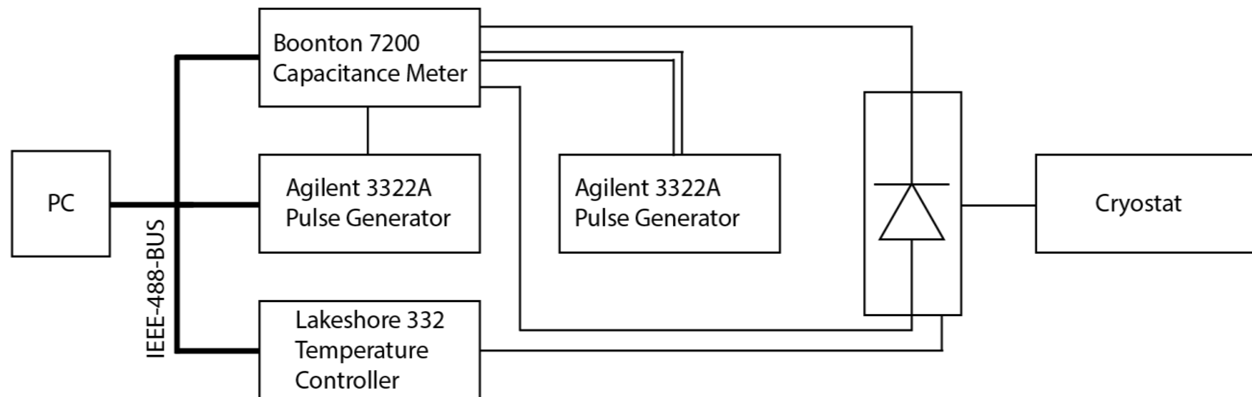

Figure 5.5: *Conventional and Laplace DLTS experimental block diagram setup.*

5.2 References

Auret, F., Goodman, S., Myburg, G. and Meyer, W., 1993. Electrical characterization of defects introduced in n-GaAs by alpha and beta irradiation from radionuclides. *Applied Physics A Solids and Surfaces*, 56(6), pp.547-553.

© University of Pretoria

6 Results and discussion

6.1 Samples and baseline measurements

The samples used in this study came from wafers of phosphorous-doped n-type Si with doping levels of between 3×10^{14} and 2×10^{15} cm^{-3} and different concentrations of C and O, as listed in Table 6.1. The wafers were provided by Fraunhofer Institute for Photonic Microsystems (IPMS), Dresden, Germany. DLTS performed on diodes fabricated on these wafers did not show any defects.

Samples were taken from all 4 wafers and labelled 1 to 4 according to their corresponding wafer number and 500 Å Pd Schottky diodes were deposited on each sample after cleaning. For irradiation, each sample was placed on a mounting plate, ensuring consistent positioning relative to the ^{90}Sr source. Each sample was exposed to irradiation from the ^{90}Sr radionuclide at an ambient temperature of 20 – 21 °C, with Samples 1 – 3 exposed for 18 hours and Sample 4 exposed for 2 hours, since it had a much lower carrier concentration. Typical IV characteristics (Samples 1 – 3) are shown in Figure 6.1. All diodes had series resistance much less than 1 kΩ and leakage current of less than 10 μA at –1V reverse bias, and therefore are suitable for DLTS measurements.

Conventional DLTS (C-DLTS) spectrum (Figure 6.2) and Arrhenius plots (Figure 6.3) were measured directly after irradiation and again after the sample being left at room temperature (24 °C) for 10 days. The properties of the defects are summarised in Table 6.2.

Table 6.1 Summary of the properties of the wafers used in this study (data supplied by the Fraunhofer IPMS).

Substrate number	Description	Growth method	Carbon concentration (cm^{-3})	Oxygen concentration (cm^{-3})	Charge carrier concentration (cm^{-3})
1	Medium carbon and oxygen concentration.	Czochralski	8×10^{16}	3×10^{17}	2×10^{15}
2	Low carbon and oxygen concentration.	Float Zone	5×10^{15}	5×10^{15}	2×10^{15}
3	Low carbon and high oxygen concentration.	Czochralski	6×10^{15}	1×10^{18}	2×10^{15}
4	High carbon and medium oxygen concentration.	Czochralski	6×10^{17}	3×10^{17}	3×10^{14}

When dealing with Si samples containing C, exposure to irradiation is expected to result in the formation of the C_i defect which is highly mobile at room temperature and will migrate and form complexes with the most dominant impurities in the system. In this case P_sC_i, C_iO_i, C_iC_s and $C_iO_i^*$ are the most likely complexes to form. In n-type samples, the formation of the C_i, $C_iO_i^*$ and the C_iC_s electrically active defects are seen by C-DLTS measurements. When left at room temperature for a few days, the $C_iO_i^*$ transforms from its metastable state into the more stable configuration C_iO_i which is visible as a hole trap under minority carrier injection (or directly in p-type samples).

© University of Pretoria

Vacancies are expected to form the divacancy (presenting peaks in two charge states VV^-, $VV^=$), O_iV and P_sV.

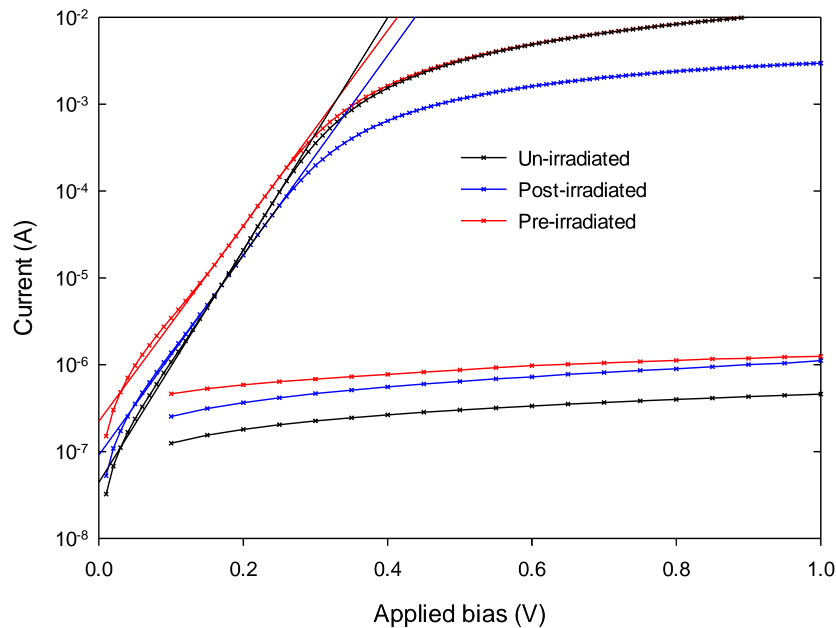

Figure 6.1 Typical IV characteristics of the un-irradiated, pre-irradiated and post-irradiated diodes. The straight lines represent the fit used for the determination of their parameters.

6.1.1 Baseline results: Wafer 1 (Medium carbon and oxygen concentration)

Directly after exposure to irradiation, the common defects C_i, $C_iO_i^*$, VV^-, $VV^=$, O_iV and P_sV were observed in the DLTS spectrum. The O_iV was the dominant peak which was expected, since oxygen was the dominant impurity. A very low concentration of C_i defects was observed due to the majority of them forming bonds with the oxygen present in the sample. C_i defects are more likely to form bonds with the most dominant impurity in the sample, which was observed with the $C_iO_i^*$ complex being the second most dominant peak.

After the sample was left at room temperature for 10 days, the $C_iO_i^*$ and C_i peaks were no longer visible in the conventional DLTS spectrum. The $C_iO_i^*$ transformed to the more stable complex C_iO_i which is not observable in n-type material. The C_i defect migrated and formed complexes with other impurities in the system. Capture-cross section measurements revealed a small portion (approximately 5 %) of the peak observed around 90 K consisted of the C_iC_s defect.

6.1.2 Baseline results: Wafer 2 (Low carbon and oxygen concentration)

Directly after exposure to irradiation, the same common defects observed in Sample 1 were present in Sample 2. In this sample the concentration of C, O and P were roughly equal. The $C_iO_i^*$ complex was present in the sample, however, with its peak close to the freeze-out temperature of Si, the concentration was too low to plot an accurate Arrhenius plot.

After leaving the sample at room temperature for 10 days, the peak observed around 35 K ($C_iO_i^*$) annealed out as expected. The C_i annealed out by migrating to form the stable C_iC_s complex. The concentration of C_i annealing was similar to the increase in the concentration of C_iC_s in the sample.

© University of Pretoria

This shows that in a system with C, O, and P impurities of similar concentration, the C_i is more likely to form a complex with other carbon atoms.

6.1.3 Baseline results: Wafer 3 (Low carbon and high oxygen concentrations)

Directly after irradiation, only some of the defects present in Samples 1 and 2 were present in Sample 3. Due to the extremely high concentration of oxygen, the concentration of the VV and the P_sV were almost negligible in comparison with the O_iV. The C_i peak was not observed after irradiation, however, the carbon related complex $C_iO_i^*$ was observed. The oxygen concentration was sufficiently high to allow the C_i defects to bind with O_i almost directly after introduction. The peak observed directly to the left of the O_iV was found to appear at around 80 K, 10 K higher compared to the C_i peak and was not seen in the other samples. The peak had an activation energy of $E_c - 0.136$ eV.

The only observable change in the sample after leaving it at room temperature for 10 days was the $C_iO_i^*$ peak annealing out, probably by transforming into the C_iO_i. The new peak observed around 80 K and the O_iV peak heights were unaffected, suggesting that no C_iC_s was introduced and that the peak around 80 K is not due to the C_i.

6.1.4 Baseline results: Wafer 4 (High carbon and medium oxygen concentrations)

This sample had a much lower carrier concentration compared to the other samples which only allowed for 2 hours of exposure to the ^{90}Sr radiation nuclei. The sample had an unpolished surface which introduced surface states which were visible on the DLTS measurements. Directly after irradiation it was impossible to measure the sample above 150 K. Below this temperature the same defects were observed ($V_2^=$, O_iV, C_i, C_iC_s and $C_iO_i^*$) with an additional peak around 40 K which was metastable, annealing out when a large bias (-5V) was applied to the sample.

After leaving the sample at room temperature for 10 days, the C_i and $C_iO_i^*$ peaks annealed out. It is assumed that the $C_iO_i^*$ transformed into its more stable C_iO_i complex. The C_i in this sample did not transform into C_iC_s as seen in previous samples. Instead the peak at 90 K which contained C_iC_s directly after irradiation now only consisted of O_iV and a new peak observed around 110 K. It is highly possible for this peak to be carbon related. It was not possible to do measurements above 125 K due to the interference of the surface states.

This sample was deemed unusable for the experiments which are to follow in this thesis. However, this serves as a reminder, showing the importance of polishing samples for the fabrication of electrical devices.

© University of Pretoria

Table 6.2 Table summarizing the defects observed in all 4 samples directly after irradiation by ^{90}Sr and again after the sample was left at room temperature for 10 days.

Defect	Temperature at which peak was observed with rate window 200 s^{-1} (K)	Energy Level Directly after irradiation (eV)	Energy Level After 10 Days At RT (eV)
$C_iO_i^*$	34	S1: $E_c - 0.068$ S2: $E_c - 0.074$ S3: $E_c - 0.068$ S4: $E_c - 0.068$	–
C_i	70	S1: $E_c - 0.111$ S2: $E_c - 0.111$ S4: $E_c - 0.110$	–
Unidentified	80	S3: $E_c - 0.136$	S3: $E_c - 0.131$
O_iV	90	S1: $E_c - 0.169$ S2: $E_c - 0.170$ S3: $E_c - 0.169$ S4: $E_c - 0.169$	S1: $E_c - 0.170$ S2: $E_c - 0.170$ S3: $E_c - 0.169$ S4: $E_c - 0.169$
C_iC_s	90	–	S1: $E_c - 0.169$ S2: $E_c - 0.170$ S3: $E_c - 0.169$
Unidentified	110	–	S4: $E_c - 0.188$
$VV^{=}$	125	S1: $E_c - 0.230$ S2: $E_c - 0.230$ S3: $E_c - 0.230$	S1: $E_c - 0.230$ S2: $E_c - 0.231$ S3: $E_c - 0.230$
VV^{-}	225	S1: $E_c - 0.364$ S2: $E_c - 0.308$	S1: $E_c - 0.364$ S2: $E_c - 0.360$
P_sV	225	S1: $E_c - 0.463$ S2: $E_c - 0.463$ S3: $E_c - 0.462$	S1: $E_c - 0.460$ S2: $E_c - 0.461$ S3: $E_c - 0.465$

© University of Pretoria

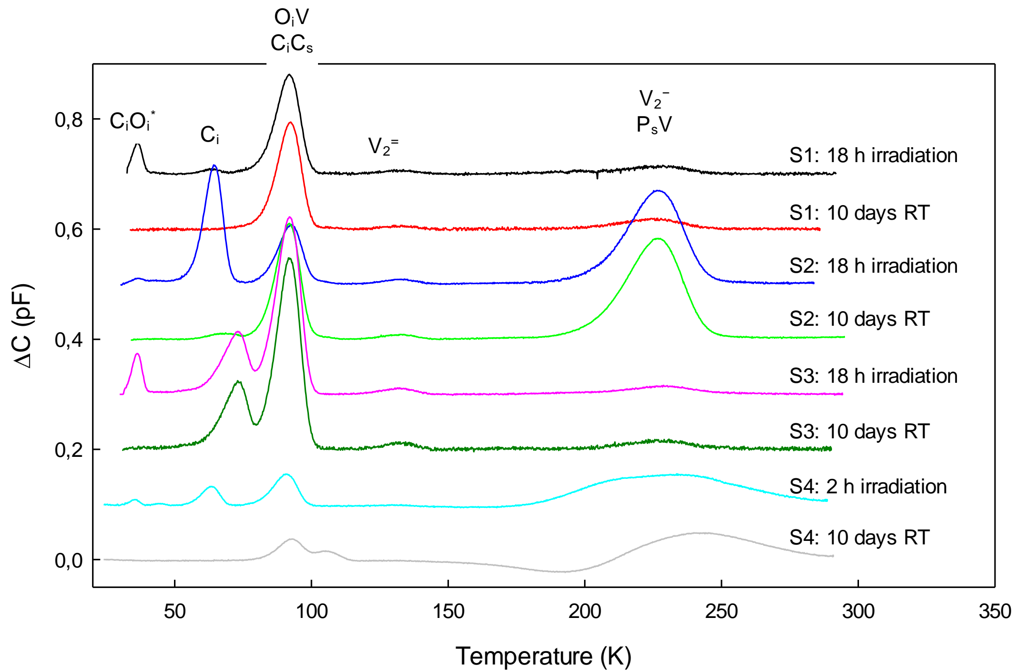

Figure 6.2 DLTS spectra of Samples 1 – 4 directly after irradiation and after being left at room temperature for 10 days. Measured at 1 K/min at 200 Hz under a reverse bias of −2 V and forward bias of 0 V of 1 ms pulse length.

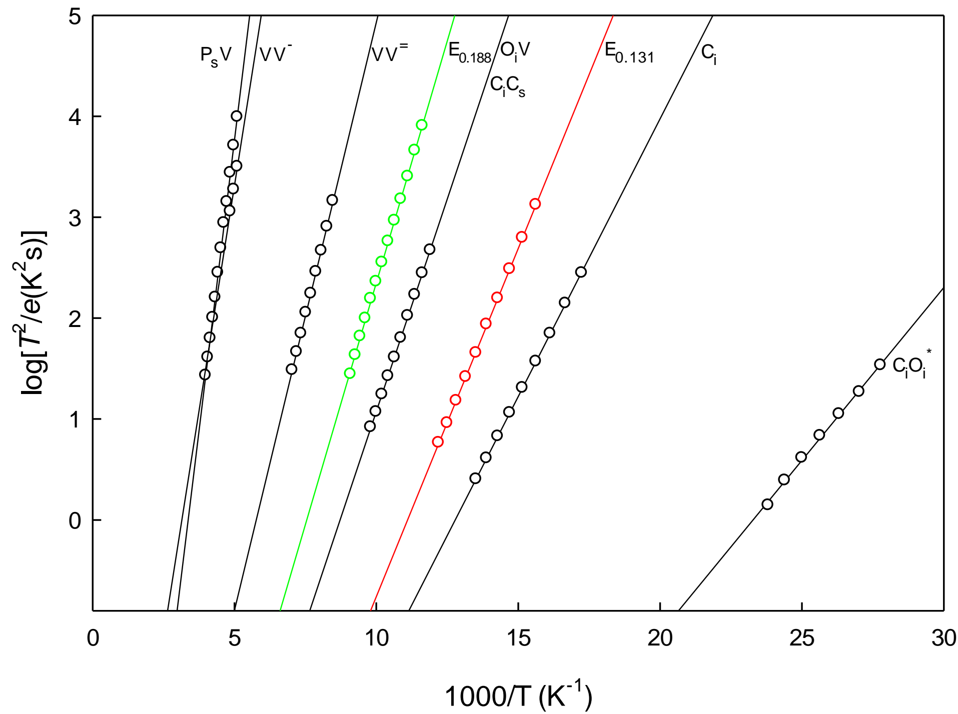

Figure 6.3 Arrhenius-plots comparing the defects observed in the 4 samples. For clarity, the defects measured in Sample 1 are shown in black and the additional defects observed are shown in red (Sample 2) and green (Sample 4).

© University of Pretoria

6.2 The effect of metal deposition

This section focuses on the effect Pd deposition has on radiation induced defects. Multiple species of metals were deposited on the surface of pre- and post-irradiated samples and C-DLTS spectrums were recorded to determine if there was any change to electrically active defects within Si.

6.2.1 Experimental setup

The effect of metal deposition on pre- and post-irradiated samples needed to be explored with different metals. Pd, Au, Ag, Ni and Al were available for investigation. Unfortunately, Pt cannot be used within resistive evaporation setups due to the high melting point of the material. Electron beam deposition or other techniques like sputter deposition will need to be used to investigate this material, however, these techniques usually bring in other defects which complicates the current experiment.

The following experiment explored if other metals exhibited similar effects on irradiation induced defects or if the effect was unique to Pd. The experiment aimed to establish whether the observed effect only manifests after the samples undergo irradiation, or if it can also occur when Schottky diodes are fabricated first and then subjected to radiation. Lastly, the experiment aimed to determine if the Pd affects previously made Schottky diodes exposed to irradiation afterwards when deposited nearby.

Five samples were cut from Wafer 1, large enough for each to accommodate two Schottky diodes. Schottky diodes were fabricated (see Figure 6.4) and measured as follows:

- Sample was cleaned using the steps mentioned in Section 5.1.1.
- A single Schottky diode, 500 Å thick, was deposited using the selected metal on one half of the substrate surface.
- The Sample was exposed to ^{90}Sr irradiation for 18 hours at an average room temperature of 20 to 21 °C.
- Conventional DLTS was performed on the Schottky diode.
- The sample was cleaned using the same cleaning process as previous used.
- The second Schottky diode 500 Å thick, was deposited 0.2 mm from the previous Schottky diode using the same metal.
- Conventional DLTS was performed on the second Schottky diode.
- Conventional DLTS was performed on the first Schottky diode.

It was important to re-measure the first Schottky diode, to see if the deposition of the second Schottky diode had an effect on nearby pre-existing diodes already exposed to irradiation.

The samples were labelled with the chemical symbol of the metal deposited on it and prefixed with “pre” or “post” depending on if the sample was irradiated before or after the metal was deposited (i.e. 1-Pre-Pd, refers to a sample from Wafer 1 exposed to irradiation before deposition of Pd).

© University of Pretoria

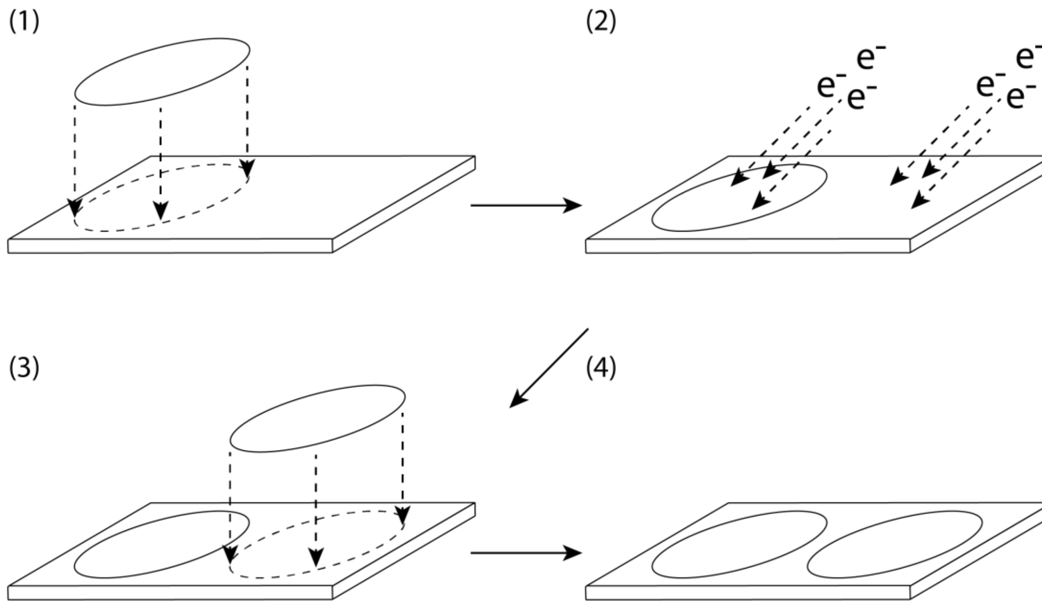

Figure 6.4 Schematic diagram of the procedure showing the selected metal Schottky diode deposited on the first half of the sample's surface (1). The full sample was then exposed to electron irradiation from the ^{90}Sr Source (2). A second Schottky diode was deposited on other half of the sample's surface (3). The resultant sample (4).

6.2.2 Results

The baseline results in Section 6.1 show the defects generally observed in Si devices made in industry then exposed to irradiation. This serves as a baseline for understanding the effect metals have on the substrate before or after exposure to radiation.

The C-DLTS spectrums of the samples irradiated after deposition (Figure 6.5) are similar as well as to the baseline measurements discussed in Section 6.1. All the expected radiation-induced defects were observed with no significant differences. Small variations in the C_i, $C_iO_i^*$ and C_iC_s concentrations were most likely caused by small variations in the temperature as each sample was irradiated on a different day.

The pre-irradiated contacts were deposited on the second half of the surface, already exposed to irradiation earlier. This allows for the fabrication of pre-irradiated Schottky diodes to be comparable to the post-irradiated samples measured earlier, as they were irradiated at the same time and experienced the same temperatures during processing. The C-DLTS spectrums for Au, Ni and Al were similar to their post-irradiated counterparts, with only some change in the C_i, $C_iO_i^*$ and C_iC_s concentration due to thermal contact during deposition. Ag showed some signs of passivating radiation induced defects, with no new electrically active defects being introduced within the n-type material.

Pd had the most interesting effect on the C-DLTS spectrum of the pre-irradiated diodes. None of the radiation induced defects observed in the post-irradiated diodes were seen in the C-DLTS spectrum of the pre-irradiated diodes. Instead, 13 new defects were observed with most energy levels not previously identified. We will refer to this unexpected change in the observed defects as the Pd-effect. Identification of these defects will be discussed in greater detail later in this chapter.

Re-measuring the first (post-irradiated) Schottky diodes on each sample showed that they were unaffected by the deposition of the second (pre-irradiated) Schottky diode next to them.

© University of Pretoria

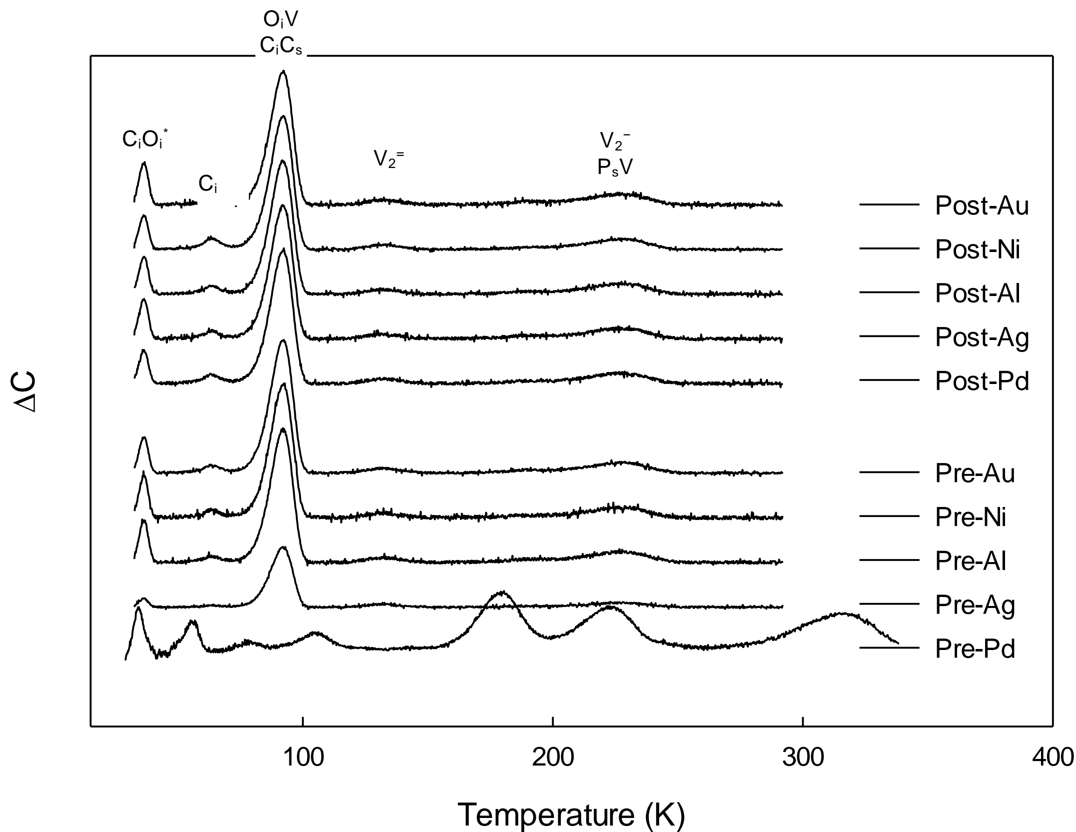

Figure 6.5 C-DLTS spectrums for Schottky diodes of different metals irradiated after deposition (post-irradiated) and before deposition (pre-irradiated). Samples were taken from Wafer 1 and exposed to irradiation for 18 hours at room temperature.

6.3 Effect of an intermediate Au or Pd layer and irradiation through a thick Pd layer

Here the question "Does the deposition of Pd only passivate radiation-induced defects and introduce new defects when making direct contact with the Si surface during deposition." was investigated. Two approaches were taken: firstly, depositing thin Schottky contacts of various thicknesses, then irradiating the samples and then depositing Pd on the contacts of various thicknesses of Pd Schottky diodes. Secondly, covering the surface with a 2 000 Å thick layer of metal, then irradiating the samples through the layer, before removing the metal and depositing Pd Schottky diodes.

6.3.1 Experimental setup

- Two samples large enough to accommodate 5 contacts each were taken from Wafer 1. Using a movable shield, contacts with varying thickness were deposited on the sample. The fabrication and measurement steps were as follows:
- Samples were cleaned using the steps mentioned in Section 5.1.1.
- Schottky diodes were deposited using the setup with a movable shield shown in Figure 6.6. Initially, all contact holes were shielded off from the deposition material until the desired 1 Å/s rate of deposition was achieved. The shield was then moved to expose only the first

© University of Pretoria

contact hole to allow deposition to occur for the first contact. After 20 Å was deposited the shield was again moved to reveal the next contact hole. This was repeated until 4 contacts with thicknesses 20, 40, 60 and 80 Å were on the sample. For the first sample Au was used and for the second sample Pd was used.

- Both samples were exposed to ^{90}Sr irradiation for 18 hours at an average room temperature of 20 to 21 °C.
- Both samples were cleaned again using the steps mentioned in Section 5.1.1.
- Both samples were placed back on the mask with contacts aligned to the holes in the mask.
- 500 Å of Pd was deposited (without the presence of the shield) on top of the four previously created Schottky diodes of varying thickness as well as through a fith hole to form a new Schottky diode. This created five Schottky diodes, one control and four diodes which have had an intermediate layer deposited before irradiation.
- C-DLTS was performed on all the Schottky diodes.

Figure 6.7 shows a diagram of a section through the 5 Schottky diodes which were created.

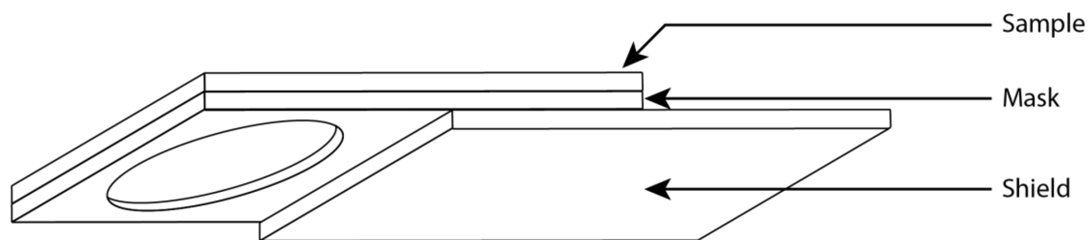

Figure 6.6 The sample was placed on top of the mask with a moveable shield below the mask to selectively prevent metal from being deposited through some of the holes. During the deposition the shield would be slid to the right revealing more holes in the mask to allow more Schottky diodes to form on the surface of the sample. This allowed multiple Schottky diodes with varying thicknesses to be deposited in a single deposition.

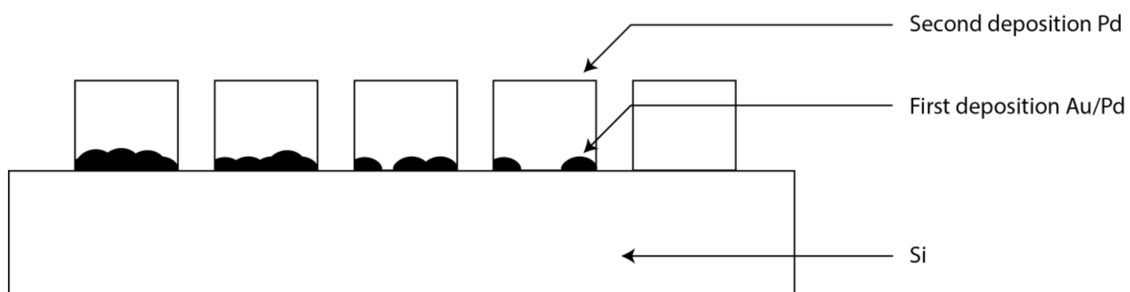

Figure 6.7 Schematic section through the 5 Schottky diodes fabricated on each sample. The first deposition resulted in Schottky diodes with thickness of 0, 20, 40, 60 and 80 Å of Au/Pd deposited. The samples were then exposed to irradiation before a thick layer of approximately 500 Å of Pd was deposited over the previously deposit ed diodes.

- Another limitation was to see if the presence of metal prevents some kind of surface deformation during irradiation. Another sample was taken from Wafer 1. with the Schottky diodes fabricated as follows:
- Sample was cleaned using the steps mentioned in Section 5.1.1
- One half the sample surface had 2 000 Å of Pd deposited on it.
- The full sample was exposed to ^{90}Sr irradiation for 18 hours at an average temperature of 20 - 21 °C.

© University of Pretoria

- The sample was placed in a solution of aqua regia to remove the Pd on the surface.
- The sample was then cleaned using the steps mentioned in Section 5.1.1.
- 500 Å thick Pd Schottky diodes were deposited on both halves of the surface.
- C-DLTS spectrums were measured of Schottky diodes on both surfaces.

6.3.2 Results and discussion

The C-DLTS spectrums of five samples prepared as described in Section 6.3.1 using Au contacts of various thicknesses are shown in Figure 6.8. The defects observed in Section 6.1 were used as a baseline to determine if the new defects exist within each Schottky diode.

The Schottky diodes that had no Au deposited on the surface (0 Å Au), went through the same process as the pre-irradiated Pd sample in Section 6.2, as expected. The full passivation of radiation induced defects was observed with the introduction of the full spectrum of new defects seen in the previous experiment. This set the baseline that the effect of depositing Pd on pre-irradiated samples did occur in the sample. With the second row of Schottky diodes, on which 20 Å of Au was deposited before exposing the sample to irradiation, the deposition of Pd on the sample still had a strong influence on the radiation induced defects. Although it is not clearly visible with most of the defects, the $E_c - 0.17$ eV peak observed in the post-irradiated samples was observed in the C-DLTS spectrum. This suggests that the Pd has to be deposited directly onto the surface in order to fully introduce the new defects and to passivate the radiation induced defects present within the sample.

Both sets of defects were observed in the Schottky diodes where 40 Å of Au was deposited before the irradiation and the deposition of Pd. The radiation induced defects were more visible, with the $E_{0.17}$ clearly present in the spectrum. The Pd-effect was clearly reduced compared to the clean-surface deposition (0 Å Au).

The last two rows had 60 Å and 80 Å of Au deposited before exposure to irradiation and deposition of Pd. Both of the samples showed no indication of the new defects within their C-DLTS spectrums or any signs of passivation. Only radiation induced defects were present within the samples and showed similar spectrums to those observed in Section 6.1 for the post-irradiated diodes.

Resistive evaporation deposition does not proceed in a completely uniform fashion. During deposition, there is a short period where instead of the covering the full surface, small islands form, exposing small gaps of the surface. It has been estimated within the community that a layer of approximately 50 Å would cover the whole surface to fabricate a single Schottky diode.

This experiment was repeated using Pd instead of Au and the C-DLTS spectrums were indistinguishable from those in Figure 6.8. The passivation and introduction of the new defects seems to be blocked by the presence of other metals, including Pd when depositing Pd on samples previously exposed to irradiation.

In the second experiment, the deposition of a 2 000 Å layer, which was removed before the Pd was deposited, the full Pd-effect was observed (i.e. the spectrums were identical to the C-DLTS spectrum observed in Figure 6.8 (0 Å Au)).

With all this information, the effect is limited to only Pd making contact with the Si surface during deposition. Having a metal on the surface, exposing it to irradiation, removing the metal and then fabricating Pd Schottky diodes does not alter the effect at all. Which suggest two things, firstly the

© University of Pretoria

effect can be done multiple times on the same sample, by removing the metal and depositing it again. This would allow for further passivation of radiation induced defects and enhance the introduction of the new defects if the first attempt was not completely successful. Secondly, it is unlikely that a surface deformation was caused by irradiation to allow for the observed effect to occur. The presence of other metals on the Si during deposition prevents this effect from being observed if the Pd was deposited over those metals.

This will give the user control over the fabrication of new devices, as they will be able to limit the passivation of radiation induced defects and the introduction of the new defects. This control is enhanced further as this can be done without affecting devices already present on the same wafer, as the effect does not seem to occur within nearby devices fabricated before this process.

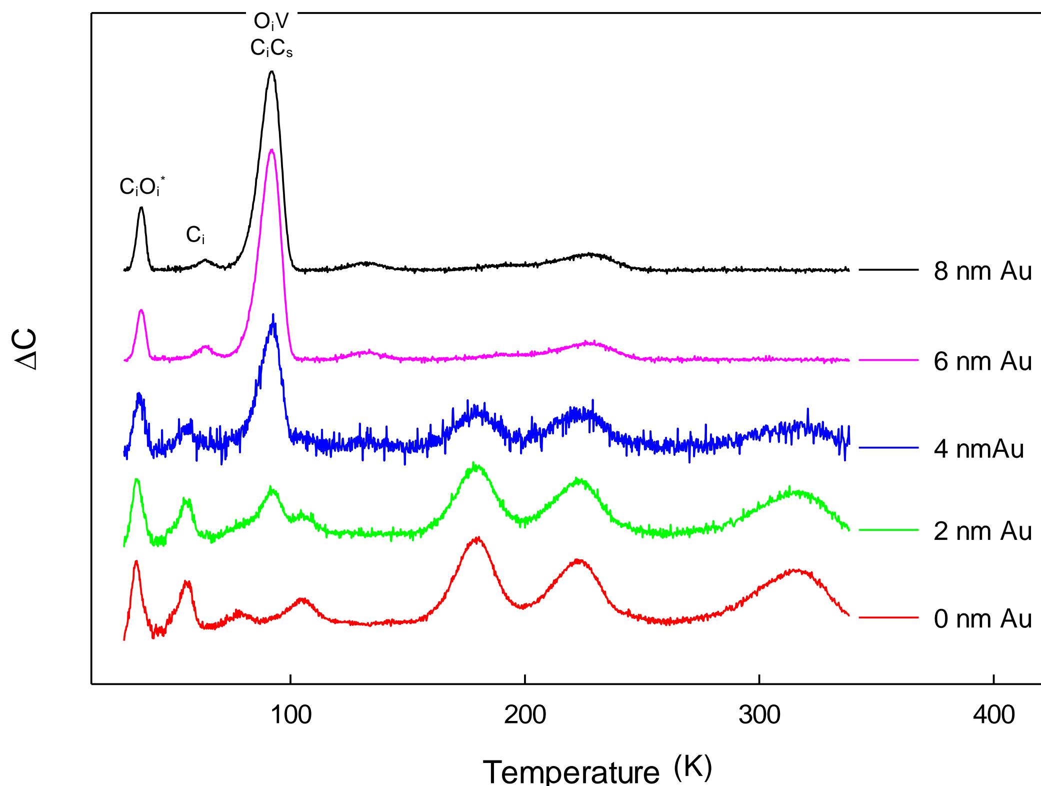

Figure 6.8 C-DLTS spectrums of contacts where different thicknesses of Au were deposited before exposing the Schottky diodes to irradiation followed by depositing 500 Å of Pd.

6.4 H, Pd and contamination

Before delving deeper into the identification and interaction of defects with each other, it is important to eliminate the possibility of hydrogen diffusion or contamination within the Pd. Various forms of Pd (ribbon, pellet, powder) from different sources were used to confirm the repeatability of the Pd-effect. Additionally, the setup from Section 6.3 was used to eliminate the possibility of hydrogen diffusion during deposition.

© University of Pretoria

6.4.1 Experimental setup

Four samples were taken from Wafer 1 and labelled accordingly. Each sample was exposed to Pd from a different source:

- Sample 1: Schottky diodes made from Pd pellets with the crucible used in previous experiments.
- Sample 2: Schottky diodes made from Pd pellets with a new crucible.
- Sample 3: Schottky diodes made from Pd powder with a new crucible.
- Sample 4: Schottky diodes made from Pd ribbon with a new crucible.

Sample 1 will be used as the baseline sample.

The resistive evaporation system underwent a complete cleaning process to ensure there was no contamination from metals previously evaporated in system. The new crucibles were all baked out to remove any contaminants. The Schottky diodes were then fabricated as follows:

- The full sample was exposed to 12 hours of ^{90}Sr irradiation at approximately 20 to 21 °C.
- The sample was cleaned using the steps mentioned in Section 5.1.1.
- The shield used in Section 6.3 was used to control where the Schottky diodes got deposited during the depositions.
- Two crucibles were loaded into the system and shielded off from each other. One crucible had the relevant Pd mentioned earlier and the other crucible had pure Au.
- The sample was then placed under a vacuum of approximately 1×10^{-7} mbar
- While keeping the deposition shield (see Figure 5.3) and the second shield up, the Pd crucible was slowly heated up until a molten state was achieved with a deposition rate of 1 Å/s and kept there for 5 minutes.
- The system shield was completely removed and the sample shield was only partially removed exposing half of the sample surface to the evaporant.
- 500 Å Pd Schottky diodes were deposited during this time.
- Both shields were placed in front of the sample again and the Pd was allowed to cool to close to room temperature.
- While under the same vacuum, the system was set to now use the Au crucible.
- The Au was heated up until melting point and deposition rate of approximately 1 Å/s and kept there for 5 minutes.
- The system shield was completely removed and the sample shield was partially removed exposing the second half of the sample (not previously exposed) to the evaporant.
- 500 Å Au Schottky diodes were deposited during this time.
- Both shields were applied and the Au was cooled down to room temperature.
- Both sets of Schottky diodes were measured using C-DLTS.
- This was repeated for the other 3 samples.

For additional clarification on contamination, Sample 1 was sent for EDX analysis in a scanning electron microscope (SEM) to measure for the presence of contamination.

6.4.2 Results

Previous investigations with regards to de-hydrogenation of Pd showed the removal of the hydrogen already occurring at temperatures below 300 °C (See Chapter 4). The melting point of Pd was found

© University of Pretoria

to be approximately 1550 °C. This is much higher (just over five-fold), which suggests that no hydrogen should be present within the Pd when in a molten state.

Under powerful vacuums, the remainder gas floating around the system can safely be assumed to consist mainly of hydrogen. This allows one to calculate an approximate mean free path for the molecules within the vacuum of the system. The environment temperature measured an average of 25 °C during the experiments. Assuming only hydrogen remains under a vacuum of 1×10^{-7} mbar, the molecule in the form of H_2 has a kinetic diameter of 289 pm. This results in a mean free path of 1109.3 m, which suggests it is highly unlikely for the evaporant to interact with gasses present within the system during deposition.

Sample 1 was selected as the baseline sample, using the pellet Pd and crucible used up into this point of the experiments. By heating up the Pd to a molten state while keeping the shield up allows any hydrogen trapped within the material to evaporate and be removed from the system by the vacuum pumps without affecting the sample. After 5 minutes of evaporating with the shields up, the shields were removed allowing fabrication of the Pd Schottky diodes. These Schottky diodes represent pre-irradiated samples, which passivate radiation induced defects and introduce a new set of defects within their place. Conventional DLTS measurements confirmed the presence of this affect, showing almost identical results seen in previous experiments. The Au Schottky diodes fabricated within the second half of the experiment showed the presence of all the well-known radiation induced defects seen in post-irradiated samples.

Similarly, Samples 2, 3 and 4 all showed identical conventional DLTS spectrums seen within sample 1. Since new crucibles were prepared and used for each material, with the whole evaporation chamber cleaned specifically to eliminate the presence of previous depositions, the likelihood of contamination is unlikely to be caused by the apparatus. The three Pd materials were provided in different forms and came from different manufacturers, yet all produced identical results. The likelihood of dealing with contaminated material can also be considered unlikely.

EDX measurements from the SEM system showed no traces of any other material besides Pd and Si observed from Sample 1 (see Table 6.3). Combine this with the multiple different forms of Pd from different manufacturers and with the environment set up for the experiment, the likelihood of contamination can be safely ignored.

The passivation of radiation induced defects and introduction of the new series of defects were still observed across multiple types of Pd. This was observed after the hydrogen was thermally removed under a powerful vacuum before removing the shields for deposition. This effect was not observed by the deposition of Au Schottky diodes under the same vacuum on the second half of the sample surface. This suggests the evaporation of hydrogen does not cause the passivation of radiation induced defects nor the introduction of the new series of defects. Secondly, from the calculated mean path of the H_2 molecules within the vacuum, the likelihood of the Pd evaporant reacting with H_2 before making contact with the surface of the silicon is highly unlikely.

© University of Pretoria

Table 6.3: SEM results for Pd Schottky Diodes on Sample 1.

Element	Line Type	Apparent Concentration	k Ratio	Wt%	Wt% Sigma	Standard Label	Factory Standard
Si	K series	9.08	0.07194	56.96	0.17	SiO_2	Yes
Pd	L series	4.47	0.04470	43.04	0.17	Pd	Yes
Total:				100.00			

6.5 Isochronal annealing

When confronted with new electrically active defects, one of the first focuses is to determine methods to control their concentration within the samples. Earlier, control over the introduction of these new defects was investigated giving new insight on how to prevent or control the concentration of these defects within the samples. This section will focus on the isochronal annealing profiles to determine the temperatures required to remove or transform the defects. One of the most important features will be determining relationships between the simultaneous removal of some defects, the removal and simultaneous introduction of other defects and defects with unique removal properties. The experiment explored whether the effect appears post-irradiation or with pre-fabricated Schottky diodes exposed to radiation, also using annealing to identify defects.

6.5.1 Experimental setup

Three types of samples were prepared for isochronal annealing profiles. All samples were exposed to ^{90}Sr irradiation for 48 hours at 275 K.

- Sample A1: Pd Schottky diodes were fabricated on a sample taken from Wafer 1 (medium carbon and oxygen concentration), before irradiation. (Post irradiated.)
- Sample A2: Pd Schottky diodes were fabricated on a sample taken from Wafer 1 after irradiation. (Pre-irradiated)
- Sample B1: Pd Schottky diodes were fabricated on a sample taken from Wafer 2 (low carbon and oxygen concentration), before irradiation. (Post irradiated.)
- Sample B2: Pd Schottky diodes were fabricated on a sample taken from Wafer 2 after irradiation. (Pre-irradiated)

The low temperature irradiation was to ensure that as little as possible C_i annealed out during the irradiation process.

All the samples underwent isochronal annealing. The samples were annealed at 5 K increments for 10 minutes per annealing phase. Careful setting of the temperature controller settings limited the temperature overshoot to a mean of 0.6 K with a standard deviation of 0.4 K. Stabilization of each temperature occurred within a mean of 9 seconds from initially reaching the set temperature with a standard deviation of 3 seconds.

6.5.2 Results: Post-irradiated samples

Isochronal annealing profiles from samples A1 and B1 (post-irradiated) focus on profiling the already well-studied radiation induced defects within n-type Si. These profiles are important for

© University of Pretoria

comparison to previous studied profiles and to determine if some of these defects are still present within pre-irradiated samples (Samples A2 and B2). The full isochronal annealing profiles can be seen in Figure 6.9 with the logistic fitting values seen in Table 6.4 which summarizes all the important information.

Table 6.4: Overview of Sample A1 Isochronal Annealing Profiles: S-Curve Analysis with Midpoint Temperature, Annealing Rate, and Defect Concentration Changes

Trap	Introduced/Annealing	Midpoint (K)	Annealing rate (K^{-1})	ΔN_T (cm^{-3})
C_iO_i	1: Annealing	316	- 7.16	1.75×10^{13}
C_i	1: Annealing	307	- 6.50	2.63×10^{13}
C_iC_s VO	1: Introduction	308	+ 6.59	8.64×10^{12}
	2: Annealing	460	- 14.65	2.46×10^{13}
	3: Annealing	594	- 15.45	1.95×10^{13}
VV=	1: Annealing	-	-	-
PV VV-	1: Annealing	341	- 9.90	3.03×10^{12}
	2: Annealing	431	- 20.75	5.61×10^{12}
	3: Annealing	569	- 12.30	2.53×10^{12}

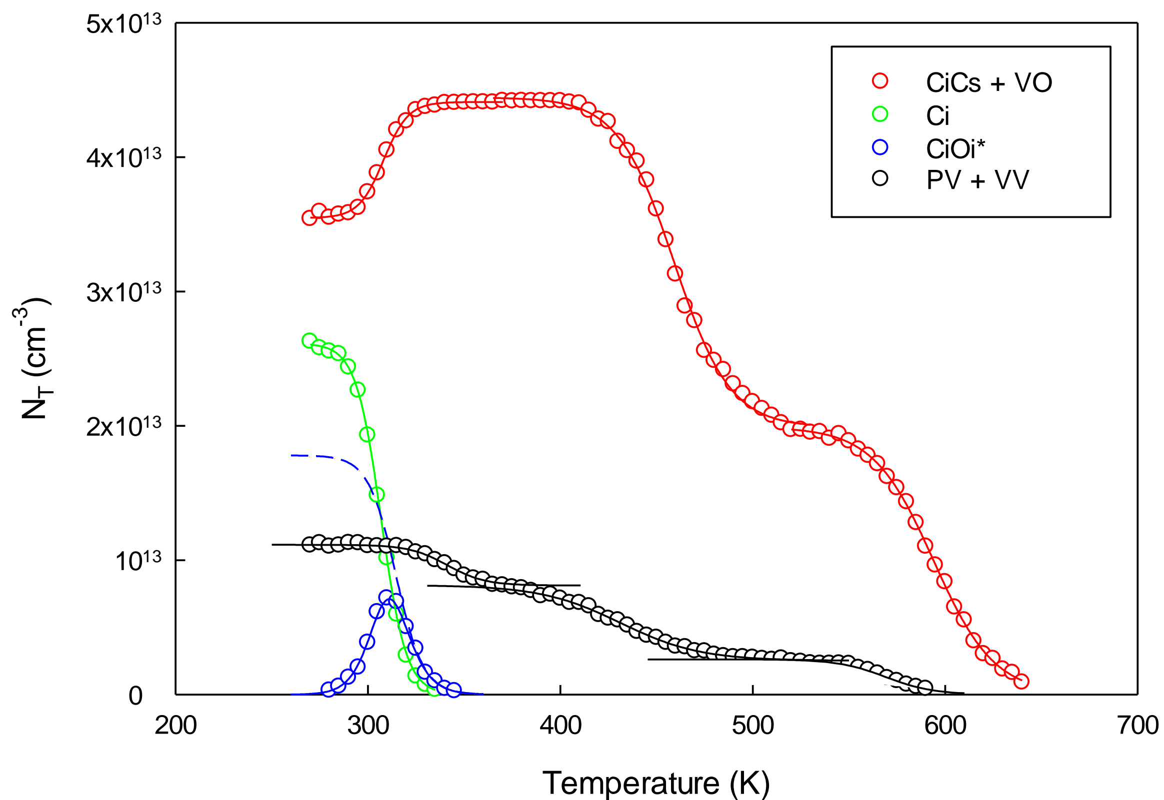

Figure 6.9 Isochronal annealing profiles of Sample A1 with 5 K incremental annealing steps at 10 minutes intervals measured 1 µm beneath the surface junction. Reversed calculation of $C_iO_i^*$ concentration introduced into the sample based on C_i and C_iC_s observed concentration change.

© University of Pretoria

6.5.2.1 $C_iO_i^*$, C_i, C_iC_s and O_iV isochronal annealing relationship

In Figure 6.9 the transformation interactions between the C_i, C_iO_i and C_iC_s peaks for Sample A1 can be observed. The peak observed around 90 K (previously assigned to the C_iC_s and O_iV complexes) was observed to grow before undergoing two separate annealing stages. During the growth phase a complicated series of additional growths and annealing's were observed with the peaks around 35 K and 65 K. The first peak was assigned to the $C_iO_i^*$ complex with the second belonging to the C_i trap. An interesting series of events occurs, initially the $C_iO_i^*$ was not observable within the sample due to the low temperature irradiation which slows down the migration of C_i within Si. However, as the concentration of the C_i starts decreasing, the $C_iO_i^*$ and the concentration of the peak observed at 90 K increased. As the temperature increased isochronally, the C_i annealed out logistically with the critical annealing midpoint observed around 307 K. Similarly, the concentration of the peak observed around 90 K showed a positive logistic observation with a growth midpoint seen around 313 K. In contrast the $C_iO_i^*$ complex showed a more bell curve like introduction which suggested the annealing process started shortly after the introduction process started.

To determine the annealing rate of the $C_iO_i^*$, one can assume the following reactions to take place:

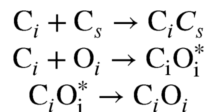

$$C_i + C_s \rightarrow C_iC_s$$
$$C_i + O_i \rightarrow C_iO_i^*$$
$$C_iO_i^* \rightarrow C_iO_i$$

These can be understood as follows: during the annealing period of the C_i, the trap migrates through the sample and forms a complex either with C_s or O_i impurities (first two reactions). The resultant concentration ratio of the two complexes is highly dependent on the concentration of both impurities. The $C_iO_i^*$ is the metastable form of the complex, which transforms into the more stable complex C_iO_i at a higher temperature (third reaction). The stable complex is not measurable within n-type material but can be observed within p-type material. Using this assumption, the introduction rate of the $C_iO_i^*$ can be calculated by using the difference between the introduction rate of the C_iC_s and the removal rate of C_i. The transformation of $C_iO_i^*$ to C_iO_i can be calculated using the difference between the measured $C_iO_i^*$, and the introduction profile calculated for the $C_iO_i^*$. This gave the $C_iO_i^*$ an introduction midpoint temperature of 308 K and an annealing midpoint around 316 K.

With Sample B1, the concentration of C impurities greatly outnumbered the concentration of O within the sample. This resulted in an annealing profile of C_i purely transforming into C_iC_s, with no signs of $C_iO_i^*$ being introduced during the profiling. The annealing midpoint for C_i was found to be 305 K, similar to what was observed within Sample A1.

6.5.2.2 PV and VV^- isochronal annealing

The peak observed around 225 K was previously assigned to belong to the PV and the single negative divacancy, VV^-. The peak was observed to anneal out in 3 stages, which can be seen in Figure 6.9. Previous investigations assign the second annealing stage to the PV with the 3rd annealing stage belonging to the VV^-. It is currently unknown what causes the first annealing stage with some papers assigning this annealing stage as removal of "junk noise". The peaks were indistinguishable from each other in Laplace DLTS measurements.

© University of Pretoria

6.5.3 Results: pre-irradiated samples

Isochronal annealing profiles from samples A1 and B1 (pre-irradiated) focus on profiling the new complexes introduced by the deposition of Pd on pre-irradiated n-type Si. Table 6.5 summarizes the isochronal annealing profiles for the E1 to E14 traps, with Figure 6.10 showing a normalized view of the annealing profiles. The L-DLTS spectrum showing peaks for each defect at critical temperatures is shown in Figure 6.11.

Table 6.5: Sample B1 isochronal annealing profiles: Model fittings and sequence of concentration changes (1-4) indicating multiple annealing profiles for some defects

Trap	Introduced/Annealing	Midpoint (K)	Annealing rate (K^{-1})	ΔN_T
E1	1: Annealing	321	-3.82	3.20×10^{12}
	2: Annealing	400	-7.07	1.52×10^{13}
E2	1: Annealing	338	-7.24	3.14×10^{12}
E3	1: Annealing	359	-7.50	1.60×10^{12}
E4	1: Annealing	337	-7.36	3.02×10^{12}
	2: Introduction	400	+7.11	1.46×10^{13}
	3: Annealing	485	-18.47	2.42×10^{13}
	4: Annealing	679	-30.51	2.19×10^{13}
E5	1: Introduction	385	+5.98	3.54×10^{12}
	2: Annealing	Above 720 K	-	-
E6	1: Annealing	349	-6.85	9.04×10^{11}
E7	1: Annealing	N/A	N/A	9.50×10^{12}
	2: Introduction	458	+8.81	9.59×10^{12}
	3: Annealing	618	-13.08	9.59×10^{12}
E8	1: Annealing	530	-8.45	1.30×10^{13}
E9	1: Annealing	337	-10.96	9.04×10^{12}
E10	1: Introduction	336	+6.53	8.61×10^{12}
	2: Annealing	466	-12.16	1.13×10^{13}
E11	1: Introduction	372	+3.66	5.47×10^{12}
	2: Annealing	497	-5.39	5.47×10^{12}
E12	1: Annealing	Disappeared?	Disappeared?	-
E13	1: Annealing	Disappeared?	Disappeared?	-
E14	1: Annealing	388	-7.08	9.63×10^{12}

© University of Pretoria

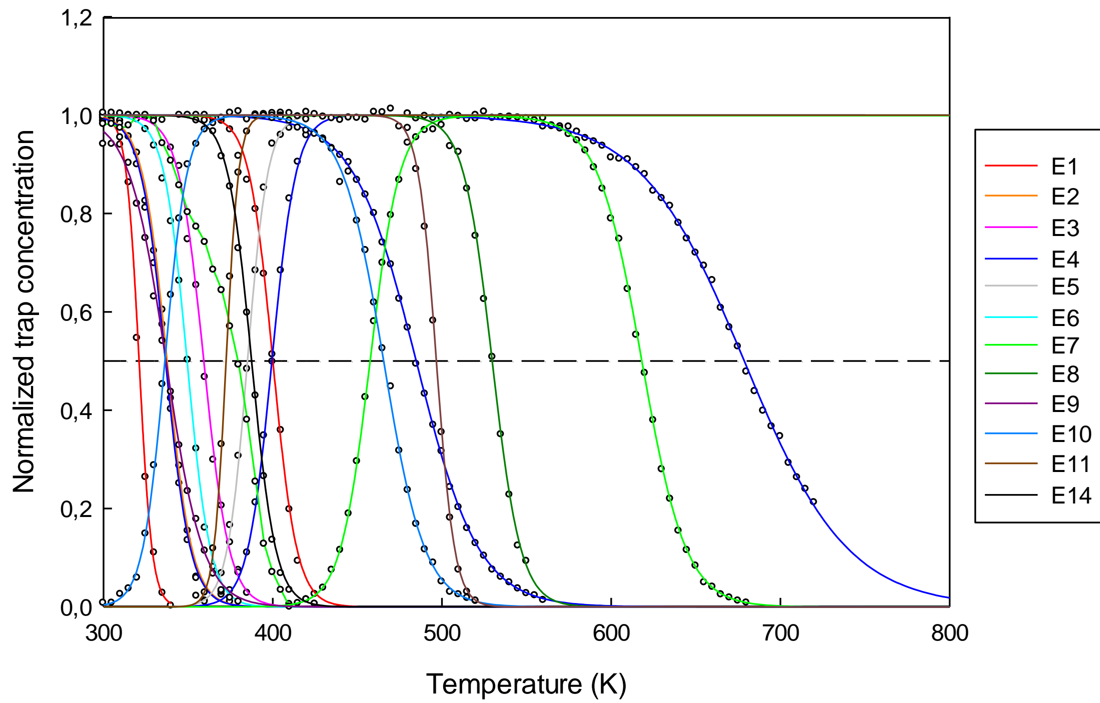

Figure 6.10 Normalized isochronal annealing profiles for Sample A2 with 5 K incremental annealing steps at 10 minutes intervals measured 1 µm beneath the surface of the Si.

© University of Pretoria

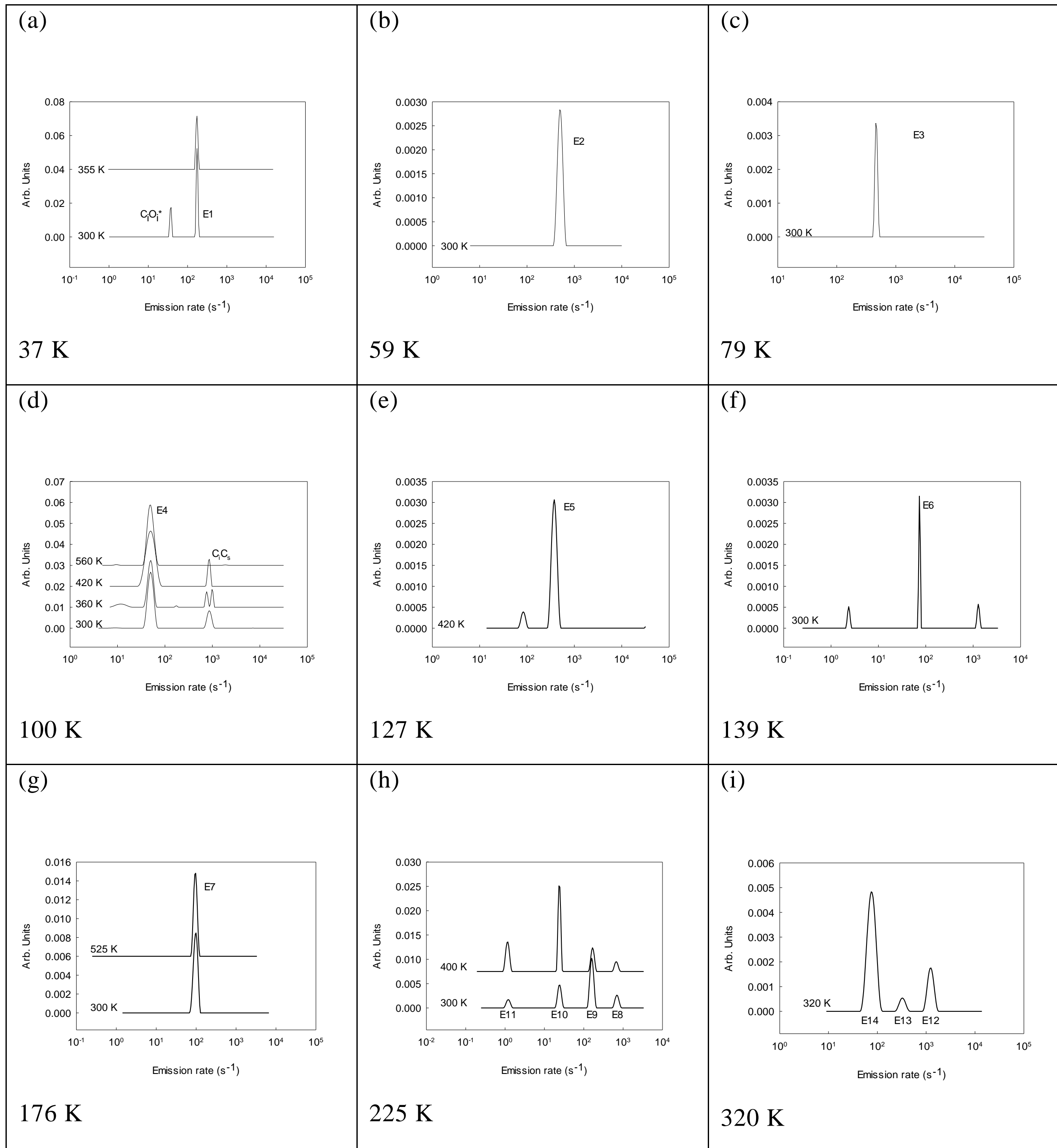

Figure 6.11 L-DLTS signals observed at critical temperatures for Sample A2 throughout the isochronal annealing process. These measurements were done under -2V reverse bias, 0 V filling pulse and a 1 ms filling pulse width.

6.5.3.1 E4

Probably one of the most prominent traps introduced by the deposition of Pd in pre-irradiated samples would be the trap E4. This trap underwent 4 isochronal annealing or growth stages, as shown in Figure 6.12. In the first annealing stage, the E4 concentration decreased by the same amount and rate as that of the E2 (see Section 6.5.3.2), when it annealed out. The second stage was a growth stage where it seemed that the annealing out of the E1 (Section 6.5.3.3) trap introduced

© University of Pretoria

more E4. Hereafter the E4 trap underwent two more annealing stages at higher temperatures. The first of these (the second annealing stage) was observed to start occurring before the growth stage had completed. It was observed to anneal to a constant concentration with a logistic decay constant of -18.47 K^{-1} and sigmoid midpoint of 485 K. The change in concentration was approximately 50 %. There were no observable changes in other trap concentrations which could relate to this trap during this annealing stage. There are a few possible explanations for this annealing stage: The peak could consist of multiple traps, or there might be a defect not observable in this sample which consumes the E4. The logistic decay rate was much slower compared to other traps observed in the system.

E4 underwent a third annealing phase, completely annealing out of the system during this stage. It was observed to anneal with a logistic decay rate of -30.51 K^{-1} and a sigmoid midpoint of 679 K. This annealing phase annealed out at the slowest rate compared to all the annealing rates observed so far, with the annealing occurring over a span of 250 K. Again, there was no apparent relationships with other traps in the sample.

With this information at hand, it suggests a few possible scenarios which will require further studies. During the growth and annealing of this peak, L-DLTS measurements were unable to split the peak and the measured emission rate remained consistent throughout the experiment (Figure 6.11). The prominent scenario would suggest that the E4 complex is a single atom impurity, similar in nature to that of the C_i trap but not highly mobile. In this case, taking into consideration the previous annealing relationships (annealing of the E1, E2 and possible unobservable trap), it is possible that the E2 undergoes dissociation, releasing an impurity that is highly mobile which combines with the E4. At the same time during the second annealing stage of the E1, it would undergo dissociation which introduces more E4 impurities. Similarly, during the second annealing stage, another impurity would combine with the E4 during its annealing making an electrically inactive complex. If this is the case, it would make the E4 trap the most important trap introduced to the system to help determine the complexes produced by the deposition of Pd.

6.5.3.2 E2

The E2 was observed in Sample A2 but not in Sample B2, As discussed earlier, the annealing of the E2 seems closely related to the first annealing stage of the E4, as showed in Figure 6.12. The E2 was observed to anneal out with a logistic decay rate of -7.24 K^{-1} and have a logistic midpoint around 338 K. The first annealing stage observed with trap E4 measured a logistic decay rate of -7.26 K^{-1} and a sigmoid midpoint of 337 K. The concentration of E2 trap that annealed out was 3.14×10^{12} cm^{-3} while at the same time the E4 trap decreased approximately 3.02×10^{12} cm^{-3} in concentration. All three variables are within 1% discrepancy, suggesting there is some form of relationship between annealing out the E2 trap and the effect it has on the concentration of E4 being annealed out at the same time. There was no observable change with the emission rate of the E4 obtained using L-DLTS. It is possible that the E2 trap undergoes dissociation during annealing, resulting in impurities being released into the system. These impurities diffuse and form complexes with the E4 trap resulting in the decrease in E4 concentration. No new complexes were observed and other trap concentrations were unaffected by the annealing of these two traps. This suggest that the new complex might either be electrically inactive or was not observable unless special requirements were met.

For Sample B2, after fabrication, the E2 peak did not show up. This was similar to the $C_iO_i^*$ not appearing in the post-irradiated sample B1, indicating that the E2 defect might be related to the

© University of Pretoria

$C_iO_i^*$. During the annealing of Sample B2, the E4 peak did not have the first annealing stage which was observed within Sample A2.

6.5.3.3 E1

One of the shallowest traps of the new series of Pd deposition induced traps observed would be the E1 trap. L-DLTS measurements clearly showed this trap to have a lower emission rate when measured alongside the C_iO_i* trap. The annealing of this trap was composed of two stages. During the first stage, it rapidly annealed out just above room temperature with a logistic decay rate of -3.82 K^{-1} and with the sigmoid midpoint measuring at 321 K. After the first annealing stage, the trap remains at a stable concentration before undergoing a second annealing stage with a logistic decay rate of -7.07 K^{-1} and a sigmoid midpoint of 400 K annealing out completely. During the first annealing stage, no other trap was observed to undergo annealing or growth with similar annealing kinetics. However, the second annealing stage shared similar annealing kinetics with the E4 trap. During this annealing stage, the E4 undergoes a logistic growth rate of 7.11 K^{-1} with a sigmoid midpoint around 400 K. During this time, the E4 concentration increased with 1.46×10^{13} cm^{-3}, similar to the concentration of E1 removed from the system. There was no observable change to the emission rate or any signs of a new peak being introduced to the system using L-DLTS. Since the two traps share the same change in concentration, have the same sigmoid midpoints and have the same logistic rates with one growing while the other decaying, highly suggests that the two traps share some form of relationship with each other. Similar to what was experienced with E2, E1 might undergo dissociation where either an impurity is released into the system to form the E4 complex, or E1 was a more complicated complex variant of E4 that broke down into the E4 complex.

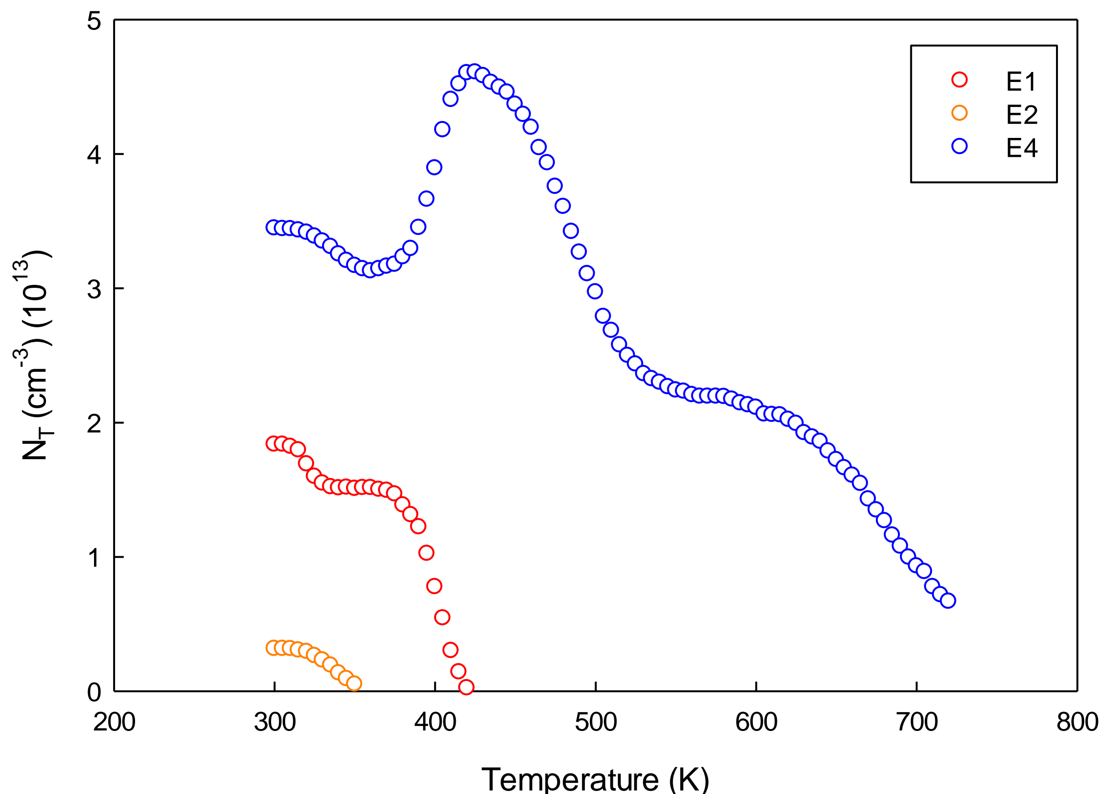

Figure 6.12 Sample A2 isochronal annealing profiles showing the relationship between the E1, E2 and E4

© University of Pretoria

6.5.3.4 E3

The trap E3, had no unique properties showing any form of relationship with other complexes already present within the system. It was observed to anneal out completely with a logistic decay rate of -7.50 K^{-1} and an annealing midpoint of 359 K. No new peaks were introduced to the system during this annealing phase.

6.5.3.5 E6

The trap E6 always had the lowest concentration compared to all the other traps. The concentration measured in A2 coincides with the concentration measured in Sample A1 for the $VV^{=}$, indicating that the E6 might be related to the divacancy. However, further experimentation is required to produce concrete evidence of this relationship between these two traps. A suggested experiment would be to use heavy particles (i.e. alpha-particles) which introduces larger concentrations of di-vacancy complexes and compare if the concentrations are still similar before and after deposition of Pd. Interestingly enough the complex has a logistic annealing midpoint around 349 K which is much lower than the logistic midpoint of 569 K observed for the di-vacancy complex. There were also no signs of the di-vacancy complex being reintroduced to the system as this trap was removed.

6.5.3.6 E7

The trap E7 had the most unique annealing property out of all the new traps observed due to the deposition of Pd (See Figure 6.13). In Sample A2 the E7 initially annealed out completely between 320 K and 410 K with an annealing curve that did not follow the sigmoidal curve shape. Annealing the sample 10 K higher (420 K) initiated the re-introduction of this trap before it started annealing out again around 545 K with it finally being removed from the system around 680 K. During these decay and growth phases, the L-DLTS measurements revealed a single distinct peak which had a constant emission rate throughout the full annealing process (Figure 6.11).

For convenience sake the initial trap which was introduced due to deposition of Pd will be referred to as E7a The shape of the annealing curve obtained for the E7a trap shows signs of consisting of multiple sigmoidal curves. Proper modelling of this curve needs to be done in future research. This may suggest that the removal is caused by multiple traps being removed from the system. Since the trap gets re-introduced to the system at higher temperatures, this suggests that impurities dissociate from another trap, migrate and combine with this trap to form the E7b, resulting in the trap being electrically inactive. No other trap was observed to be introduced while this trap was removed. At temperatures higher than 420 K, the E7a is re-introduced to the system at a logistic rate of 8.81 K^{-1} and annealing midpoint of 458 K. Further increasing the temperature results in the trap finally annealing out with a logistic rate of -13.08 K^{-1} and annealing midpoint of 618 K.

© University of Pretoria

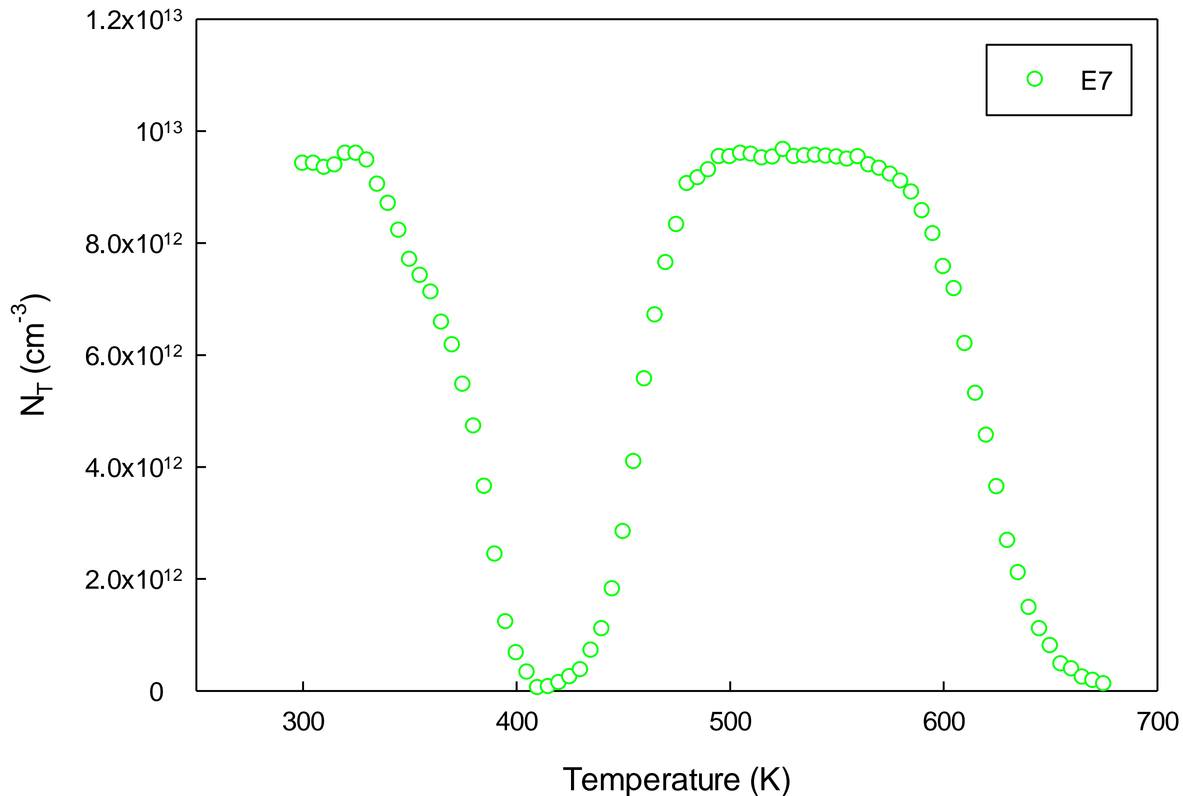

Figure 6.13 Sample A2 isochronal annealing profiles showing the E7 annealing out completely before being re-introduced to the system just to be annealed out at a higher temperature.

6.5.3.7 E8

The E8 trap had no observable unique properties regarding its annealing profile. The trap was observed to anneal out with a sigmoid midpoint of 530 K and a logistic decay rate of -8.45 K^{-1}. There were no observable interactions with other traps within the system during its annealing phase.

6.5.3.8 E11

E11 is a strange trap already present in the system directly after deposition of Pd Schottky diodes. The concentration was observed to increase quite rapidly with a logistic growth rate of 3.66 K^{-1} and a logistic midpoint of 372 K. This trap then annealed out with a logistic decay rate of -5.39 K^{-1} and a logistic midpoint of 497 K. During both stages, the introduction and annealing, did not share any similar annealing kinetics with other traps that were observed in the system. L-DLTS measurements (Figure 6.11) showed a single trap with its concentration undergoing growth and then fully being removed with a single annealing profile at a higher temperature. It is currently unknown where the initial concentration of E11 comes from as the sample did not anneal at temperatures higher than 320 K during deposition of Pd.

6.5.3.9 E12

E12 was another defect with a unique property when compared to other traps. This trap was introduced by the deposition of the Pd Schottky diodes after the sample was exposed to radiation.

© University of Pretoria

However, after the sample was exposed to a reverse bias while at temperatures above 340 K, the trap would be completely removed from the sample. The exact temperature that triggers this event will need to be investigated more thoroughly, however, applying a reverse bias at room temperature and below has not shown any removal of this trap. Currently it does not seem to be reversible using conventional methods, however, further studies are required.

6.5.3.10 E9 and E10

The formation of the E10 trap was observed to be the result of annealing the E9 trap. The E9 complex annealed out with a logistic decay rate of -10.96 K^{-1} and a sigmoid midpoint of 337 K. E10 was introduced with a logistic growth rate of 6.53 K^{-1} and a sigmoid midpoint of 336 K. The concentration of E9 trap removed from the system was equivalent to the E10 introduced during this removal. There are some important features to take note of. Due to the number of complexes observed with L-DLTS, whenever a dominant trap was present, the analysis of the transient would become more complicated. This would explain why the rates would be different but the annealing midpoints would be of similar nature. Interestingly enough, there was already E10 present in the system before annealing. Due to these low temperature annealing kinetics, during the deposition of Pd, the sample would easily reach high enough temperatures where the transformation of E9 to E10 would occur.

The annealing characteristics of the E9 resembles those observed with the first annealing phase of the PV complex seen in Sample A1 (Table 6.4). The midpoint and logistic decay rate were measured to be 341 K and -9.90 K^{-1} respectively. This results in a difference of 4 K and -1.04 K^{-1} for the midpoint and logistic annealing decay rate. The differences between the two would most likely be the result of the complexity of measuring the PV concentration with L-DLTS in A1. It is still currently unknown what causes the first annealing phase of the trap observed at the PV complex. Further studies need to be done of these two complexes which might one day give further insight of the structure if a correlation is found.

It is possible that the E9 and E10 traps are the same complex but in different states. With the E10 being a more stable state. It would then result in E9 transforming into E10 when the samples are exposed to temperatures slightly above room temperature.

At higher temperatures the E10 finally anneals out with a logistic decay rate of -12.16^{-1} K and a sigmoid midpoint of 466 K. There were no observable signs to suggest the annealing of this trap affected the concentrations of other traps that still remained within the sample.

© University of Pretoria

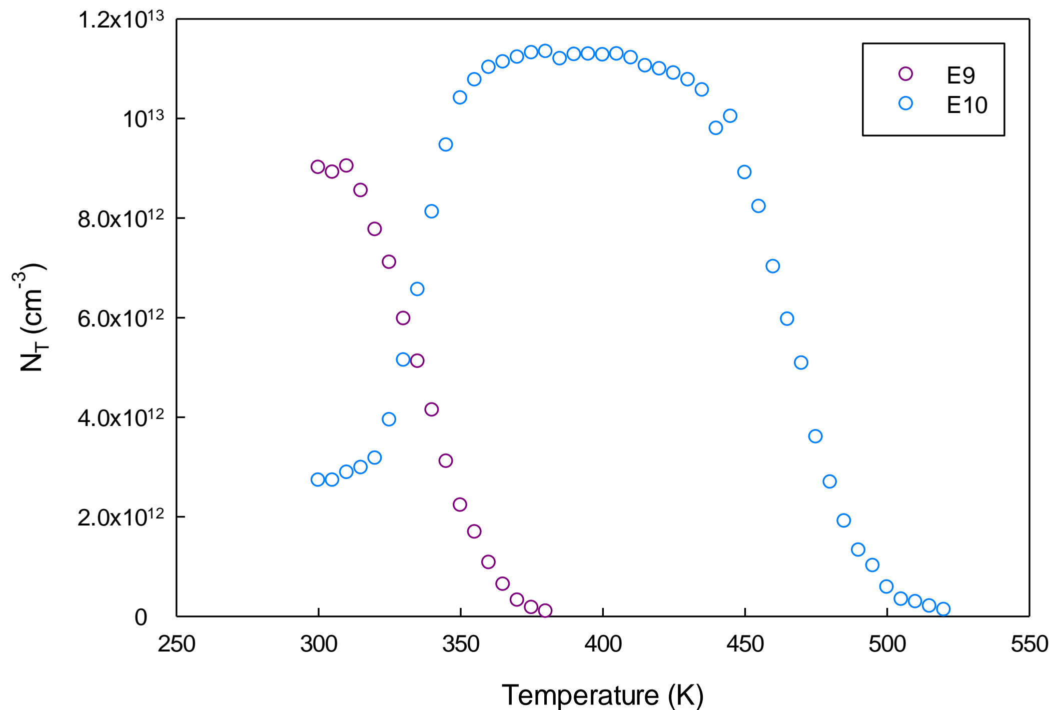

Figure 6.14 Sample A2 isochronal annealing profiles isochronal annealing profiles showing the relationship between the E9 and E10.

6.5.3.11 E14

E14 is the deepest trap measured in Si within pre-irradiated samples, with DLTS measuring its emission signals above room temperature. This trap only undergoes a single logistic annealing stage with a logistic decay rate of -7.08 K^{-1} and a sigmoid midpoint around 388 K. As discussed earlier, this trap shared similar annealing kinetics to trap E5, however, the correspondence was not exact due to deviations in the annealing kinetics and trap concentrations. No other trap measured shared similar annealing kinetic properties linking it to the E14.

6.5.3.12 E5

E5 is another trap that was introduced only after annealing. It grew logistically with a growth rate of 5.98^{-1} K^{-1} and a sigmoid midpoint of 385 K during the isochronal annealing process. This trap was not introduced in Sample A1 or B1 during isochronal annealing, which suggests its introduction was related to the new complexes introduced by the deposition of Pd after exposure to irradiation. During its introduction, the only complex with annealing kinetics which were similar enough to it was the E14 complex. The logistic midpoints differ by 3 K, with E14 having a midpoint of 388 K and annealing out with a logistic decay rate of -7.08^{-1} K^{-1}. Although the midpoints are similar, they are different and the annealing rate was significantly different. Comparing the change in concentration of the two traps, E5 increased with a concentration of 3.54×10^{12} cm^{-3} while E14 decreased with a concentration of 9.63×10^{12} cm^{-1}, which is approximately 3 times the change in concentration E5 experienced. There still lies the possibility that 1/3 of the E14 released into the system combines with something else that is inactive to form the E5. However, it is unlikely that these two traps have a relationship within the system. It is more likely that there are electrically inactive impurities/complexes or even traps that were not observed requiring different conditions to

© University of Pretoria

be measured that create this trap during annealing. It was not possible to observe the annealing phase of E5, mainly due to the samples no longer functioning as intended once exposed to temperatures as high as 725 K. However, this does suggest the trap requires temperatures higher than 720 K to anneal out. This suggests that the trap is highly stable at high temperatures, which is one step closer to identifying the structure.

6.5.3.13 E13

For the trap E13, there is not much information to be given except that it is the second trap that has measurable emission rates above room temperature in Si with DLTS. The trap was only properly visible with L-DLTS once the concentration of E14 was reduced by annealing. This trap seems to exist in very small quantities and suddenly disappears from the system when taking the sample above 420 K.

6.6 Identification of Pd effect complexes

Phosphorous-doped Si was irradiated by electron irradiation from a ^{90}Sr radionuclide source either before (pre-) or after (post-irradiated) deposition of 400-nm thick Pd Schottky diodes. In the case of post-irradiation, irradiation was performed through the Schottky diodes, which were thin enough to allow most of the radiation to pass through unimpeded. The concentration of C_i, $C_iO_i^*$ and C_iC_s was controlled by irradiating at different temperatures. The experiment was repeated a number of times on samples with different carbon and oxygen concentrations with doping levels of about 2×10^{15} cm^{-3}. The carbon, oxygen and charge carrier concentration of the samples are listed in Table 6.1.

6.6.1 Experimental

Multiple samples were taken from Wafer 1, 2 and 3. These samples were either exposed to irradiation at different temperatures before (pre-) or after (post-irradiated) deposition of their Schottky diodes. Schottky diodes were controlled to be 400 nm thick and deposited at a rate of 1 Å/s under a vacuum of approximately 1×10^{-6} mbar. From Wafer 1, the following 8 samples were prepared:

a) post-irradiated sample irradiated at room temperature
b) post-irradiated sample irradiated at room temperature and left at this temperature for 1 week
c) post-irradiated sample irradiated at 275 K
d) post-irradiated sample irradiated at 303 K
e) pre-irradiated sample irradiated at room temperature
f) pre-irradiated sample irradiated at room temperature and left at this temperature for 1 week before deposition
g) pre-irradiated sample irradiated at 275 K
h) pre-irradiated sample irradiated at 303 K

Wafers 2 and 3 only underwent methods a, b, e and f.

6.6.2 Results

The results of a series of experiments for Wafer 1 (with a relatively high carbon concentration) are shown in Figure 6.15. Curves (1a) – (1d) were recorded for post-irradiated samples, while Curves (1e) – (1h) were recorded from pre-irradiated samples (the labelling corresponds to that used in the list above). In the post-irradiated samples (Curves (1a) – (1d)) the DLTS peaks due to the well-

© University of Pretoria

known radiation-induced complexes (C_i, C_iC_s, $C_iO_i^*$, O_iV, VV^-, $VV^=$ and P_sV) (Makarenko *et al.,* 2009), (Shinoda *et al.,* 1992), (Auret *et al.,*2006), (Svensson *et al.,* 1991) were observed. However, in the pre-irradiated samples (Curves (1e) - (1h)), a different set of DLTS peaks were observed. By comparing Curves (1a) and (1b), it is clear that the C_i and $C_iO_i^*$ annealed out when the sample was left at room temperature. When comparing Curves (1e) and (1f), it is clear that the peaks at 55 K (E2) and 80 K (E3) share this same property, therefore it is believed that the E2 and E3 peaks are related to the C_i and $C_iO_i^*$. A more specific assignment may be made by comparing Curves (1c) and (1g), where it is clear that the $C_iO_i^*$ (in Curve (1c)) and the E3 (in Curve (1g)) are not present, we therefore conclude that Pd deposition converts the $C_iO_i^*$ to the E2. Further evidence for this conclusion is found by comparing Curves (1d) and (1h).

The second experiment for Wafer 2 is shown below in Figure 6.16. Similarly, to what was observed in Wafer 1, in the post-irradiated samples all well-known radiation induced complex DLTS peaks were observed but the $C_iO_i^*$ (Curves (2a) & (2b)), while different peaks were observed in the pre-irradiated samples (Curves (2e) & (2f)). The formation of $C_iO_i^*$ was most likely prevented by the low concentration of carbon and oxygen, however, the formation of C_iC_s was still observed. Wafers (2a) and (2e) were irradiated at room temperature and immediately processed and measured, while Wafers (2b) and (2f) were left at room temperature for a week before processing and measurement. Here it was clear that the $C_iO_i^*$ peak observed in Wafer 1 was not present in Wafer 2, while similarly the peak at 55 K (E2) was not present in the pre-irradiated samples. By comparing Curves (2a) and (2b), it is clear that the C_i peak anneals out when the sample is left at room temperature. Similarly, when comparing Curves (2e) and (2f), it is clear that the peak at 80 K (E2) shares this property. Due to the lack of $C_iO_i^*$ formation within Wafer 2, this allowed for the elimination of the two additional steps done in Wafer 1.

The results of the third experiment involving Wafer 3 (with a high O concentration) are shown in the lower half of Figure 6.16. Similarly, to what was observed in the previous samples, in the post-irradiated samples all DLTS peaks relating to well-known radiation induced peaks were observed, in this case, however with the exception of the C_i, while different peaks were observed in the pre-irradiated samples (Curves (3e) & (3f)). An additional peak was observed around 73 K in the post-irradiated samples, likely due to the high concentration of oxygen present. Samples (3a) and (3e) were irradiated at room temperature and immediately processed and measured, while Samples (3b) and (3f) were left at room temperature for a week before fabrication of Schottky diodes and measurements. Unlike in Wafers 1 and 2, it was clear that no C_i was observed in the post-irradiated samples (Curves (3a & 3b)), however, the formation of $C_iO_i^*$ and C_iC_s was observed. Similarly, the peak at 80 K (E3) was not observed in pre-irradiated samples (Curves (3e) & (3f)). By comparing Curves (3a) and (3b), it is clear that the $C_iO_i^*$ peak anneals out when left at room temperature. Similarly, by comparing Curves (3e) and (3f), it is clear that the peak at 55 K shares this property. However, there are some additional peaks observed not seen in Wafers 1 and 2, which could be related to the high concentration of oxygen. In addition to this, it must be noted that the freeze-out temperature was observed around 25 K instead of the usual 30 K range, which allowed for the observation of the very shallow trap.

© University of Pretoria

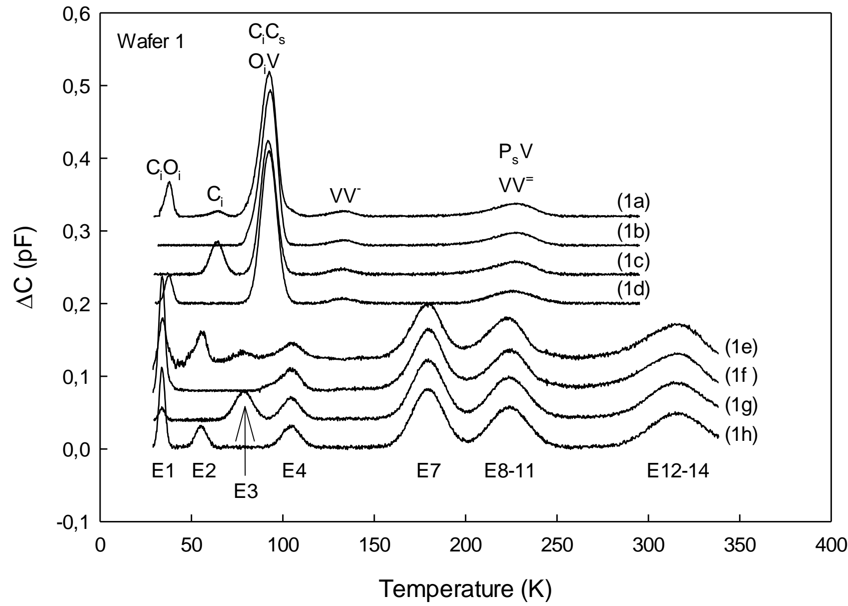

Figure 6.15 C-DLTS spectrums of the 8 samples (Wafer 1) prepared under different conditions. Samples 1a, 1b, 1c and 1d, Pd Schottky diodes were fabricated before irradiation and Samples 1e, 1f, 1g and 1h were fabricated after irradiation. All DLTS spectrums were recorded with a -2 V reverse bias, zero filling pulse, 1 ms pulse length and at 200 Hz.

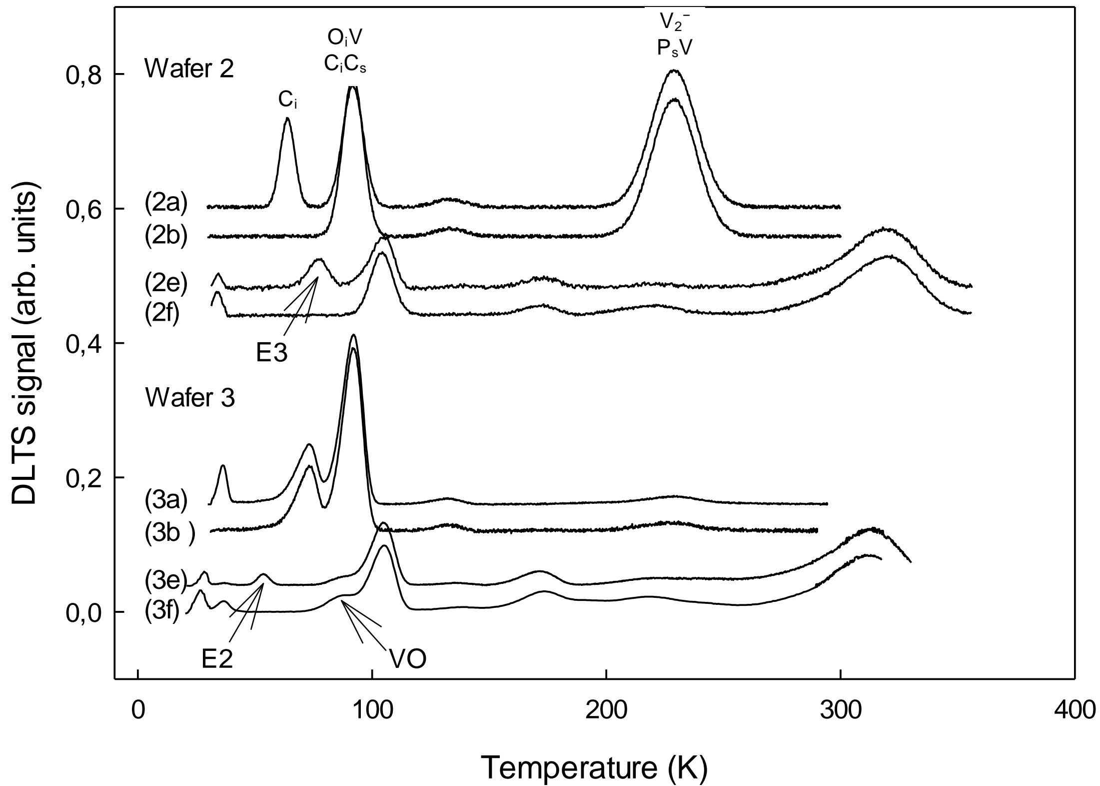

Figure 6.16 C-DLTS spectrums of the 4 samples from Wafer 2 and Wafer 3 prepared under different conditions. Samples (2a), (2b), (3a) and (3b), Pd Schottky diodes were fabricated before irradiation and Samples (2e), (2f), (3e) and (3f) were fabricated after irradiation. All DLTS spectrums were recorded with a -2 V reverse bias, zero filling pulse, 1 ms pulse length and at 200 Hz.

© University of Pretoria

6.7 Arrhenius plots and defect identification

6.7.1 Experiment

The samples produced in Section 6.6 were used to measure the defect energy levels of both the pre- and post-irradiated samples. Sample (1a) produced all the energy levels observed by the well-known radiation-induced defects. This creates a reference for comparing the energy levels of the complexes introduced by the deposition of Pd on pre-irradiated samples. Samples 1(e), 2(e) and 3(e) will be referred to as pre-1, pre-2 and pre-3 which produced the new energy levels observed in pre-irradiated samples. In order to minimise the field effect, the Arrhenius plots were obtained from subtracting two transients obtained under different forward biases, each with a pulse width of 1 ms, while the sample was placed under a quiescent reverse bias of -2 V.

6.7.2 Results and discussion

In the post-irradiated sample (refer to Figure 6.17), a total of seven traps were observed (E_c – 0.068, E_c – 0.111, E_c – 0.169, E_c – 0.169, E_c – 0.230, E_c – 0.355, E_c – 0.463 eV) with energy levels matching the literature values of the C_iO_i, C_i, C_iC_s, O_iV, VV and P_sV (E_c – 0.06, E_c – 0.12, E_c – 0.17, E_c – 0.170, E_c – 0.230, E_c – 0.360, E_c – 0.470 eV respectively) complexes. However, in the pre-irradiated samples a total of 14 defects were observed, significantly more than in the post-irradiated sample. The new energy levels observed were very different from the well-known radiation-induced complexes.

The E12 and E13 could not be measured since the E12 annealed our rapidly under reverse bias at 330 K and the E13 was difficult to measure due to the interference of noise observed with L-DLTS.

6.7.2.1 Comparison with Pd-related defects reported in literature

Gill *et al*. investigated Pd doped samples, and observed four deep levels: E_c – 0.180, E_c – 0.220, E_c – 0.370 and E_c – 0.590 eV. These correspond closely to the E4, E5, E7 and E14, respectively, observed in the present study, as shown in Table 6.6. In most previous as-diffused studies, only the E4 (E_c – 0.180 eV) and E5 (E_c – 0.220 eV) were observed, while the E7 and E14 were only observed in p^+n junctions by Jie *et al.* and Gill *et al*. Interestingly, Jie *et al.* only observed the E4 and E5 traps after annealing the p^+n samples at elevated temperatures. The energy level reported for E14 by Jie *et al.,* was significantly higher (E_c – 0.620) compared to the value reported by Gill *et al*. This conflict was later revised by Gill *et al.,* who arrived at the value of E_c – 0.590 ± 0.01 eV for the E14 energy level. The E7 and E14 traps were reported to be the dominant levels in the p^+n samples with roughly equal concentrations observed by Jie *et al.,* while the E4 and E5 levels were dominant in the p^+n samples observed by Gill *et al*. In the three pre-irradiated samples investigated in this report, the dominant peak would alternate between the E4, E7 and E14, depending on the sample history and exposure time to radiation.

In the case of the E5 level, it was not identifiable in any of the three pre-irradiated samples until they were subjected to annealing at temperatures exceeding 370 K. It's worth mentioning that once introduced, the E5 level in pre-irradiated samples exhibited high stability, remaining intact even at temperatures above 700 K. Previous studies suggested that the high thermal resilience of E5 could link it to a Pd-substitutional trap.

On the other hand, the E4 level behaved differently. As per Gill and his team's findings, the E4 level (E_c – 0.220) would manifest after the device fabrication process and remain stable up to roughly

© University of Pretoria

600 K. Beyond this temperature, its concentration would incrementally rise with the annealing process. Interestingly, in pre-irradiated samples, the E4 level would anneal out while the E5 level remained stable. Previous research proposed a correlation between E4 and the Pd-vacancy complex due to these unique behaviours.

6.7.2.2 Comparison with H-related defects reported in literature

In a previous study, it was proposed that hydrogenation A-centers results in E4-complexes (O_iV), each containing two hydrogen atoms. The study further introduced the concept of an A-H1 complex, a variant with a single hydrogen atom. The A-H1 complex was believed to be undetectable due to its closely aligned energy level with the A-center. The complex measures an energy level of 0.32 eV while observed to anneal out above 620 K. For comparison, the E7 was investigated, measuring an energy level of 0.360 eV. This defect was observed to anneal out at temperatures above 600 K. Earlier experimentations ruled out the possibility of hydrogenation contamination, however, similarities do persist between these two defects.

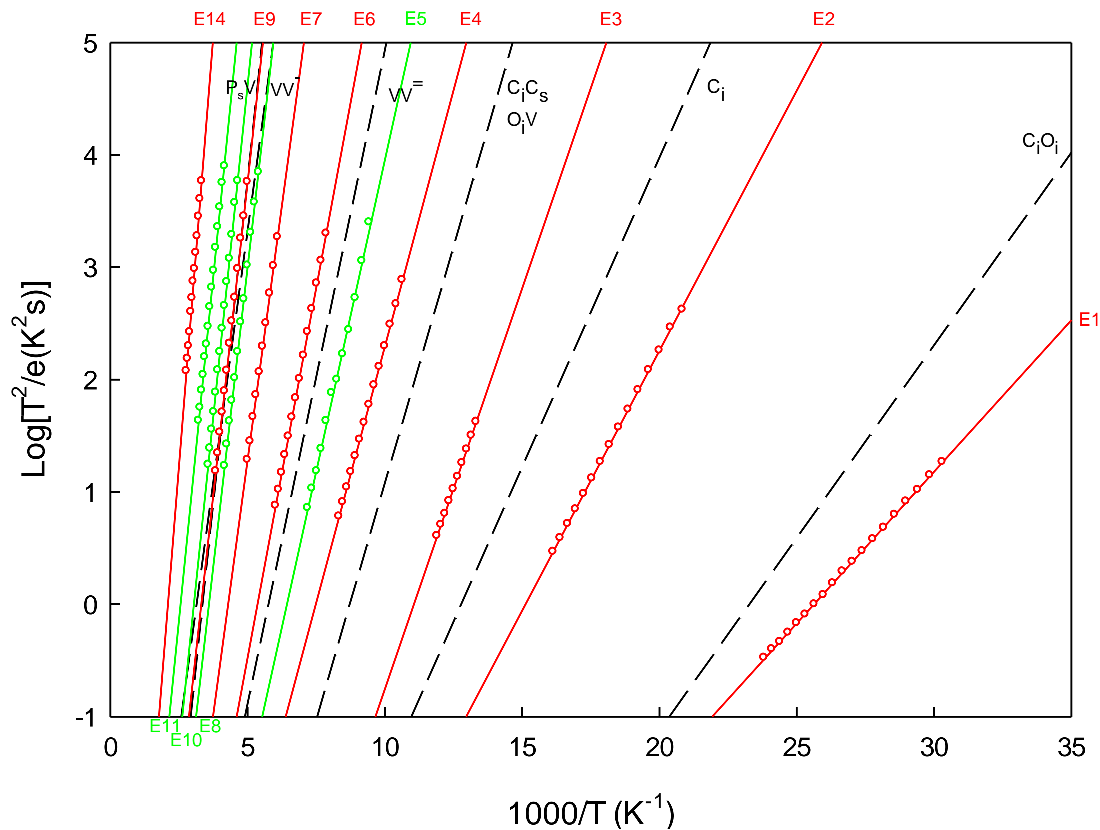

Figure 6.17 Arrhenius measurements of emission activation energy for the pre-irradiated samples directly after deposition (red) and introduced during annealing (green).

© University of Pretoria

Table 6.6: Electrical properties of defects observed in Wafer 1.

Defect	Activation enthalpy (meV)	Temperature observed by DLTS at 200 Hz (K)	Apparent capture cross section (cm^{-2})	Annealing	Ref	Assignment
C_iO_i	68	37	3.2×10^{-14}			C_iO_i
C_i	111	65	3.7×10^{-15}			C_i
C_iC_s	169	92	7.5×10^{-15}			C_iC_s
O_iV	169	92	7.5×10^{-15}			O_iV
$VV^{=}$	230	133	1.7×10^{-15}			$VV^{=}$
VV^{-}	355	228	1.4×10^{-16}			VV^{-}
P_sV	463	228	2.0×10^{-14}			P_sV
E1	53	33	2.8×10^{-15}			
E2	92	54	3.4×10^{-15}			C_iO_i*-related (H/Pd)
E3	140	75	2.6×10^{-14}			C_i-related (H/Pd)
E4	182	102	2.2×10^{-15}	In: 400 K Out: 485 & 679 K	This	
	180	100 @ 229 Hz	8×10^{-16}	In 400 K Out: 600 K	Gill (1993)	PdH_2/PdV
E5	220	119	4.6×10^{-15}	In: 385 K Out: stable.	This	
	220	120 @ 229 Hz	3.4×10^{-15}	In unannealed Small incr. 490 K Rapid incr. 620 K Out: stable.	Gill (1993)	Pd_s
E6	261	140	3.8×10^{-15}			
E7	360	175	2.1×10^{-14}	In unannealed Out: 380 K	This	
		175	2.4×10^{-14}	Back: 458 K Out: 618 K		
	370	175 @ 229 Hz	6.6×10^{-14}	In unannealed Out: 380 K	Gill (1993)	Pd_i
	320		2.1×10^{-14}	Out: >620 K	Feklisova (1999)	
E8	423	195	1.5×10^{-14}			
E9	443	220	8.4×10^{-15}			
E10	469	234	5.3×10^{-15}			
E11	486	265	6.2×10^{-16}			
E12	—	310	—			
E13	—	315	—			
E14	607	320	9.0×10^{-16}	In: unannealed Out: 388 K	This	Pd_i-related
	590	310 @ 229 Hz	2.3×10^{-16}	In: unannealed Out: 410 K	Gill (1993)	

© University of Pretoria

6.8 Depth profiling

Control over the charge carrier life time requires a deeper understanding of the distribution of defects beneath the junction of the metal-semiconductor surface. The distribution of these defects will determine if the defects produced are limited to the surface, penetrate deeper uniformly or penetrate deeper and form concentrated areas. Depth profiles were measured for defects found in both pre- and post-irradiated sample.

6.8.1 Experiment

Two types of samples were prepared from Wafer 1 for depth profiles. Both samples were exposed to Sr^{90} irradiation for 48 hours at 297 K.

- Sample A1: Pd Schottky diodes were fabricated on a sample taken from Wafer 1, before irradiation. (Post irradiated.)
- Sample A2: Pd Schottky diodes were fabricated on a sample taken from Wafer 1 after irradiation. (Pre-irradiated)

Depth profiles were measured under a reverse bias of V_r = -5 V, a pulse width of 1 ms and a double filling pulse. The measured change in capacitance for both pulses were subtracted from each other after each measurement before being averaged for the inverse Laplace calculations. The difference between the pulses remained 0.1 V, with the applied voltage decrementing by 0.1 V for both pulses for each measurement.

6.8.2 Results

Sample A1 showed uniform depth profiling below the metallurgical junction for all the observed traps. The traps observed were the result of exposing a Si based Schottky diode to a ^{90}Sr source. Due to the high energy of the electrons penetrating through the sample, the traps were created well below the depth ranges that can be probed. The profiles showed that the sample was uniformly doped with P during fabrication, with the contamination of O and C also introduced uniformly.

Depth profiling for Sample A2 showed their concentrations to be uniform below the metallurgical junction in the depth ranges that could be probed. The depth profiles of E1, E2, E3, E4, E5, E7, and E14 are shown in Figure 6.18. The sample was then isochronally annealed for 15 minute intervals in 10 K increments to introduce the E5 for depth profiling.

Depth profiling was too complicated to distinguish between the E8, E9, E10 and E11 point defects. The emission rates were too similar for L-DLTS to properly determine the correct concentration of each impurity. However, it is important to note that the combined concentration of the E9 and E10 was seemingly uniform. The trap E12 was removed from the system as soon as the sample was placed under a reverse bias at 320 K.

Depth profiling observed by Gill *et al.,* had notable features which were not observed in Sample A2. The E_c – 0.180 and E_c – 0.220 (E4 and E5) in this study were observed to be uniformly distributed below the metallurgical junction, however, the E_c – 0.370 (E7) and E_c – 0.590 eV (E14) in the study by Gill *et al.* were found to be concentrated in the region close to the junction while rapidly decreasing when moving slightly away from junction. It was observed in Sample A2 that all four deep levels were uniformly distributed up to 2 µm below the junction, similar to what was observed with the radiation induced traps in the post-irradiated sample (A1).

© University of Pretoria

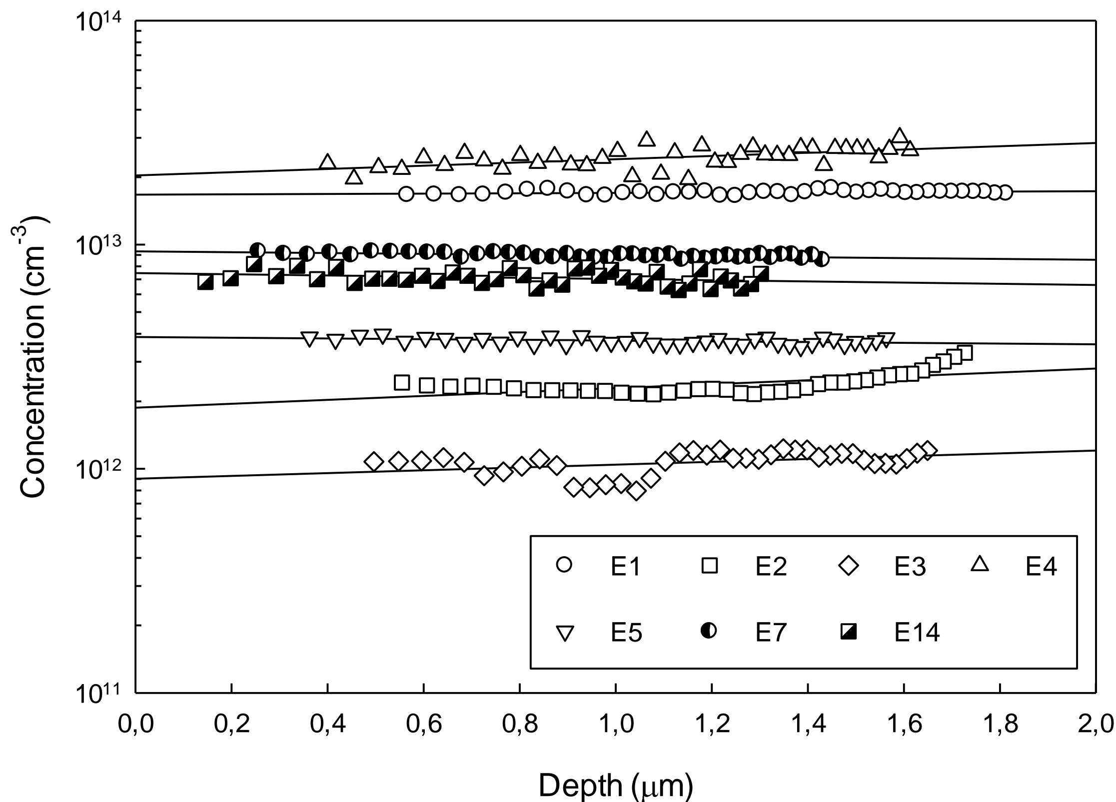

Figure 6.18 The depth profiles of E1, E2, E3, E4, E7 and E14 recorded in Cz Si after a Pd Schottky diode was resistively evaporated onto a pre-irradiated Sample 1 (See Figure 6.2). The depth profile of E5 was recorded after the sample was annealed at 400 K.

6.9 References

Auret, F., Peaker, A., Markevich, V., Dobaczewski, L. and Gwilliam, R. (2006). High-resolution DLTS of vacancy–donor pairs in P-, As- and Sb-doped silicon. *Physica B: Condensed Matter*, 376-377, pp.73-76

Feklisova, O. *et al.* (1999) 'Hydrogen interaction with defects in electron-irradiated silicon', *Physica B: Condensed Matter*, 273–274, pp. 235–238. Doi:10.1016/s0921-4526(99)00461-5.

Gill, A., Iqbal, M. and Zafar, N. (1993). Palladium-related deep levels in silicon. *Semiconductor Science and Technology*, 8(5), pp.675-681.

Jie, Z., Shengyang, R., Hong, H., Weikun, G., Xiujiang, J. and Shuying, L. (1986). The interaction of radiation defects and Pd-related centers in silicon. *Chinese Physics Letters*, 3(1), pp.5-8.

Makarenko, L., Korshunov, F., Lastovskii, S., Murin, L. and Moll, M. (2009). DLTS Studies of Carbon Related Complexes in Irradiated N- and P-Silicon. *Solid State Phenomena*, 156-158, pp.155-160.

Shinoda, K. and Ohta, E. (1992). Interstitial carbon-oxygen complex in near threshold electron irradiated silicon. *Applied Physics Letters*, 61(22), pp.2691-2693.

© University of Pretoria

Svensson, B., Mohadjeri, B., Hallén, A., Svensson, J. and Corbett, J. (1991). Divacancy acceptor levels in ion-irradiated silicon. *Physical Review B*, 43(3), pp.2292-2298.

© University of Pretoria

7 Discussion and Conclusion

The upcoming section offers a concise summary of the results outlined in Chapter 6, aiming to enhance the clarity of the discussion. It delves into possible structures and transformations of the traps identified in pre-irradiated samples during the annealing process. Lastly, this section serves to conclude the thesis and encapsulate the research findings.

7.1 Summary overview

Exposing Schottky diodes to electron irradiation from a ^{90}Sr radiation source resulted in the formation of the well-known radiation-induced traps in Si. The experiments showed the formation of $C_iO_i^*$, C_i, C_iC_s, O_iV, VV and P_sV within P-doped Si wafers. In addition, their isochronal annealing profiles agreed with those reported in literature. However, exposing the Si substrate to electron irradiation before the fabrication of Pd Schottky diodes resulted in a new series of traps. Of these, the majority were stable directly after fabrication, a few were removed when the diode was placed under reverse bias at temperatures above room temperature and others were introduced once the device was annealed at higher temperatures.

This phenomenon was shown to be limited to Pd. In contrast, Ni, Al and Au gave the same range of electrical active traps irrespective of the substrate being exposed to irradiation before or after fabrication of the relevant Schottky diodes. Ag showed some passivation of peaks, but did not introduce any new peaks in the pre-irradiated samples. The effect was observed with Pd from different sources and different forms (ribbon, pellet, powder).

The observed effect was constrained to the initial 60 Å of Pd deposited on the surface of pre-irradiated Si samples. When fabricating Au or Pd Schottky diodes with a thickness of at least 60 Å, subjecting them to irradiation, and then adding Pd on top, there was no passivation of the radiation-induced traps or the emergence of new ones.

The risk of contamination was thoroughly dismissed after a complete maintenance and cleaning of the deposition chamber, complemented by the usage of brand new crucibles for deposition. This was later corroborated by Energy-Dispersive X-ray Analysis (EDXA) measurements in a Scanning Electron Microscope (SEM), verifying the purity of Pd and Si. The influence of hydrogen was ruled out by fully shielding the substrate prior to deposition. Furthermore, none of the newly observed peaks corresponed to peaks attributed to hydrogen in literature.

The new range of traps that emerged from pre-irradiated samples, exhibited a diverse array of unique annealing profiles, with a number indicating interaction between defects. These profiles can be succinctly summarized in the subsequent points:

- E1, E2 and E4:
    - During isochronal annealing, the concentration of the E1 trap showed a decrease in concentration that was identical to the rate and concentration decrease of the E4 trap. It's important to note that the E4 only reduced in concentration within this temperature range in samples where E1 was concurrently present during the annealing process.
    - The E2 trap underwent two phases of annealing, with a reduction in its concentration evident in both phases. Interestingly, during the second phase, as the concentration

© University of Pretoria

of E2 diminished, the concentration of the E4 trap increased at an equivalent rate. This implies that the rate at which E2 was eliminated from the system was exactly matched by the rate at which E4 was introduced.
    - The E4 trap was found to undergo a total of four annealing stages. The first two stages, already detailed in the previous points, saw the trap's concentration decrease and then increase. In the following two stages, the E4 trap also showed a reduction in concentration. The initial phase of these last two stages was marked by a swift decrease, while the second phase was characterized by a slower, yet steady reduction over a broader temperature range.
- The E3, E6, and E8 traps each displayed a single annealing phase, and they did not share any observable interrelation with other traps during their removal from the system.
- The E5 trap did not appear immediately following device fabrication. However, upon raising the temperature above 350 K, the E5 manifested, as indicated by the observed introduction profile. Concurrently, E14 underwent a singular annealing phase, leading to its total elimination from the system. Despite identical temperature ranges for these processes, there was a significant difference in the rates. The concentration decrease of the E14 removed from the system was three times the concentration of the E5 introduced. Hereafter, the E5 concentration maintained stability at elevated temperatures, even beyond 720 K.
- The E7 trap underwent three annealing phases. In the initial phase, the trap was entirely eliminated from the system. Subsequently, with a minor temperature increase of 20 K, the trap was reintroduced, restoring its concentration to the initial value as the temperature increased. This concentration persisted until a final annealing phase at an increased temperature where the trap was completely annealed out at around 680 K.
- E9 and E10: Around 366 K, both E9 and E10 exhibited an annealing phase. E9 was completely annealed out while E10's concentration increased. The removal of E9 from the system corresponded to the introduction of E10, indicating equal concentrations. Given their similar energy levels, interference between the two traps during Laplace-DLTS measurements was plausible, leading to variances in annealing rates.
- The E11 trap was present at relatively low concentrations directly after sample fabrication and went through two distinct annealing phases. In the initial phase, the trap's concentration rose sharply, whereas in the second phase, the concentration dropped to zero. No observable characteristics were shared between these annealing profiles and those of other traps within the system.
- The E12 trap was present immediately post-fabrication but was entirely removed from the system upon applying a reverse bias at 340 K. This process was irreversible.
- The E13 trap was observed in small concentration immediately after fabrication. However, once the sample reached temperatures near 420 K, the trap vanished from the system.

The concentration of C_i, $C_iO_i^*$, and C_iC_s in samples could be manipulated by varying the irradiation temperature or letting the sample rest at room temperature post-exposure. This allowed for correlation between known radiation-induced traps and traps found in pre-irradiated samples. The correlations were as follows:

- If $C_iO_i^*$ existed in post-irradiated samples, then the E2 trap would be present in the corresponding pre-irradiated samples.
- If C_i was present in post-irradiated samples, then the E3 trap would be found in corresponding pre-irradiated samples.

© University of Pretoria

Additionally, depth profiling showed that both the well-known radiation-induced traps and those found in pre-irradiated samples remained constant beneath the measurable distance below the Schottky junction.

7.2 Discussion of possible complex structure

Five energy levels associated with Pd traps were previously identified in the literature: a single acceptor level at $E_v + 0.34$ eV, which is thought to potentially comprise two distinct levels, and four donor levels at $E_c - 0.180$, $E_c - 0.220$, $E_c - 0.370$, and $E_c - 0.590$ eV. These donor energy levels mirrored the E4, E5, E7, and E14 levels in pre-irradiated samples. It's hypothesized that the E_c – 0.220 eV correlates with the Pd_s, given its high thermal stability, while the $E_c - 0.180$ eV is thought to relate to the Pd-vacancy complex due to its interaction with the O_iV complex. With these assumptions, it's inferred that the E5 corresponds to the Pd_s and E4 to the Pd_iV.

The E5 (having a similar signature as the $E_c - 0.220$ eV, identified as the Pd_s) was not detected immediately after fabrication, but only emerged after annealing at higher temperatures. In the introduction phase of the E5, the E14 annealed out, and the E5 concentration increased to a third of the E14's initial concentration. After its introduction, the E5's concentration remained stable, even at high temperatures (720 K), in agreement with the results by Gill *et al.* (1993). Given the assumption that the E5 correlates to the Pd_s, as suggested in the literature, and given that the E14 was also previously linked to a Pd complex by Gill *et al.,* it's plausible that E14 is a complex defect that dissociates during annealing, with a third subsequently forming the electrically active Pd_s trap and the rest forming an unobserved defect. It's important to note, however, that the rate of E5 introduction differed from the E14 annealing rate, but this could be attributed to a more complex annealing process.

In contrast to the results in this study, earlier investigations reported that the $E_c - 0.220$ was present in unannealed samples and would increase in concentration when annealed above 360°C (~633 K), but in this study, the E5 was observed only once the isochronal annealing reached around 370 K. This disparity could be attributed to different types of radiation exposure, such as alpha-particle irradiation, known for its short stopping distance and cluster formation in the substrate. Another possibility is the method of metal introduction into the system, which may require less energy to migrate or form this trap.

Examination of the isochronal annealing profile of the E4 trap (having a similar DLTS signature as a defect identified as the Pd_iV) revealed multiple annealing stages within the system. The first stage was clearly linked to the annealing of the E2 trap. When E2 was present, the E2 and the E4 experienced an identical decrease in concentration during the annealing of the E2. In samples without traces of the E2, the E4 did not exhibit this initial annealing stage. To explain this, we need to consider a process that would explain why the concentration of both defects reduced by exactly the same amount, with that of E2 going to zero and that of E4 remaining finite. Since we only observed the effect on the E4 when the E2 is present, we know the E2 has to be actively involved. We consider two possibilities:

1) The defect responsible for the E2 has another level that happens to correspond exactly to that of the E4. This sounds very unlikely, but might be a possibility.
2) The E2 in pre-irradiated samples was identified to be related to the $C_iO_i^*$ in post-irradiated samples. Taking this into consideration, the most likely complex formation would be the

© University of Pretoria

$C_iO_iPd_i$. As for the C_iO_i part, it is currently uncertain if it is still in the unstable state ($C_iO_i^*$) or transforms into the stable formation afterwards. What is certain is that the Pd seems to react with the unstable complex to produce the E2. This was seen in Section 6.6, when transforming the $C_iO_i^*$ to the stable C_iO_i (not observable in n-type Si without injection) before the deposition of Pd would result in no formation of the E2 after deposition. During the annealing of the E2, the E4 decreased in concentration at the same rate and concentration. Assuming the E4 relates to the literature Pd_iV, this suggests that the complex would dissociate with an impurity filling the vacancy site of the E4. It is however, not clear how 100% of these defects would be captured by the Pd_iV site.

During the E1's second annealing stage, the E4 increased in sync in both rate and concentration. The E4 would subsequently anneal out in two stages. Throughout these annealing stages, L-DLTS measurements were incapable of dividing the peak into multiple peaks, with the emission rate and measured energy level remaining consistent after each annealing stage. Literature assigns the energy level of the E4 to the Pd_iV. If we assume only the literature trap Pd_iV was observed at this energy level, the E1 can be interpreted as a Pd_i substitutional impurity complex (Pd_iI_s) where I presents the impurity. The complex dissociates, causing the impurity to diffuse away, thereby forming the newly increased Pd_iV complex, and thus increasing the E4 concentration.

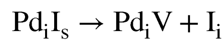

$$Pd_iI_s \rightarrow Pd_iV + I_i$$

The dominant impurity atoms that are expected to be present within this system are O, P, and C. Oxygen can be excluded as a possibility since it is known to occupy the interstitial site within Si. Both carbon and phosphorus can occupy the substitutional site, however, phosphorus in silicon is only mobile at extremely high temperatures. Carbon, on the other hand, exhibits high mobility in Silicon even at room temperature.

Given that this process takes place just 30 K above room temperature, it's plausible that carbon forms a complex with oxygen interstitials (O_i) almost immediately after dissociating, resulting in the formation of a carbon-oxygen interstitial complex (C_iO_i), which then stabilizes (See Section 3.1 for additional information).

This transformation hypothesis can be verified in future experiments, possibly within materials where an acceptor level of this defect may be observed. Theoretical modelling of the defects could also lend further credence to this theory. Such experiments and theoretical studies would provide a more concrete understanding of the processes and interactions at play in this system.

The first possibility is that the C_i dissociates from the complex, migrates and occupies the vacancy to form the Pd_iC_s complex. The Pd_iO_i complex would then be electrically inactive which would explain why no other peaks are introduced. If this was the case, it would contradict the suggestion of the possible Pd_iC_s complex explained for E1, as this would show a rise in concentration. Additionally, the temperature would be high enough where the C would dissociate from the complex after formation, in agreement with the suggested theory for E1. This would mean that either the E1 is the formation of an unknown impurity within the system, or the C does not dissociate from the E2.

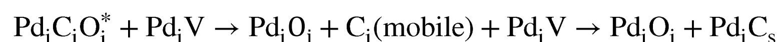

$$Pd_iC_iO_i^* + Pd_iV \rightarrow Pd_i0_i + C_i(\text{mobile}) + Pd_iV \rightarrow Pd_iO_i + Pd_iC_s$$

The second possibility is that the Pd_i dissociates from the complex, migrates and occupies the vacancy of the Pd_iV complex to form the Pd_iPd_s. The $C_iO_i^*$ then stabilizes into the C_iO_i complex due

© University of Pretoria

to the high temperature. The annealing midpoint for the stabilization of the $C_iO_i^*$ was found to be 316 K with the midpoint of the E2 annealing out to be around 328 K, which re-enforces this possibility.

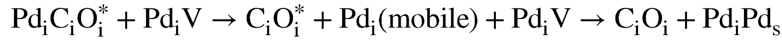

$$Pd_iC_iO_i^* + Pd_iV \rightarrow C_iO_i^* + Pd_i(mobile) + Pd_iV \rightarrow C_iO_i + Pd_iPd_s$$

The latter suggestion is most likely, however, C_iO_i peak is not visible in n-type material when in the stable formation. This theory can be investigated by using a p^+n substrate to investigate if the C_iO_i complex gets introduced as the E2 (E_v + 0.36 eV) anneals out.

The E3 in pre-irradiated samples was identified to be related to the C_i in post-irradiated samples. Taking this into consideration, the most likely complex formation would be the Pd_iC_i. The isochronal annealing profile didn't show any interaction with other visible electrical active traps. The E3 anneals out at a much higher temperature (midpoint 359 K) compared to the annealing profile of C_i (midpoint (307 K). There are two possible models that comes to mind. The first is that the Pd_iC_i dissociates into Pd_i and C_i, then migrating before forming complexes with other impurities.

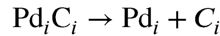

$$Pd_iC_i \rightarrow Pd_i + C_i$$

Considering the nature of the C_i to readily interact with other impurities within the system to form new complexes (i.e. C_iO_i, C_iC_s, P_sC_i, etc), one would expect to see these peaks introduced to the system. Unfortunately, none of these well-known peaks were introduced during its annealing phase, making this model highly unlikely.

The second model assumes that the Pd_iC_i is in an unstable state (i.e. $Pd_iC_i^*$) and stabilizes during this annealing phase into an electrically inactive trap in n-type material.

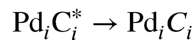

$$Pd_iC_i^* \rightarrow Pd_iC_i$$

Further investigation of this trap is required to clarify the model. It is suggested to investigate if an acceptor level gets introduced to the system during the annealing phase of the E3.

Previous investigations of Pd related traps assigned the E7 and E14 to be Pd-related as well. Currently there is not enough literature to help identify the possible complex structure of these traps.

The E6, E8, E9, E10, E11, E12 and E13 are all new traps that get introduced by diffusing Pd at a temperature where radiation induced defects don't anneal out of the system. This suggests that the complex formations of these traps point towards the combination of radiation damage and Pd.

7.3 Conclusion

This dissertation makes significant strides in our understanding of radiation damage and recovery processes in Schottky diodes, with a particular emphasis on those constructed on P-doped silicon (Si) substrates. The research addresses the intricate events following electron irradiation before fabrication, specifically when palladium (Pd) is used as a contact.

First, the study provides empirical validation for established knowledge about known radiation-induced traps, such as C_iO_i, C_i, C_iC_s, O_iV, VV, and P_sV, formed in Si wafers after ^{90}Sr radiation

© University of Pretoria

exposure. The isochronal annealing profiles presented align well with previous research, solidifying our understanding of these fundamental processes.

The study's crux lies in the revelation of new series of traps that emerge from pre-irradiation of the Si substrate. These unique traps display distinct annealing characteristics and interactions. For instance, the interconnected concentration changes of E2 and E4 traps during annealing imply complex defect interactions. Similarly, joint reductions of E1 and E4 traps, as well as the emergence of the E5 trap concurrent with the decrease of E4, underscore the intricate dynamics of these systems. While some traps, like E3, E6, and E8, displayed unique annealing phases, others like E7 demonstrated multiple phases, highlighting the richness of these interactions.

Interestingly, the research revealed that these new traps are localized within the first 60 Å of Pd deposited on pre-irradiated Si samples. The finding is unique to Pd contacts, unlike other metals like nickel (Ni), aluminum (Al), and gold (Au), where no new traps were found irrespective of irradiation timing. Silver (Ag) demonstrated some trap passivation but did not form new traps.

Rigorous steps were taken to ensure sample and deposition process purity, confirming the findings' credibility. Hydrogen influence was ruled out by shielding during substrate deposition, further strengthening the results. Additionally, the study illuminated how manipulating irradiation temperature or allowing the sample to rest post-irradiation can influence the concentration of known radiation-induced traps.

In-depth analysis of the E4 and E5 traps revealed complex interactions and possible scenarios of complex formations involving Pd, carbon interstitials, and oxygen interstitials. The study further explored the roles of highly mobile carbon and oxygen interstitials in complex formations and stability transformations. The study also hypothesizes two potential models for the behavior of the E2 and E3 traps, each with unique dissociation or stabilization pathways.

However, despite the extensive research, the study does not provide definitive answers to all questions, and certain discrepancies persist. There is a clear call for further investigations, particularly with different substrates and a closer look at certain complex stabilizations. The emergence of new traps introduced by diffusing Pd at specific temperatures underlines the necessity of future research to fully understand the interplay between radiation damage and Pd in these systems.

In conclusion, this study has substantially broadened our knowledge of radiation damage and recovery in semiconductor devices. It provides an intricate understanding of defect formation, behavior, and interactions within pre-irradiated Schottky diodes, particularly when Pd is used as a contact. Yet, the dynamic nature of these systems, characterized by multiple energy levels, defect complexes, and complex interactions, necessitates continued research. This research forms a robust foundation for further investigations in the field, guiding future efforts toward the development of advanced mitigation strategies against radiation damage in semiconductor devices.

7.4 Future work

In both the theoretical and experimental fields there is still a lot of work that needs to be done on these traps. Below is a summary of some of the work that needs to be done:

- True capture cross sectional measurements of all 14 traps seen in pre-irradiated samples.

© University of Pretoria

- Field effect measurements for all 14 traps seen in pre-irradiated samples.
- Reproducibility of the effect in p-type Si samples.
- The effect on other dopants in n-doped samples (i.e. As, Sb etc).
- Theoretical modelling for each trap, specifically $Pd_iO_iC_i^*$, to investigate stability and dissociation, Pd_iV to investigate stability and dissociation.
- The effect Pt has on pre-irradiated samples as this is another metal very similar to Pd.
- Attempt to observe the C_iO_i after annealing of the E2 to confirm the nature of the E2
- Investigations on the shift of the freeze out temperature of Si due to the Pd-effect

7.5 References

Gill, A., Iqbal, M. and Zafar, N., 1993. Palladium-related deep levels in silicon. *Semiconductor Science and Technology*, 8(5), pp.675-681.

© University of Pretoria